Thresholds of Deflection For Flexible Conical Vegetation Under Wave Flow

Msc Thesis: Hydraulic Engineering

Eli Weitzner

Delft University of Technology

TU Delft

Thresholds of Deflection For Flexible Conical Vegetation Under Wave Flow

by

Eli Weitzner

Eli Weitzner 5482135

Committee:

Dr.ir. Bas Hofland
Dr. Bregje Van Wesenbeeck
Ir. Su Kalloe

Project Duration: November, 2022 - Dec, 2023

Faculty: Faculty of Hydraulic Engineering, Delft

TU Delft

Acknowledgements

To my family and friends

Thank you for your continued support without which this would have been *impossible.*

Special thanks to my daily supervisor Su Kalloe.

For putting up with me all those long days in the lab.

Abstract

Woody vegetative systems can be found throughout the world in coastal environments, such as salt marshes, and mangrove forests. Due to this, many recent studies have placed a large emphasis on determining the effectiveness of these vegetative systems in coastal protection. Recently a study were conducted by [**Wesenbeeck et.al. 2022**] on the ability of pollard willow trees (*Salix Alba*) to reduce wave energy as protection for dykes. These tests showed that the trees generated a promising amount of wave reduction up to 22% in the full-scale testing. Interestingly, when the tests were recreated by [**Kalloe et al. 2023**]in the $1/10$th scale a maximum reduction of 30% occurred. This is thought to be due to the scale differences of the tests and the complex nature of flow around flexible canopies of willow trees. Due to the variations between the two data sets it was determined that more testing needed to be done to better understand the underlying processes. This study seeks to better understand the effects occurring around solitary woody branches under wave attenuation, by testing conical canopy mimics around varying values of stiffness and size. The mimics were created with three different sizes in an effort to induce different flow regimes. The thinnest mimics were consistently in low Reynolds flow with a Reynolds number of <1000. While the medium and large were in high Reynolds flow with a Reynolds number of >1000. The different sizes of mimics along with multiple materials also served as a method to create many different values of EI. The range of EI's across all different objects was $\in [453.8, 417226]$. The baseline model of the medium and thin cones also in theory had similar force-to-stiffness ratios as the branches of complex trees created by [**Kalloe et al. 2023**]. In theory, these mimics should go through the same deflection as the complex trees however this was proven to be untrue. The tests showed that the common numbers used to determine force-to-stiffness (Cauchy) $\in (0.009, 30.6)$ or inertia and drag (KC) $\in (5.63, 754.35)$ were poor predictors of tip deflection. Even the combined number generated by [**Jacobsen et al. 2019**] $\frac{CaL}{KC}$, which was determined to be a good predictor of motion in cylindrical stems of a constant cross-section, also failed to predict the deflection across the testing range. This is believed to be due to the tapering that occurs on conical objects. Thus, a new number which takes into account the 3-dimensional shape of the object, is proposed through empirical data fitting. This number

$$\theta = 1224 * \frac{F_p r \eta {S^3}^{1.19}}{EI}$$

provided a strong correlation with an R^2 of 0.742 between the peak force F_p generated by a waveform and the corresponding amount of deflection θ the object exhibited. It was also found that if the tip moved within 2 degrees of deflection, the object could be treated as fully stiff. And relatively stiff within 5 degrees, as a practical method to determine whether woody vegetation can be treated as stiff under flow conditions, to better gauge their effectiveness.

Contents

List of Variables

$\omega = wave\ frequency\ [\frac{1}{s}]$

$k = wave\ number\ [\frac{1}{m}]$

$\delta_y = Object\ Diameter\ at\ point\ [m]$

$E = Modulus\ of\ Elasticity\ [\frac{kg}{s^2 m}]$

$I = Second\ Area\ Moment\ of\ Inertia\ [m^4]$

$I_m = Mass\ Moment\ of\ Inertia\ [m^4 * kg]$

$\rho = fluid\ density\ [\frac{kg}{m^3}]$

$\rho_s = object\ density\ [\frac{kg}{m^3}]$

$d = water\ depth\ [m]$

$z = depth\ relative\ to\ waterline\ [m]$

$u_w = Peak\ flow\ Velocity\ due\ to\ Orbital\ Motion\ [\frac{m}{s}]$

$U_{ref} = Velocity\ at\ Point\ [\frac{m}{s}]$

$C_D = Drag\ Coefficient\ [-]$

$\overline{C_D} = Bulk\ Drag\ Coefficient [-]$

$C_M = Inertia\ Coefficient\ [-]$

$v = Kinematic\ Viscosity\ of\ Fluid\ [\frac{m^2}{s}]$

$l = Object\ length\ [m]$

$D = Object\ Diameter\ at\ Base\ [m]$

$S = Rate\ Of\ Tapering\ [-]$

$\eta = Max\ Wetted\ Branch\ Length [m]$

$\eta_p = Max\ Wetted\ Branch\ Length\ at\ Wave\ Peak [m]$

$\eta_h = Water\ Surface\ Elevation [m]$

$L = Orbital\ Wave\ Excursion\ Length\ [-]$

$\theta = Tip\ Deflection\ [Deg]$

$R_e = Reynolds\#\ [-]$

$Ca = Cauch\#\ [-]$

$Fr = Froude\#\ [-]$

$KC = Keulegan - Carpenter\#\ [-]$

$g = Gravity\ [\frac{m}{s^2}]$

$T_p = WavePeriod\ [S]$

$F_d = Drag\ Force\ [N]$

$\lambda = Wavelength\ [m]$

$r = radius\ [m]$

$U = Ursell\#\ [-]$

$Q = Discharge\ Per\ Unit\ Width\ [\frac{m^2}{s}]$

$c = Wave\ Celerity\ [\frac{m}{s}]$

$c_g = Wave\ Group\ Velocity\ [\frac{m}{s}]$

$n = Ratio\ of\ c_g\ to\ c\ [-]$

$\epsilon_v = Energy\ Dissipation\ of\ Waves\ Propogating\ Through\ a\ Vegetation\ Field[J/m/s]$

$b_v = Plant\ Area\ Per\ Unit\ Height\ [-]$

$\alpha h = Mean\ Vegetation\ Height\ [m]$

$N = Number\ of\ Vegetation\ Stand\ Per\ Unit\ Horizontal\ Area\ [-]$

$H_{rms} = Root\ Mean\ Squared\ Wave\ Height$

1 Introduction

Dyke protection has a large impact on the areas in and around the Netherlands. Dykes provide a large portion of the protection against flooding during incumbent storms and sea level rise. One concept for dyke protection lies around using vegetation. This study follows the use of the pollard willows trees (Salix Alba), as a form of foreground protection for dykes [**Wesenbeeck et al. 2022**], to reduce the wave energy reaching the dyke. When using woody vegetation as a source of protection it is important to quantify the parameters that can affect the efficacy of the material. The most important of these is the amount of force the vegetation can exert on the surrounding flow. Previous tests have been conducted on the subject. Both, model and full-scale tests were conducted by ([**Wesenbeeck et.al. 2022**],[**Kalloe et al. 2023**],). The studies were tested at realistic scales with irregular waves of up to a 1.5-meter average height, in storm conditions. The same tests were then repeated on a 1/10th scale. It was found that with similarly constructed forests, the resulting wave damping was 22% including all tree foliage in the full-scale tests. Compared to the small-scale tests which generated 30% wave damping with only the branch stems (no leaves), when waves passed through the bulk of the frontal area. The previous testing showed that even when properly scaled with the Young's Modulus of Pollard willow branches from the literature. Using the current methods, there are still complex processes occurring that can heavily affect outcomes. Most testing seeks to simplify the effects of bending. Dealing with fully flexible objects such as seagrass, or treating woody brush, such as mangroves as fully stiff. The expectation of this work is that due to flow effects, the movement of the trees was not fully captured through scaling, which led to errors in the results. Thus, this study seeks to look at the in-between. In hopes of determining when objects can be considered stiff or flexible when undergoing wave attenuation in nature. The objective of this study is to find the effects of object flexibility on its ability to exert force on incident waves. This, in turn, should provide a better understanding of the effect of object motion on wave damping. The main focus is to find the threshold when the deflection or motion of vegetation starts to impair the ability of the object to remove force from the incident flow. This is further complicated by the use of a complex shape in the form of a conical object. Most models for wave damping are derived from rigid cylinders with empirical corrections for flexibility. In this study, the focus is specifically, on objects comparable to that of woody brush. The secondary focus of this study is on the effects of the force-to-stiffness ratio (Cauchy#) and the drag-to-inertia ratio (Keulegan-Carptenter#) on this threshold. This is done in an effort to determine why there was a large disparity between the damping effects of the model tests done in the small flume, [**Kalloe et al. 2023**] and the large-scale tests conducted in the delta flume [**Wesenbeeck et.al. 2022**]. To achieve this, a range of conical solitary mimics with different sizes and material properties will be tested at the 1/10th scale. These mimics will be tested across two water levels one where they are fully emerged and one partially submerged. The forces induced by wave flow on the mimics will be recorded as a method of relating the ability of the mimics to induce wave damping. The motion of the objects will be recorded through a mounted camera as a method of relating the object's motion to the forces

felt. An overview of the experimental set-up can be found in **Sections 3.1 and 3.4**. The testing specifications can be found in **Section 3.2**. Image processing can be found in **Section 4.1** while the quantitative analysis can be found in **Section 4.2**. The relationships of active variables to the processes of deflection can be found in **Section 5**. The fitting of a new number for the prediction of deflection can be found in **Section 6**. Conclusions and Recommendations in **Section 8**.

2 Literature Review

2.1 Quantifying Object Size

When quantifying the size of vegetation there are two styles of schematization that can be taken into consideration for this experiment. Volumetric [**Strusi ska-Correia et al. 2013**] in this research on mangroves under tsunami-style waves. The bird's eye view is kept constant for a model, while the volume is changed by adjusting the sizes of the cylinders which then affects the frontal area as well. See Fig.1

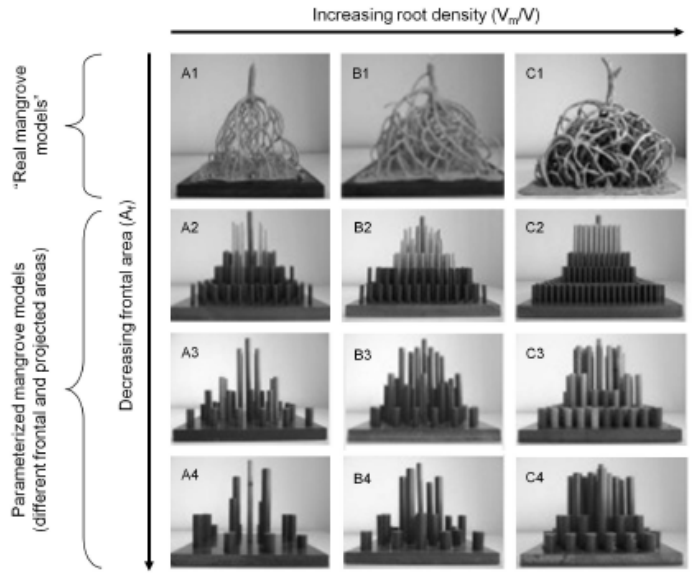

Figure 1: Volumetric Mangrove Schematization [**Strusi ska-Correia et al. 2013**]

The other method is, projected frontal area in the test done by [**Kalloe et.al. 2023**] projected frontal area is the only thing that is tracked. One of the methods is through the use of Lidar to find the frontal area of the tree. This leads to the following projected frontal area determination of a pollard willow which can be seen in Fig.2

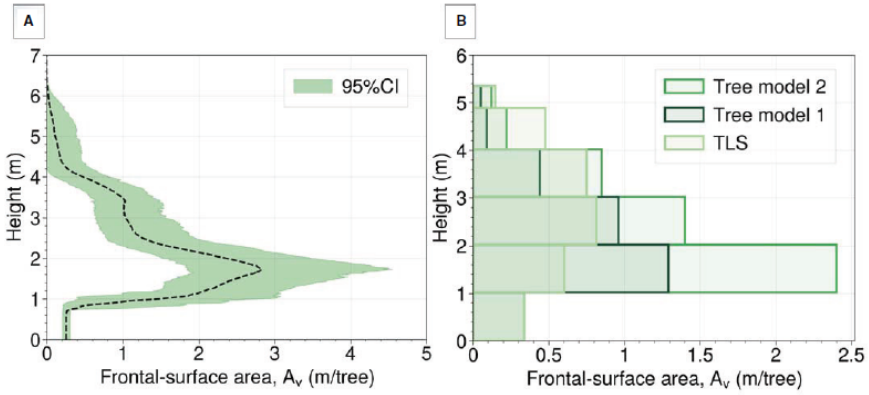

Figure 2: Average Frontal Surface Area of Trees [**Kalloe et al. 2023**]

Volumetrically, nothing is taken into account, if the shape of the object is held constant volumes will also be scaled. However, if the shape is simplified to that of a cone or cylinder the volume of the object will also change. This means for the less complex (larger objects) there is an extreme difference in total volume between the scale trees and the schematized cones or cylinders. When comparing both cases across the relevant dimensionless numbers, a frontal area approximation makes the most sense as most dimensionless numbers used for scaling, are derived from the Morison equation [**Morison et al. 1950**] which projects flow 2-Dimensionally.

2.2 Canopy Forcing

When determining forces due to flow, the force is based on a cylindrical shape which can be readily adapted to a cone using an integration over the height of the object. The initial equation for a conical object subject to flow is based on [**Morison et al. 1950**].

$$F_x = F_d + F_i \tag{1}$$

where F_x is the force generated by the object due to flow.

$$\overline{F}_d = \frac{1}{2}\rho\delta_y C_d U_{ref}^2 \tag{2}$$

$$F_i = \frac{\pi}{4} C_M \delta_y^2 U_{ref} \frac{dt}{du} \tag{3}$$

Where $\overline{F}_d$ is the average force on the object due to drag and F_i the average force due to inertia. ρ is the fluid density, δ_y is the diameter at a point, and U_{ref} is the orbital velocity induced by the wave over the height. C_d is the drag coefficient, and $C_M = 1 + C_a$ is the moment of inertia coefficient. In an ideal fluid around a cylinder $C_M = 2$ [**Mohamed A. 2012**] the general range, however, is between 1.5 to 2.0. Since this work deals with flow under waves the velocity will vary with the object height and thus it must be integrated from z = 0 to the peak. In this experiment, it is worth noting that δ_y also varies with height. However, since the active object profile in this work is a non-constant diameter, the following adjustment must be made for validity. The force prediction

equation must instead treat the object as multiple slices of cylinders resulting in the following equations.

$$\overline{F}_d = \frac{1}{2}\rho \int_{z=0}^{\eta} \delta_y C_d U_{ref}^2 dz \tag{4}$$

$$F_i = \frac{\pi}{4} \int_{z=0}^{\eta} C_M \delta_y^2 U_{ref} \frac{dt}{du} dz \tag{5}$$

where.

$$U_{ref} \frac{dt}{du} = -a\omega^2 \frac{sinh(kd)}{sinh(kz)} sin(\omega t) \tag{6}$$

Where η is the maximum wetted branch area, a is the wave amplitude,ω is the angular frequency, d is the water depth, and z is the vertical coordinate. To approximate the force F_x properly, a proper drag coefficient and inertia coefficient C_d, C_M must be applied to the equation. The inertia term however may be removed from the calculations. The peak forces are expected to occur at the wave peak, at this exact moment the change in velocity of the wave is entirely in the vertical direction, thus $F_i = 0$ and $U_{ref} \frac{du}{dt} = 0$ resulting in only the drag term being active in the equation.

$$F_x = F_d = \frac{1}{2}\rho \int_{z=0}^{h_v} \delta_y C_d U_{ref}^2 dz \tag{7}$$

The drag coefficient can be approximated in two different ways, using the Reynolds number via the following equation [**Van Rooijen et.al. 2018**],

$$C_d = 1 + 10 * R_e^{-2/3} \tag{8}$$

Where C_d is the drag coefficient, and R_e is the Reynolds flow around an object.

$$R_e = \frac{U_{ref} \delta_y}{v} \tag{9}$$

[**Reynolds et al. 1883**] where U_{ref} is the orbital velocity, δ_y is the diameter at a point, and v is the kinematic viscosity of the fluid. This work will be looking at a high Reynolds number which is a Reynolds of greater than 1000 [**Fredsoe et al. 2006**] which can be seen in fig. 3

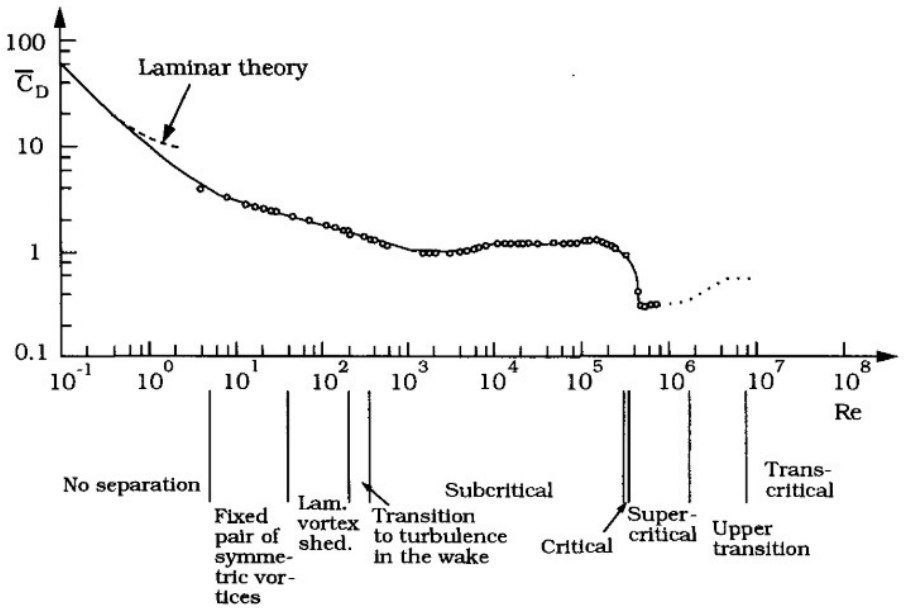

Figure 3: Cd Vs Reynolds [**Fredsoe et al. 2006**]

The drag coefficient can also be calculated using the work by [**Keulegan et al. 1983**] where the drag coefficient can be approximated using the Keulegan-Carpenter number,

$$\frac{U_{ref}XT}{\delta_y} \tag{10}$$

where T is the wave period of a regular wave.

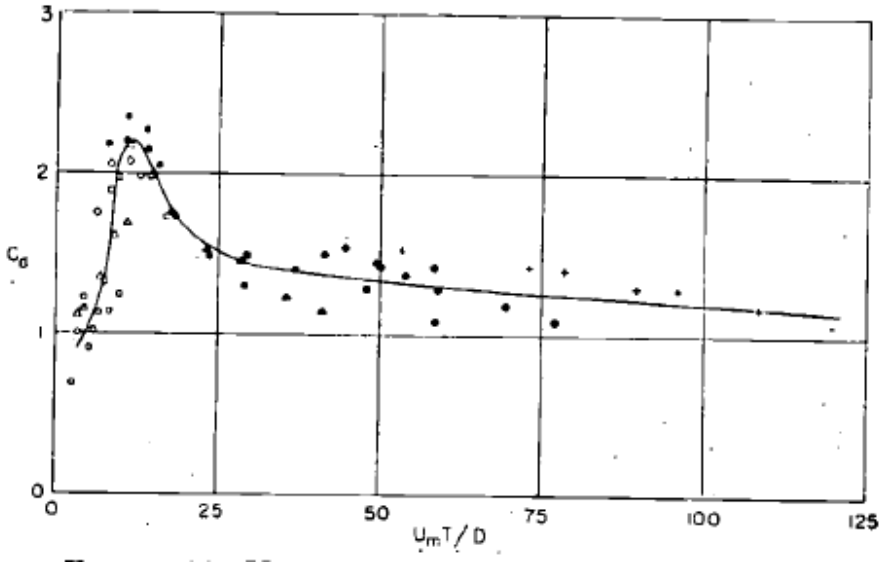

Figure 4: KC Vs Drag Coefficient [**keulegan et al. 1956**]

A comprehensive study by [**Chen 2018**] compares different methods of determining drag across different com-

binations of wave-current flows. Referencing a study by, [**Jadhav 2013**] which studied the dissipation of wave energy through salt marsh vegetation. They generated the following fit.

$$\overline{C_d} = 70KC^{-0.86} \tag{11}$$

Where $\overline{C_D}$ is the bulk drag coefficient. Which corresponds to a regressive fit of 0.95 across all recorded observations inside a KC range of 25 to 135. This generates the following figure.

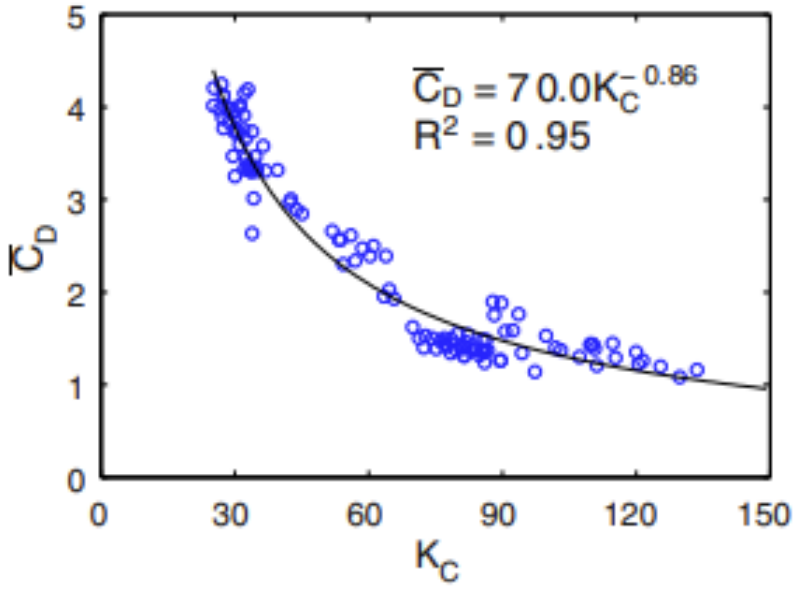

Figure 5: Cd Vs KC [**Jadhav 2013**]

For values below a KC < 6 a study by [**Bradley 2009**] which focused on the dissipation of flexible seagrass, found a value of,

$$C_d = 253.9KC^{-}3.0 \tag{12}$$

with a R^2 regression of 0.95. Between the KC values of 3<KC<59 the equation by [**Mendez et al. 2004**] in the study finds that $\overline{C_d} = 0.47^{(-0.52KC)}$ with a R^2 regression of 0.76 which can be seen in the following figure 6.

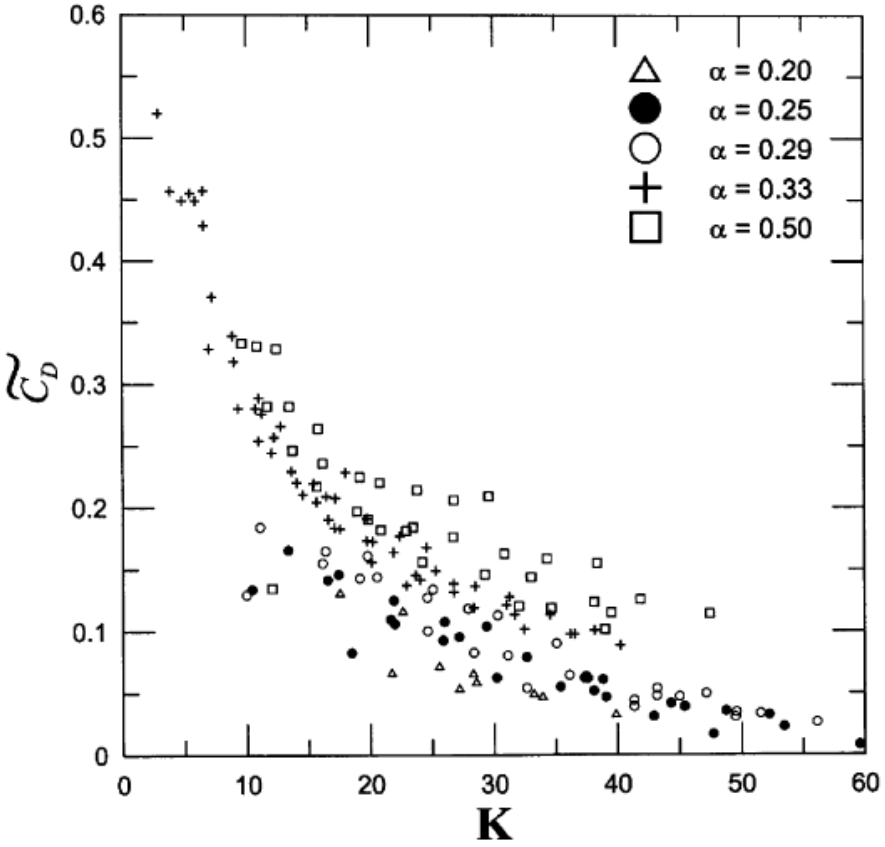

Figure 6: Cd Vs KC [**Mendez et al. 2004**]

What these different drag coefficients mostly show is that based on the bulk dimension of the object, and under different flow regimes the expected drag coefficient can change by a large degree. Owing to this the rough estimation of the bulk drag coefficient will be created in this work as a method for determining forces acting upon an object. Using data fitting from the forces recorded. The forces can then be used as an indicator of the ability of vegetation to initiate wave damping. The relation was originally made through [**Dalrymple et al. 1984**] with the relation.

$$\epsilon_v = \frac{2}{3\pi}\rho C_d b_v N(\frac{kg}{\omega})^3 \frac{sinh^3(k\alpha h) + 3sinh(k\alpha h)}{3kcosh^3(kh)} H^3 \tag{13}$$

Where αh is the mean vegetation height, N is the number of vegetation stand per unit horizontal area, b_v is the plant area per unit height, and ϵ_v is the energy dissipation of waves propagating through a vegetation field. This equation was further expanded on for random wave fields ([**Mendez et al. 2004**].

$$\epsilon_v = \frac{1}{2\sqrt{\pi}}\rho C_D b_v N(\frac{kg}{2\omega})^3 \; X \; \frac{sinh^3(k\alpha h) + 3sinh(k\alpha h)}{3kcosh^3(kh)} H_{rms}^3 \tag{14}$$

Where H_{rms} is the root mean squared wave height. Both equations are derived from the simpler relationship

$$F_x = \frac{1}{2}\rho C_D b_v N U_{ref}|U_{ref}| \tag{15}$$

Thus forces will be used in this work as a method of relating damping.

2.3 Flexible Vegetation: Pollard Willows

A previous test series conducted on pollard willow trees by [**Wesenbeeck et al. 2022**] found that protection of trees under storm conditions could reduce the incident wave energy by a maximum of 22% over a 40-meter forest consisting of 32 trees. Using pollard willow trees 15 years of age with 3-year aged branches from the knot. These experiments were then recreated in a 1/10 scale flume by [**Kalloe et al. 2023**]. With a re-creation of the full-scale set-up, it was found that the maximum reduction of wave energy was 30% in a 4-meter forest consisting of 32 trees across the same wave conditions. Soft PLA (E modulus of 400Mpa) was used to generate similar flexibility in the 1/10 trees by scaling the force-to-stiffness ratio using the Cauchy number. Below is the representation of the average tree used in the scale testing.

Figure 7: Complex Scale Canopy
[**Kalloe et al. 2023**]

With conditions matching those of the full-scale tests, it raised the question of what scale effects caused the difference in peak force reduction between the two tests. This discrepancy is thought to be due to the effects of flow turbulence in the form of the Reynolds number and the object's flexibility.

2.4 Relevant Non-Dimensional Numbers

A paper by [**Jacobsen et al. 2019**] provides the most relevant usage of the KC and Ca numbers in relation to the present study. The paper covers the motion of a flexible stem under wave flow with varying material properties and dimensions to affect the object's motion under wave duress. The results comparing the combined number:

$$\frac{CaL}{KC} \tag{16}$$

Where Ca is the force to stiffness ratio or the Cauchy number (Ca)

$$Ca = \frac{\rho \delta_y U_{ref}^2 l^3}{EI} \tag{17}$$

Where ρ is the fluid density, and l is the object height E is the Young's Modulus, and I is the second area moment of inertia of vegetation of a constant cross-section. L describes the "length of the stem to the to the wave orbital excursion" [**Jacobsen et al. 2019**]

$$L = \frac{l}{a_w} = \frac{l\omega}{u_w} \tag{18}$$

Where u_w is the characteristic orbital velocity. KC the Inertia-to-Drag ratio

$$KC = \frac{U_{ref} XT}{\delta_y} \tag{19}$$

Where T is the wave period of a regular wave. This number is used as a method for determining the motion of flexible stems. Inside the testing on stems by [**Jacobsen et al. 2019**] it was found that the quantity $\frac{CaL}{KC}$ was a better predictor of motion than just simply using CaL. The $\frac{CaL}{KC}$ number can be used to match the scale material properties generated by [**Kalloe et al. 2023**] during the previous testing series to the full-scale tests. As this experiment is focused on relating the scale effects between the full scale and model tests an important factor is the effects of the vegetation flexibility. it is well known that flexibility has an impact on object performance however the amount is difficult to quantify, as modes of deflection, object shape, and flow regime can all have large impacts [**Nepf 1999**]. Hence objects with different flexibility are tested to find out if the effects are constant across similar conditions or if it is also dependent on the flow turbulence R_e, KC. To relate these simply the relationship of EI is to be used to generate an array of different flexibility's to be tested.

2.5 Wave Generation

Due to the nature of this thesis attempting to link the variation between the full scale and model tests done by [**Kalloe et al. 2023**; **Wesenbeeck et al. 2022**] the wave generation will follow similar testing conditions as done in the prior tests to check the importance of flexibility. In nature and in the previous tests by

[**Kalloe et al. 2023**; **Wesenbeeck et al. 2022**] both stokes and Cnoidal waves are present during storm conditions. The classifications of such can be found using the Ursell number which was developed along with Cnoidal wave theory by [**Korteweg et al. 1895**; **Ursell 1953**]

$$U = \frac{HL^2}{h^3} \tag{20}$$

Where h = water depth, L = wave length and H = wave height. while U<10 Stokes theory is valid, for 10 < U < 25 both Cnoidal and Stokes theory are valid, and U>25 only Cnoidal theory is valid.

2.6 Stokes Waves

Wave types can be determined using the Ursell number $U = \frac{HL^2}{h^3}$ If the parameter falls below a value of U = 10 then the wave is assumed to be inside the Stokes regime. As such linear wave theory is applied to find the peak orbital velocities to be used in the calculations of the relevant variables. Using equations derived by **[Airy 1845],[Stokes 1847]** for linear wave theory.

$$w^2 = gktanh(kd) \tag{21}$$

and

$$U_{max} = \omega a \frac{cosh(k(d+z))}{sinh(kd)} \tag{22}$$

Where U_{max} is the peak velocity at a point, ω is the angular frequency or $\frac{2*\pi}{T}$, g is the gravitational constant (9.81 $\frac{m}{s^2}$), k is the wave number or $\frac{2\pi}{\lambda}$, d is depth, and z is the vertical coordinate.

2.7 Cnoidal Waves Approximation

If the incident wave has an Ursell number that is between 10 and 25 it is Cnoidal and stokes, if above 25 the wave is fully Cnoidal. Based on similar work by Jochem Dekkers and [**Goring et al. 1978**], where the wave paddle was used to calculate the Cnoidality of the waves, a method was derived to find the Cnoidal peak velocities for use in this experiment. Since depth-averaged velocity can be defined as

$$U = \frac{Q}{h + \eta_w} \tag{23}$$

, where Q is the discharge per unit width of the flume and

$$Q = c * (\eta_w) \tag{24}$$

and U is the depth-averaged velocity, c is the wave celerity, and η_w is the wave surface elevation above MWL.

$$U = \frac{c\eta_w}{h + \eta_w} \tag{25}$$

Then since the net flux in the system can be assumed to be 0, as all is done in a flume. Here however the method will differ from that of [**Goring et al. 1978**] as we do not have the motion of the wave paddle itself in the x direction. In tests, accurate wave data will be taken at the point of interest. Knowing this the wave data for the relevant test is taken from then compared to the WSE of the same wave generated from linear theory at the peak. This is possible because both waves are the same wavelength meaning the peak cross-sectional areas can be compared as they will be in phase with one another resulting in the following equation.

$$U_{ref} = U_{max} * \frac{\eta_{w-cn}}{H/2} \tag{26}$$

This can then be used to approximate the difference in depth-averaged flow velocity between the real and linear cases. Full derivation can be found in Appendix B section 5.

3 Methods

3.1 Overview of Experiment

Stiff and flexible conical canopy mimics will be tested over different water levels. these tests are roughly based on the experiments conducted by [**Kalloe et al. 2023**] ie) 1/10 scale. This campaign differs from the previous works by seeking to look at a more simplified view of the canopy of a willow tree in isolation. As a method of determining a better understanding of the individual motions of the branches in a woody canopy. Conical objects are used here as the branches and canopies of pollard willows have a projected frontal area that mimics a conical shape. The main variables that will be tracked across this work are the forces felt by the canopy (mimic) as well as the amount of deflection or motion it undergoes. A list of the variables used to relate the force and motion can be found in **Section 3.3**. To capture all of this a short burst of regular waves will be used with the parabolic damper at the back of the flume. This will allow reflections to be ignored in the data. A force transducer will placed underneath the object to determine the forces in the X-direction. The recorded forces will be used to determine the effect of object bending on damping within a wave-attenuated flow. The object bending or deflection will be recorded using a camera, set on a mount [**Kalloe et al. 2023**; **Jacobsen et al. 2019**]. Then, used later as a way to compare the effects of wave damping, as objects go through deflection.

3.2 Scaling and Schematization

3.2.1 Object Scaling & Mimic schematization

A representation of the original complex scale trees, created by [**Kalloe et al. 2023**] as per the previous works in the WOODY project can be seen in the following figure 8. Which have a frontal surface area akin to this

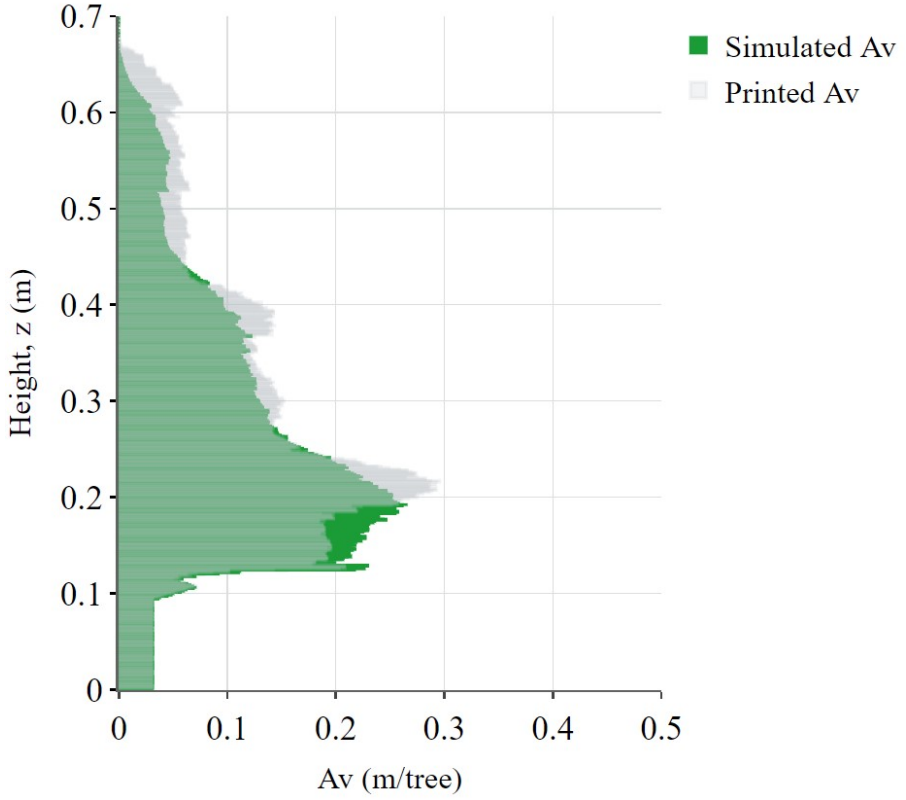

Figure 8: Complex Tree Frontal Area[**Kalloe et al. 2023**]

The trees are made up of 4 components, the trunk, and then three different branch classes, class 1-3. The class 1 branches are the largest with a base diameter of over 5 millimeters. The class 2 with a base diameter of 2-5 millimeters, and the class 3 with a diameter of less than 2 millimeters. The maximum branch lengths are roughly 0.43, 0.25, and 0.1 meters respectively. For this project, two shapes were considered to represent the simplified canopy of the tree. A cylinder that projects a rectangular frontal area. Or a cone that projects a triangular frontal area. Cones were chosen as the optimal shape as they can not only match the projected frontal area of the total canopy but that of the singular branches as well. This will induce a more realistic shape of deflection with a realistic vertical variation in I.

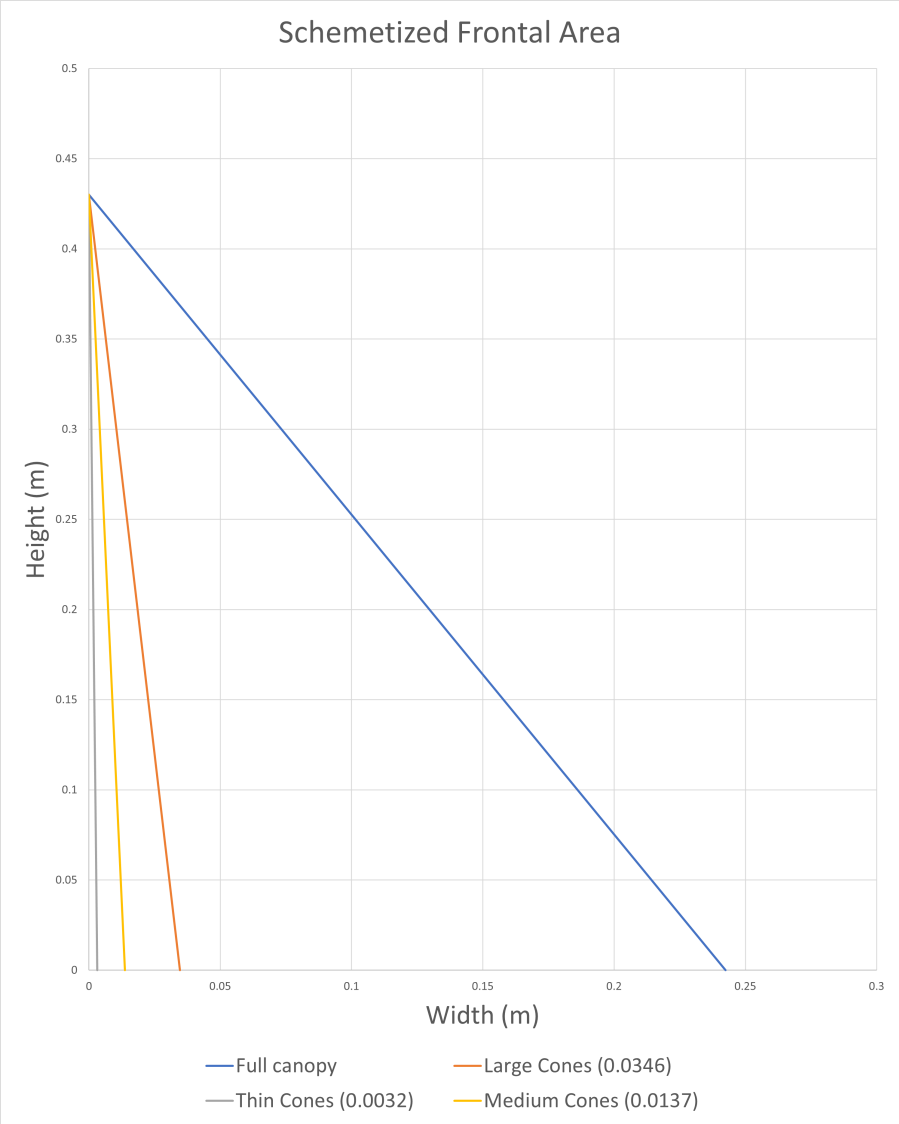

Figure 9: Simplified Frontal Area Above Trunk

Due to this relation, the cone (mimic) is used as the relative shape for the rest of this experiment. A cylinder is used as the trunk for all tests, this trunk has a 1:1 scale with the complex model trees. With dimensions 0.1 meters tall, and a circumference of 0.035 meters. This is indicative of the average trunk of the complex trees tested in previous experiments by [**Kalloe et al. 2023**]. To ensure the entire canopy is covered in the experiments a branch length of 0.43 meters was used, which is the same height as the class 1 branches. See figure 10 for an example of the Large cone.

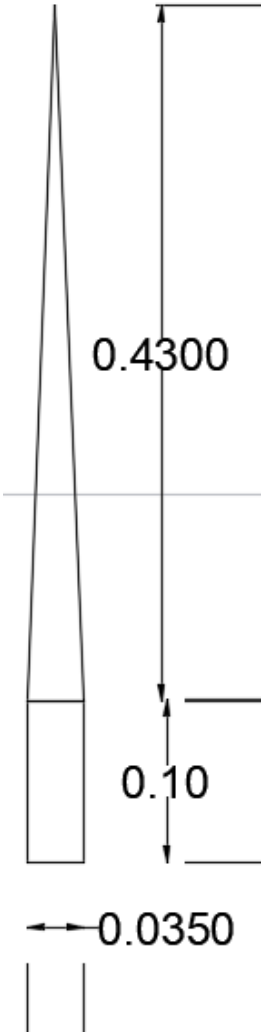

Figure 10: Example Cone & Mount

This will give the schematized cone the same overall height as the bulk of the complex tree canopy. Different base diameters will be used to induce different flow regimes, along with varying E-moduli to change the amount of deflection experienced. The specifics can be found in the following table.

Table 1: Combinations of Sizes and Materials

Diameter at base (m)	Length (m)	Youngs Modulus (Mpa)	Material Type
Large: 0.0346	0.43	5	FilaFlex 60A
	0.43	7.5	FilaFlex 70A
	0.43	56	TPU 95A
	0.43	1820	Ultimaker PLA
Medium: 0.0137	0.43	5	FilaFlex 60A
	0.43	7.5	FilaFlex 70A
	0.43	56	TPU 95A
	0.43	1820	Ultimaker PLA
Thin: 0.0032	0.43	400	Soft PLA
	0.43	1820	Ultimaker PLA

Across this combination of materials and sizes the range of the Cauchy number will be in $\in (0.0009, 30.6)$ and KC within $\in (5.63, 754.35)$. The average Reynolds number for the thin cones will be low ie) Re <1000, while for the large and medium cones it will be greater than 1000.

3.2.2 Wave Scaling

The waves will be using a 1/10th scale wave height, from the large Delta flume tests to better mimic the approach taken by [**Kalloe et al. 2023**; **Wesenbeeck et al. 2022**] The water levels will also have the same scale to keep the wave scaling consistent. The waves are scaled using the initial T_p and H_{m0} and deep water level d_{deep}.

Table 2: Wave Scaling

d_{deep}	d_{Tree}	T_p	H_{m0}	d_{deep_new}	d_{Tree_new}	T_{p_new}	H_{m0_new}
6.83	4.5	3.9	1	0.683	0.45	1.23	0.1
5.33	3.0	5.6	1	0.533	0.30	1.77	0.1

For the basic flow velocity calculations, the peak orbital velocities under the wave are taken using eq.

$$u_{w,max} = \frac{a\omega \cosh kh}{\sinh kz} \tag{27}$$

All waves were then scaled using the Froude Equation.

$$\frac{U_{ref}}{\sqrt{gh}} \tag{28}$$

For completeness and to generate a full spectrum of waves the heights 0.14, 0.18, 0.05 were added to the tests for each water level and wave period as well. The following conditions were tested.

Table 3: Overview of Generated Waves

Test#	T_p (S)	λ (m)	Wave Height (m)	d_{Tree} (m)	Ursell #	Classification	Incidence
1	1.00	1.37	0.05	0.3	3.5	Stokes	Non-breaking
2	1.00	1.37	0.1	0.3	7.0	Stokes	Non-breaking
3	1.00	1.37	0.14	0.3	9.8	Stokes	Non-breaking
4	1.23	1.83	0.1	0.3	12.4	Stokes and Cnoidal	Non-breaking
5	1.23	1.83	0.14	0.3	17.3	Stokes and Cnoidal	Non-breaking
6	1.23	1.83	0.18	0.3	22.3	Cnoidal	Breaking
7	1.77	2.84	0.1	0.3	29.9	Cnoidal	Non-breaking
8	1.77	2.84	0.14	0.3	41.8	Cnoidal	Breaking
9	1.77	2.84	0.18	0.3	53.8	Cnoidal	Breaking
10	1.77	2.84	0.05	0.3	14.9	Stokes and Cnoidal	Non-breaking
1	1.00	1.49	0.05	0.45	1.2	Stokes	Non-breaking
2	1.00	1.49	0.1	0.45	2.4	Stokes	Non-breaking
3	1.00	1.49	0.14	0.45	3.4	Stokes	Non-breaking
4	1.23	2.07	0.1	0.45	4.7	Stokes	Non-breaking
5	1.23	2.07	0.14	0.45	6.6	Stokes	Non-breaking
6	1.23	2.07	0.18	0.45	8.5	Stokes	Non-breaking
7	1.77	3.36	0.1	0.45	12.4	Stokes and Cnoidal	Non-breaking
8	1.77	3.36	0.14	0.45	17.3	Stokes and Cnoidal	Non-breaking
9	1.77	3.36	0.18	0.45	22.3	Cnoidal	Non-breaking
10	2.10	4.11	0.05	0.45	9.3	Stokes	Non-breaking

3.3 Dimensional Analysis

The following figure details the variables that can be recorded and tracked during testing.

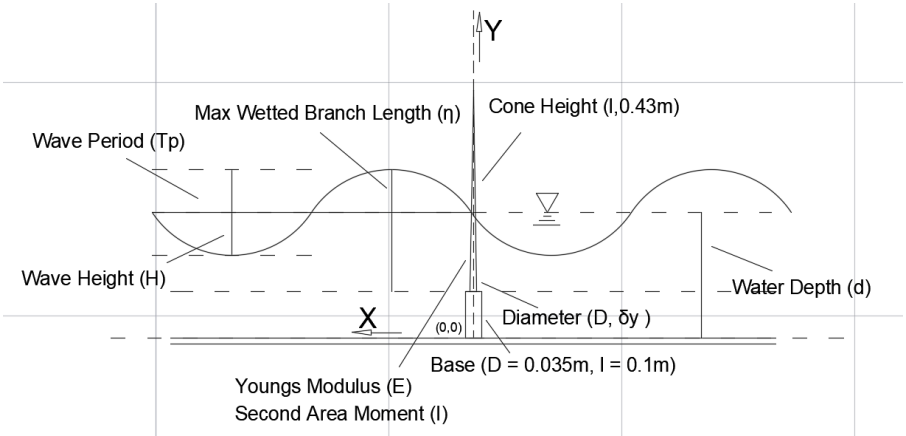

Figure 11: Variable Diagram

Breaking this down we have the following variables to work with as well as the mechanical property variables of the object and fluid:

$\eta = Max\ Wetted\ Branch\ Length\ [L]$

$T = Wave\ Period\ [T]$

$d = Water\ Depth\ [L]$

$H = Wave\ Height\ [L]$

$\delta_y = Diameter\ [L]dz$

$D = ObjectDiameter\ at\ Base\ [L]$

$l = Objectlength\ [L]$

$\rho = Density\ [ML^{-3}]$

$v = Kinematic\ Viscosity[L^2S^{-1}]$

$E = Young's\ Modulus\ [ML^{-1}T^{-2}]$

$I = Second\ Area\ Moment\ [L^4]$

When viewing the quantifiable variables, all three dimensions of $[L, M, T]$ can be found. According to the Buckingham-Pi Theorem **[Hughes 1993]** with 10 variables across three dimensions 7 unique combinations can be created. Four of these can immediately go to the Cauchy, KC, Reynolds, and the Froude number. Leaving three more available combinations, one of which can be the rate of tapering of the object or slope $\frac{l}{D-\delta_{y,t}}$ the second being the peak of the incident wave relative to the height of the object $\frac{\eta}{l}$. The third can be $\frac{H}{D}$ the ratio of the wave height to the diameter at its base. It should be noted that η is 0 at the base of the object and maxes out at the peak of the object i.e. its maximum value is equivalent to l (0.43m) for this analysis.

Other terms can be combined into some common variables as well such as force, $[MLT^{-2}]$, or $U_{ref}, [LT^{-1}]$ which will be used later in the discussion section of this report.

3.4 Experimental setup

This experimental setup will follow a similar plan as the previous small-scale tests conducted by [**Kalloe et al. 2023**]. The notable differences are the exclusion of irregular waves and no forest. The only object in the flume will be the mimic (cone), and the mount attached to the force gauge at the base. The wave damper is also set at the back of the flume to increase the time between generation and reflection.

3.4.1 Tree Placement

Cones will be placed on a platform raising them up by 0.233 meters off the bottom of the flume. With, a distance of 11.3 meters from the wave maker. The platform is connected to a foreshore slope extending towards the deep water ie) the wave generator. For images of the set-up see figures 12, 14, and 13.

3.4.2 Wave Gauges

10 wave gauges will be used, three in deep water (WG 1-3), and three in front of the tree (WG 4-6) to check the wave heights before impact. The three (WG 8-10) behind the structure to check for reflection will not be used in these tests. The final gauge (WG 7) is placed in line with the tested mimic. All ten wave gauges were placed on the (y) center line of the flume with X being the relative distance from the wave maker. All WGs have a sampling rate of 200Hz for all tests. For gauge placements see fig 12.

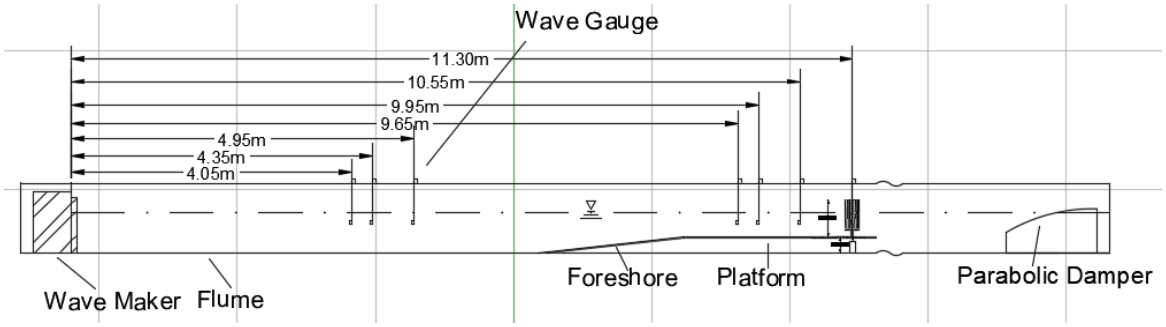

Figure 12: Side View Tank

3.4.3 Force Gauge

For all relevant tests, a force gauge was placed under the mount of the cones. At the same x location as that of WG7 which is 11.3 meters from the wave paddle. This will be used to measure the applied force of the fluid in the x-direction. The gauge measures force through the single-point bending of a steel beam. The FG has a sampling rate of 200Hz. See Appendix E table 8 for more specifications on the FG.

Table 4: FG Specs

Range (V)	Sensitivity (V)	Calibration Factor (N/V)	Sampling Freq (Hz)
10	0.01	0.024525	200

3.4.4 Capturing Object Motion

A camera was mounted on a separate mount that was suspended using wooden beams, these are attached perpendicularly to the wave flume. This ensured that the camera did not move between tests. Inside the camera mount, there are vertical guides and a horizontal guide that allow the camera to be locked in a specific direction. Keeping constant positioning between tests. see Fig.14,13 for the set-up. For the camera specifications see Appendix E.

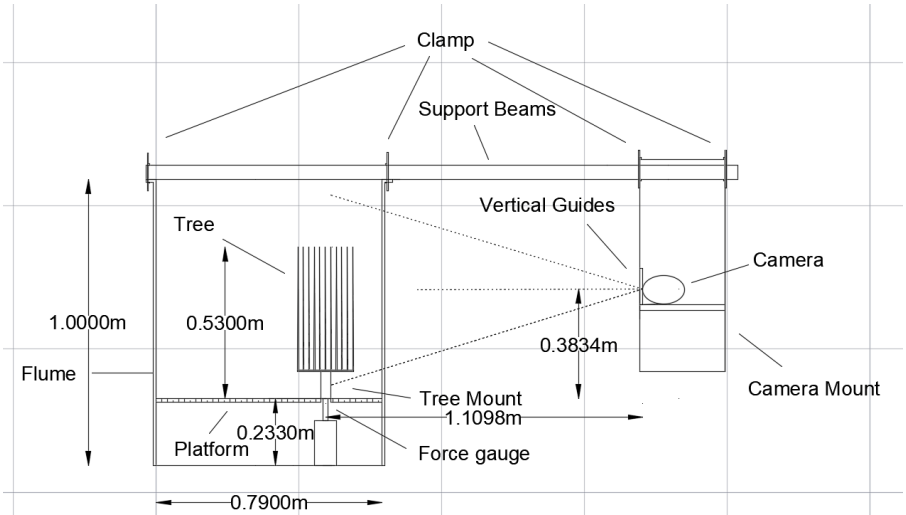

Figure 13: Camera Setup Sketch Side View

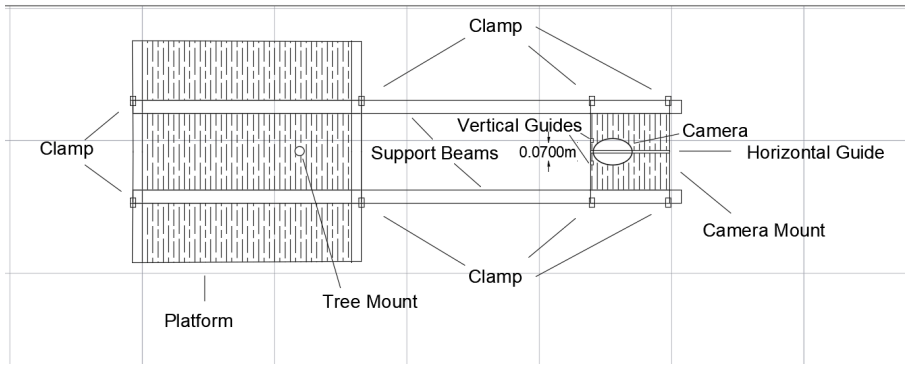

Figure 14: Camera Setup Sketch Top View

Deflection will be recorded using the camera as specified above, the camera is roughly 1.1 meters from the center of the mimic. The sampling rate of the camera is 25 FPS for the large cones and 50 FPS for the medium and thin cones.

4 Processing

4.1 Image Processing

4.1.1 Magnification Factor

While the checkerboard is submerged at all points in the x-y direction the size of a 20 mm square is 36 pixels or 0.55 mm per pixel. The dry checkerboard shows that 20mm, or one square is covered by a distance of 32 pixels i.e. 1 pixel is equivalent to 0.625 mm, this means converting the captured pixels to dry from submerged is a factor of 9/8.

4.1.2 Lens Distortion

The camera being used in this experiment has an optimal focal length of 1.2 meters. The lens was placed roughly this distance from the tested object, at this focal length there is minimal to no lens distortion. Due to the mount, the tangential distortion is consistent. The distortion was found using a large checkerboard and a light intensity filter inside of Matlab. The maximum possible distortion experienced by the object then was calculated to be roughly $+-1$ pixel across the entire object length of 0.43m or roughly $+-0.008$ deg (θ), See Appendix A Section 1 for the full calculation set.

4.1.3 Object Tracking & Measurement Error

This section covers the range of errors for the measurements of the objects themselves. In the videos with proper lighting, the image contrast is very high. Therefore the measurements can be taken by a computer with

no error in an image. However, in low-contrast images, the tip measurements must be done by hand, the zoom inside of Matlab allows for an error of +- 1 pixel.

This means for the 1080p image the maximum displacement from the actual value to pixel measurement error is 2 pixels. Between points or a confidence interval of +- 1.25 mm from the recorded values, in the 1080p images. For the 4k images the value then becomes +- 0.625 mm from the recorded values.

for measurements taken by hand, there is a set of rules that must be followed to ensure that everything is taken properly.

1. The highest leftmost point is taken as the object tip.
2. All measurements are taken from the leftmost side of the object (base and tip for still and active positions).
3. If there is motion blur, then the blur that occurs in the leftmost part of the screen is assumed to be the active point of the cone and recorded as such.

Examples of high and low-contrast images can be found in Section 2 of Appendix A.

4.1.4 Object Tracking

Objects are tracked in Matlab using the grayscale and difference functions to generate an array of high-contrast points. These points can then be used to recreate the image in a scatter plot where only the areas of interest are visible. While some noise does slip through the filter the object itself is highly visible.

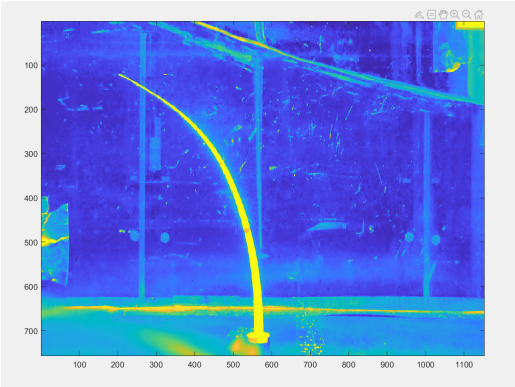

(a) Grayscale Image T#:6-0.68

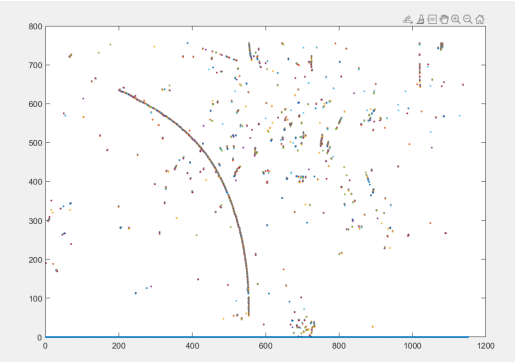

(b) Re-Graphed Image T#:6-0.68

Figure 15: Object Definition

4.1.5 Definition of Deflection

Object deflection is defined as the maximum forward deflection of the tip from the initial position relative to the object base. Forward motion is defined as the motion of the bulk of the object in the forward direction. This can also be defined as the deflection at the moment the bulk of the object reaches a net-0 velocity. After deflection, when the object starts to move back toward its original position it often happens due to the thinness of the tip that it will deflect even more due to fluid viscous forces. While this could be taken as the maximum,

it is disregarded. The main component of interest is the effect of the forward motion of the wave on the object. Taking only from forward motion also removes the effects of secondary modes of bending at the tip. The peak deflection will only be taken at the instance when the object no longer moves in a forward direction. See Fig.17

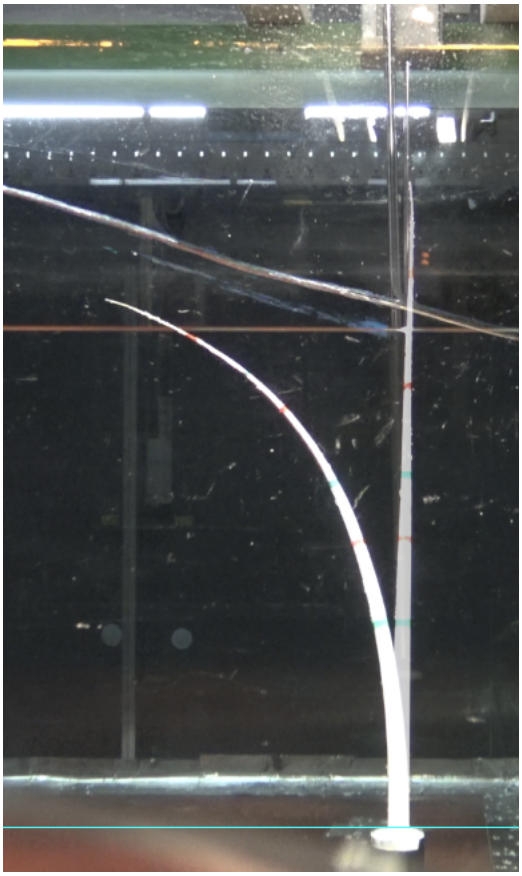

Figure 16: Example of Tip Deflection Off of Initial Position

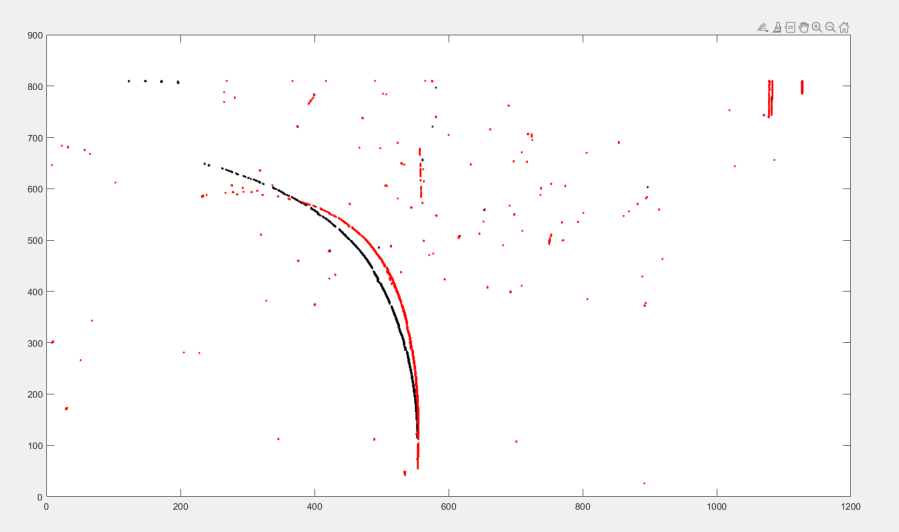

Figure 17: Forward Deflection (Black) Vs Peak Deflection (Red)

This figure views test 6, the 1.23-period wave with an Hm0 of 0.18m at a WL of 0.68 on the 7.5Mpa medium.

In this situation, the black (time: 31.56s) is the forward motion-induced deflection, and the red is the peak deflection the tip of the cone undergoes. The tip of the object at the maximum (red) (time: 31.6s) goes through significantly more bending however, tracing the line we can see the bulk of the object has started to deflect back towards its initial position. This combined with the resistance of the water induces this extra bending. To ensure that the bending initiated by the forward motion of the waveform is used and consistent, the maximum forward deflection is taken while the bulk of the object is moving forward or stopped (black).

4.1.6 Quantifying Deflection

The calculation of the deflection of the object is found by creating two rays from the base point. One is at the object's resting point before the water is disturbed. The second is from the base point to the tip of the object during maximum forward deflection.

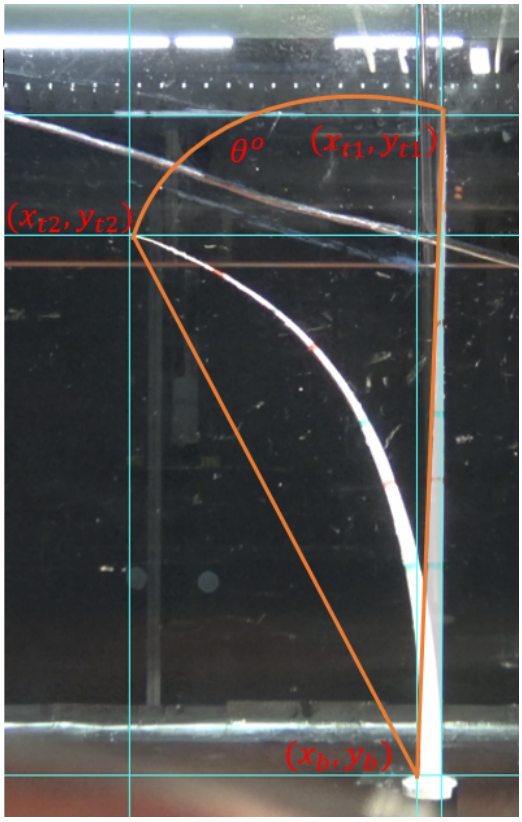

Figure 18: Deflection Example

To find the deflection both rays are converted from Cartesian coordinates into slopes. By taking

$$m_n = \frac{|y_t - y_b|}{x_t - x_b} \tag{29}$$

for both points where x_b, y_b are the base points, and x_t, y_t are the coordinates at the tip of the object. To find

the angle of the rays relative to one another the equation:

$$tan\theta = \left| \frac{m_1 - m_2}{1 + m_1 * m_2} \right| \tag{30}$$

is applied where m_1 is the slope from the base to tip in the starting position, and m_2 is the slope from base to tip in the position of maximum forward deflection (θ), this is solved for theta in radians then converted to degrees using the relation $rad * \frac{180}{\pi}$.

4.2 Quantitative Analysis

4.2.1 Wave Gauge Correlation

To find the forces on the mimic, the forces of the mount must be removed from the data. As the Mount and Mount-mimic tests must be run independently of one another, the data sets will not be perfectly in sync in time. To combat this the data sets must be correlated in time. To do this the function 'xcorr' is used in Matlab [**Buck et al. 1997**; **Stoica et al. 2005**] r = xcorr(x,y) returns the cross-correlation of two discrete-time sequences. This can then be used to shift the data sets so that the wave data is matching. All data sets are correlated using WG1 as it deals with the least noise. An example of this is shown in the following figure. The full calculations can be found in Appendix B Section 1.

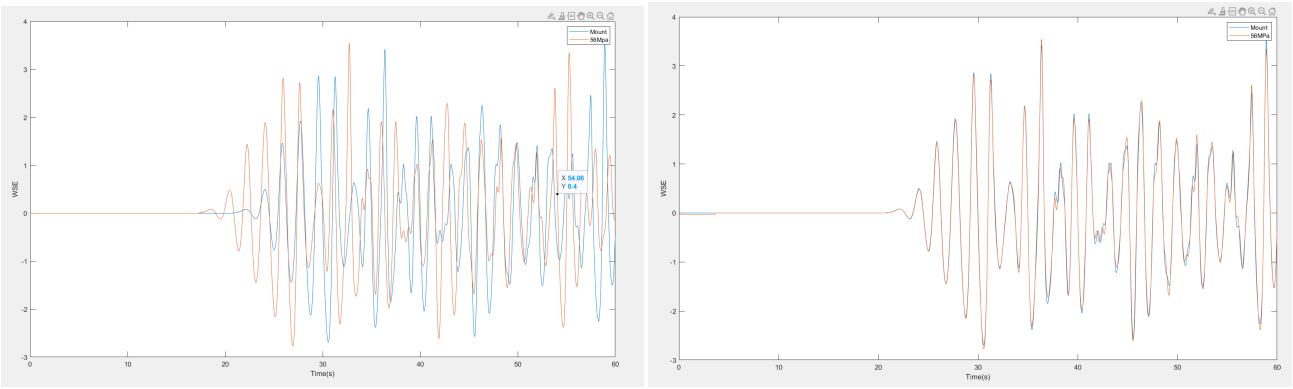

(a) Uncorrelated Data

(b) Correlated Data

Figure 19: Data Correlation Example

4.2.2 Force Separation

The recorded data includes the forces on the mount from separate tests. As well as the overall forces on the canopy and mount combined recorded by the force gauge. Once the data is correlated then the forces from the mount are subtracted from the total forces induced by the mount-canopy combination to find the forces induced by the canopy alone. An example is provided in the following figure. The blue line represents the combined Canopy-Mount forces. While the orange depicts the forces on just the canopy after the mount data has been removed. Full calculations can be found in Appendix B Section 2

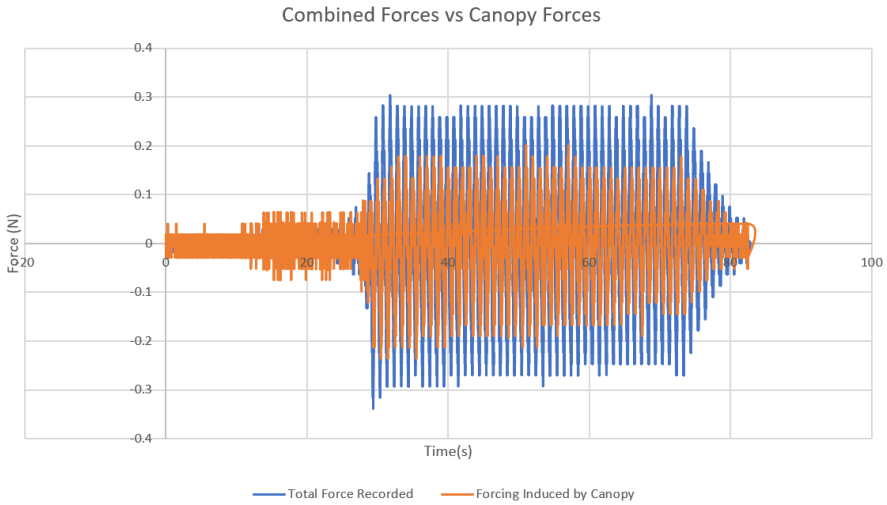

Figure 20: Force Removal Example Flex Fork WL:0.68 m T_p:1.00 s H_{m0}:0.14 m

4.2.3 line-up Error

The above process of force correlation is done by lining up the data at a frequency perfect match 1/200 Hz however in rare cases the data may require a shift of 1/400 Hz in which case it is rounded to the nearest whole 1/200 Hz and then shifted the error that this generates is rather negligible on the total and peak forces. The maximum error in peak forces across all data sets based on an offset was 1.33% of the peak force. This shift is also twice the actual effect that could occur in a data set. See Appendix B-4 for calculations.

4.2.4 Force Peak Separation

The peak forces generated on the mimic in each test are separated from the data using the function 'FindPeaks' in Matlab. All highlighted points are recorded and placed into a matrix along with the average of the 3rd through 13th points. Data is taken at the third point to guarantee the wave is fully spun up and stopped at the 13th to ensure no reflections are taken into account. The average of these 10 points is the F_p used for calculations in the results section. See the following example Fig. 55. Full calculations can be found in Appendix B Section 3.

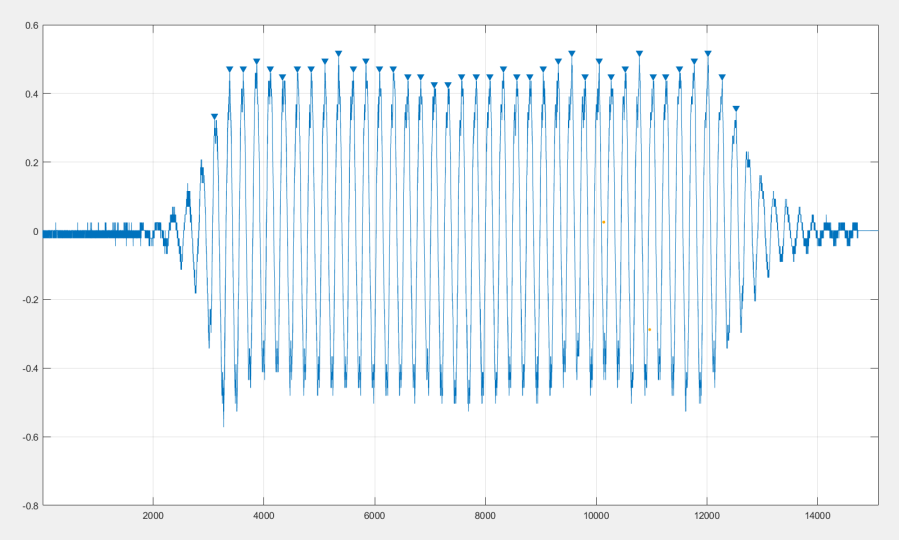

Figure 21: Peaks

4.3 Forcing Checks

Forcing values need to be taken as a check for wave damping, and whether bending and change in flow regimes have an active effect on force. An estimation of the forcing will be calculated through the approximation of forcing on a cylinder, applied over multiple points on the cone to generate the average force based off of eq.(4)

$$f_d = \Sigma_{n=0}^{n=i} 1/2 \rho \delta_y C_D U_{ref}^2 \tag{31}$$

C_d can be calculated one of two ways, using the Reynolds number Re eq.(9) or the Keulegan-Carpenter number KC eq.(19). For the Reynolds approximation eq.(8) can be used. For the Keulegan-Carpenter number based on previous literature, a coefficient will be determined using the data generated from the stiff mimics with the following formula.

$$C_D = \alpha (KC)^{\beta} \tag{32}$$

5 Results

5.1 Thin Cones

In the 0.68 and 0.53 WL tests for the thin cones, phenomena occurred where the 400 Mpa cones simply followed the shape of the wave more so than active deflection. Likely due to the object having low enough inertia and bending resistance that it simply followed the orbital path of the fluid instead of deflecting and then attempting to revert to its initial shape and position. The thin cones were so easily affected by the waveform that they started to permanently warp from the tests. Due to this the thin cones are no longer included as part of the analysis in this data set.

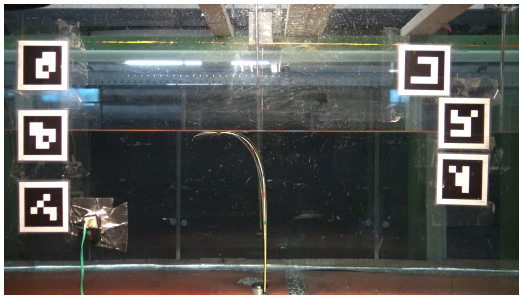

(a) Thin Cone Initial WL:0.68 m T_p:1.23 s H_{m0}:0.18 m

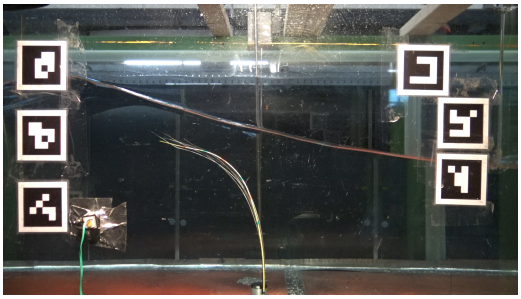

(b) Thin Cone Final WL:0.68 m T_p:1.23 s H_{m0}:0.18 m

5.2 Inertia-to-Drag Ratio

The Keulegan-Carpenter Number (KC) $\frac{UxT}{\delta_y}$ is the ratio between the inertia-to-drag ratio of the object in relation to the flow of the fluid around it. When looking at the KC# with respect to the data gathered in the testing a few things immediately become apparent. There is a strong relationship between the KC# on a single object and the corresponding motion of the object underflow. As we can see in the following figure Fig.23 across all tests changes in deflection closely follow changes in the inertia-to-drag ratio.

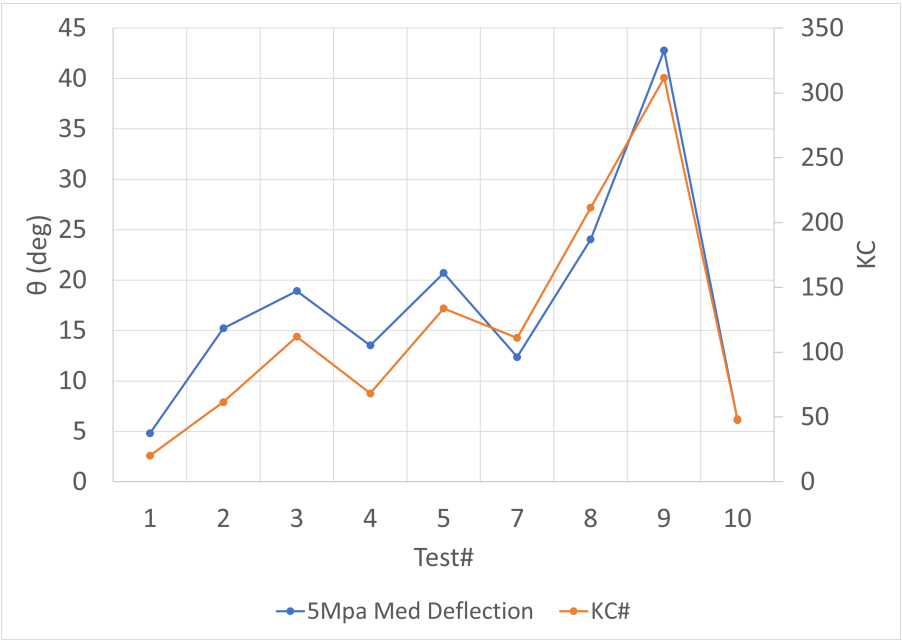

Figure 23: KC and Deflection Across WL:0.68 m Tests for 5Mpa Medium Cone

Indeed, once the data is organized, a nice fit in figure 24 is demonstrated across a single object. At a constant water level, this generates a very strong correlation between the deflection of the object and the inertia-to-drag ratio felt due to flow.

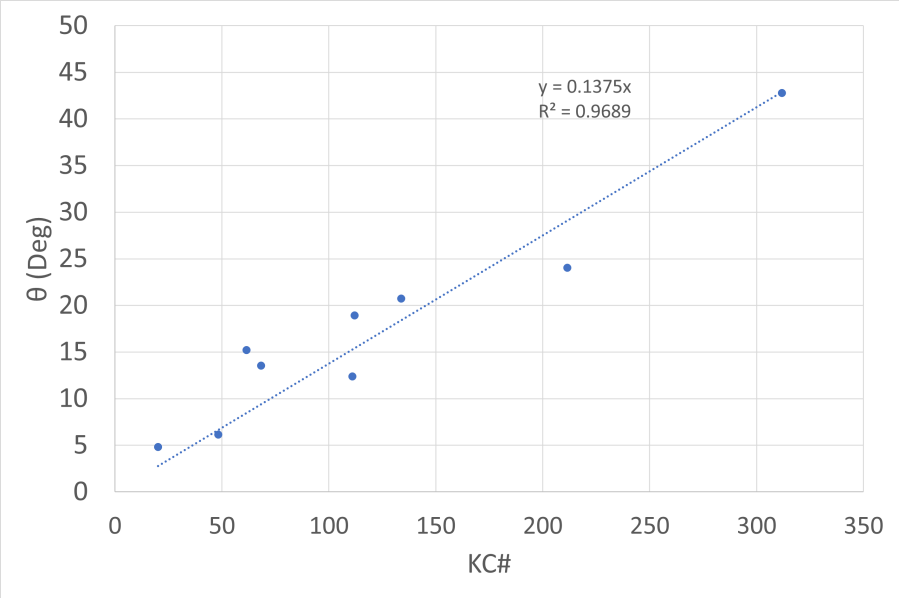

Figure 24: KC Vs Deflection WL:0.68 m 5Mpa Med

However, where this falls short is object stiffness. As the E-Moduli of the object changes the slope of the line will increase or decrease. With a higher E-Moduli, the object will deflect less even with the same KC number. This can be seen in the following figure 25 which displays the different amounts of deflection relative to the different stiffness of same shape objects.

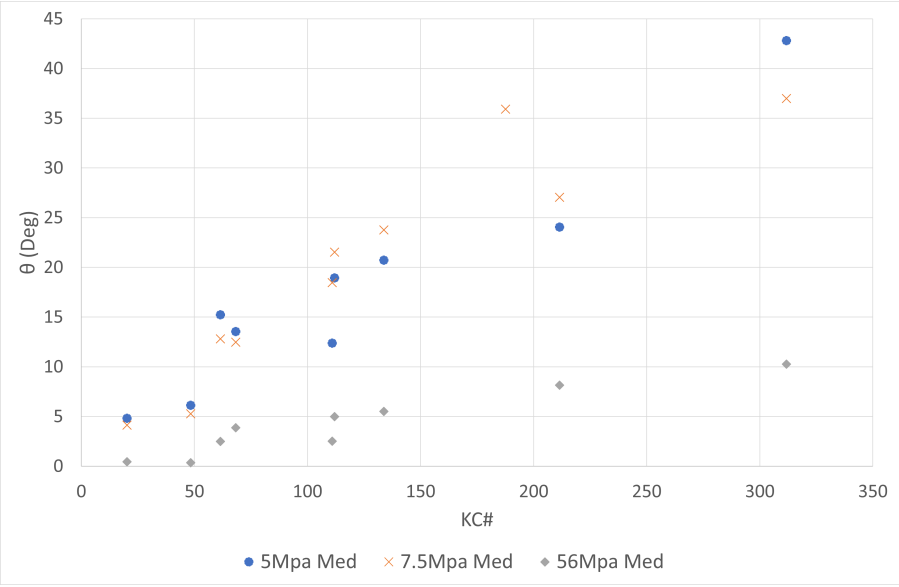

Figure 25: KC Vs Deflection WL:0.68 m Med cones

In theory, across differently-sized objects with the same E, the KC should relate the two relatively well. However when looking at the ratio between the object's deflection and the KC number ie) Def/KC across the tests of the large and medium cones it can be seen that the Deflection/KC values do not match, in fact, there is a large disparity between points.

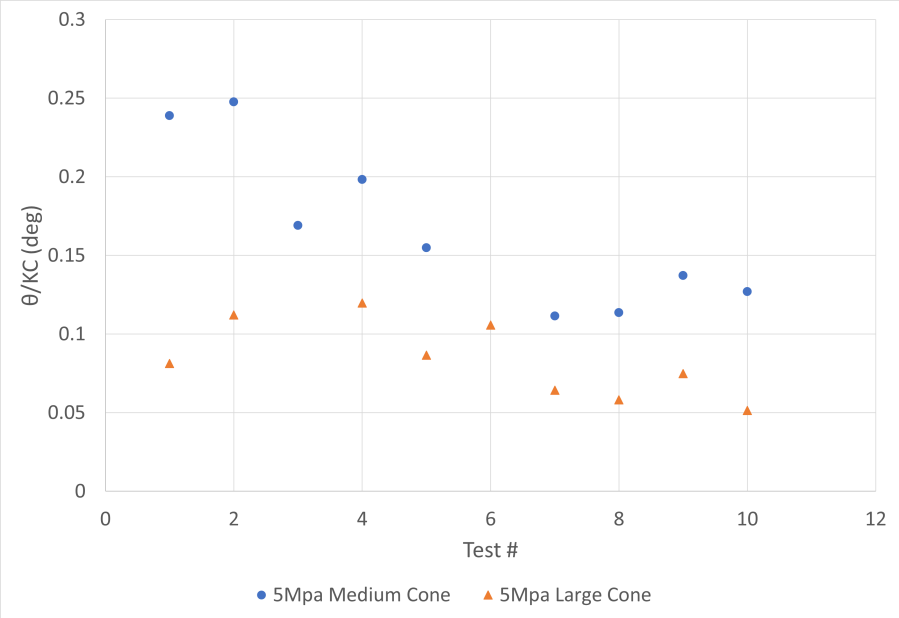

Figure 26: Deflection Over KC WL:0.68 m 5Mpa

As seen in the above graph, the objects do follow the same trend of deflection. There is still a disparity in the ratio of deflection and KC. Where the smaller object deflects more relative to its KC number than the larger object even though they share the same material properties, and the same principal shape (Cone).

5.3 Force-to-Stiffness Ratio

The Cauchy number $\frac{\rho U_{ref}^2 l^3 \delta_y}{EI}$ represents the force applied to the object relative to its resistance to bending, which gives the relative stiffness of the object. Similarly to the KC number as the Cauchy number increases so too does deflection. However, the Cauchy would predict that a 5Mpa large and medium cone would be going through the same force relative to the resistance.

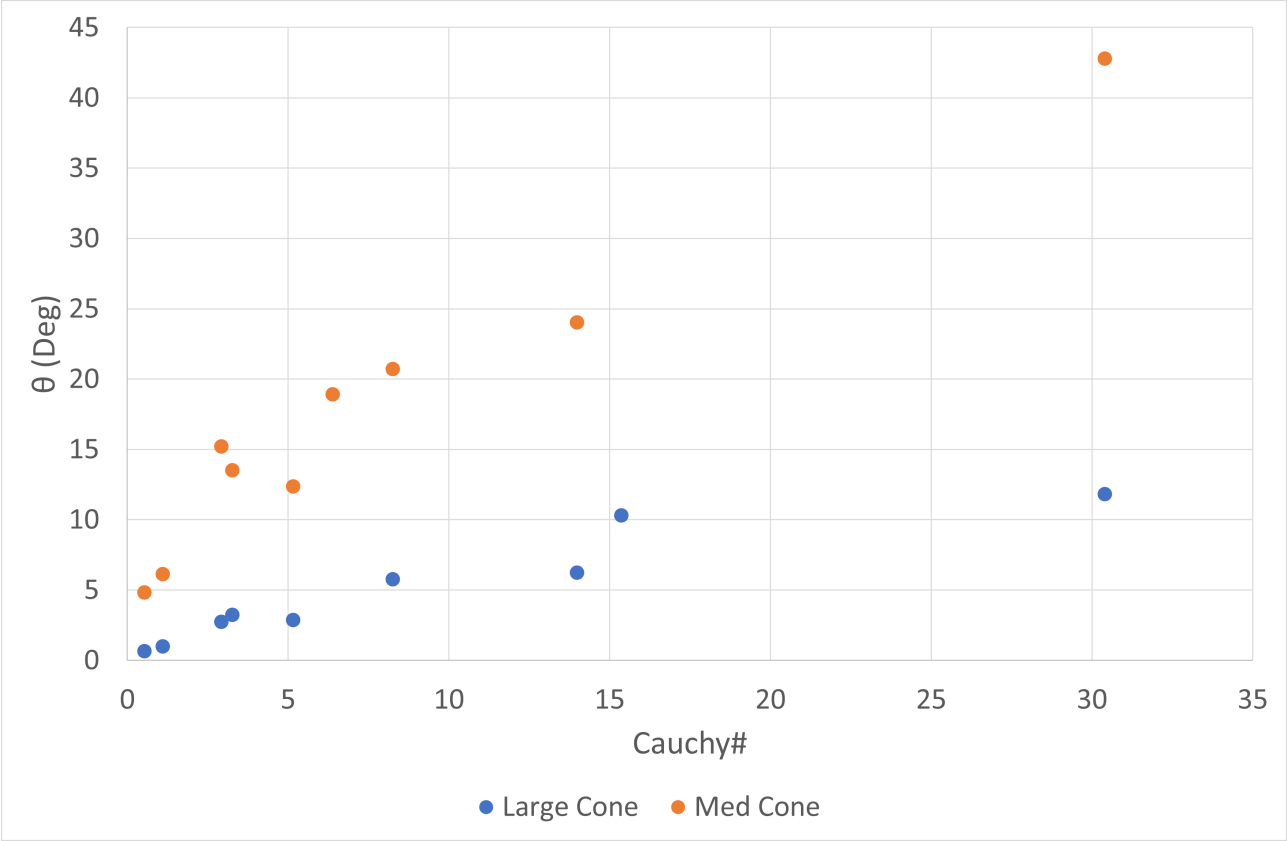

Figure 27: Deflection Vs Cauchy WL: 0.68 m 5Mpa Cones

As seen, in the above figure 27 this is not the case for the objects in question. Instead, there is a large separation between the amount of deflection between the two objects even though they feel the same amount of force-to-stiffness ratio. While there is a good indication of prediction among singular objects it fails to capture the full scope across different sizes.

5.4 Wave Period T_p

In this section, we will be looking at the effects of a changing wave period on the stiffness of an object. The most consistent tests for this are tests 2,4, and 7 at the 0.68-meter water level. Each test has an incident wave of roughly 0.1 meters with little skew relative to one another. With, respective wave periods of 1.00, 1.23, and 1.77 seconds. Based on WG data the average impact height of the wave peak is 0.401, 0.402, and 0.407 meters up the cone, ie. All roughly the same impact points in this we can assume that the effects of Hm0 and skew are negligible when looking at the data. Taking a look at the Medium cones (0.0137) deflection across these different waves and their peak forces see figure 28.

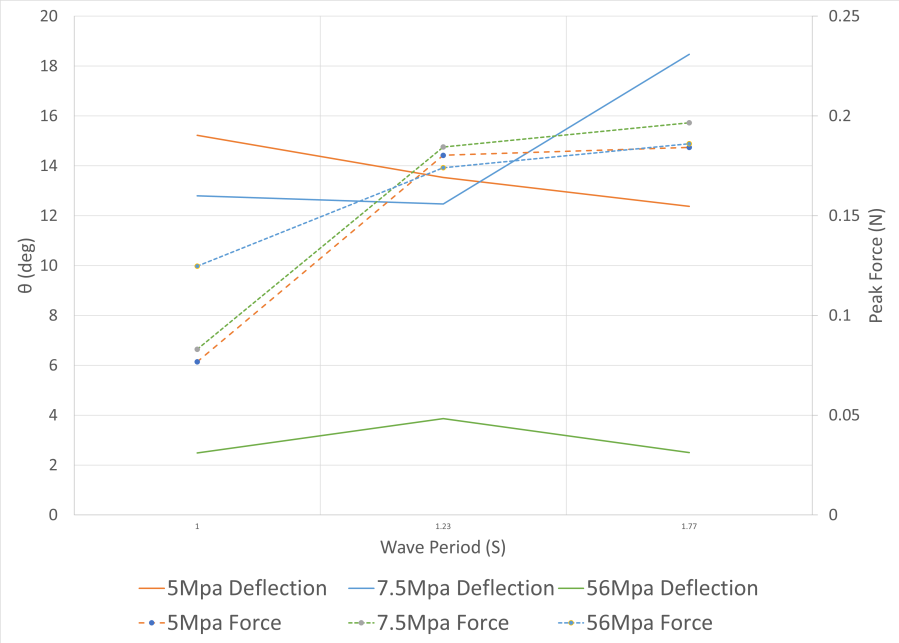

Figure 28: Deflection and Peak Forces Across a Constant Wave Height Wave, and Different Periods, For Medium Cones WL:0.68 m Tests: 2,4,7

Looking at the 5Mpa medium cone in singularity we see that as the wave period increases the object deflection decreases. Each increase in wave period decreases the deflection. Starting at 15 degrees down to 12 degrees by the 1.77 second period. While the peak force was at 0.076 N at the peak for the 1-second wave and 0.18 N for both the 1.77 and 1.23-second waves. This would indicate that as the wave period increases, the deflection decreases however it does not explain why peak force is not changing. Nor why the forces are so low for the 1-second period wave. While the 7.5 and 56Mpa variants do not decrease, in fact, the 7.5Mpa cone increases in deflection, while the 56Mpa increases in test 4 and then decreases in test 7. To further assess the effect of the wave period it would be prominent to look not at the peak forces generated but at the wave flux as a representation of average energy.

5.5 Relative Flexibility to Wave Energy

A rough look at the data shows that there is a distinct correlation between the object's flexibility and the amount of force it can exert on the surrounding flow. It should be noted that the separation between the points also increases with increasing wave size as seen in the below figure, Fig.29

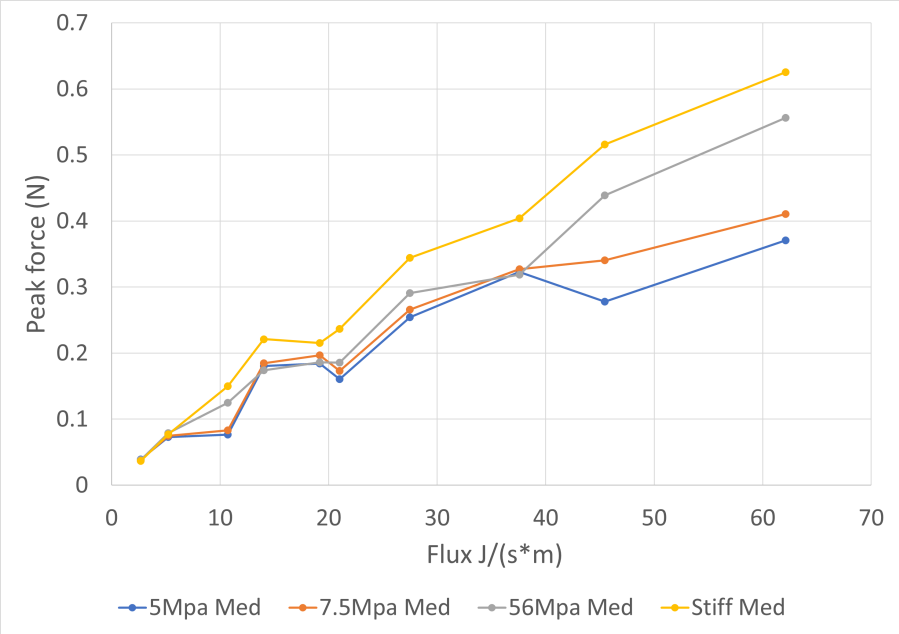

Figure 29: Peak Forces Vs Flux WL: 0.68 m

we can see that as a general trend as the wave increases in size so too does the separation in the forces. In fact, this shares a direct correlation with the peak deflection of the object as well. When then using the same X-axis we can see that if the deflection of the flexible objects is against the flux there is a positive correlation.

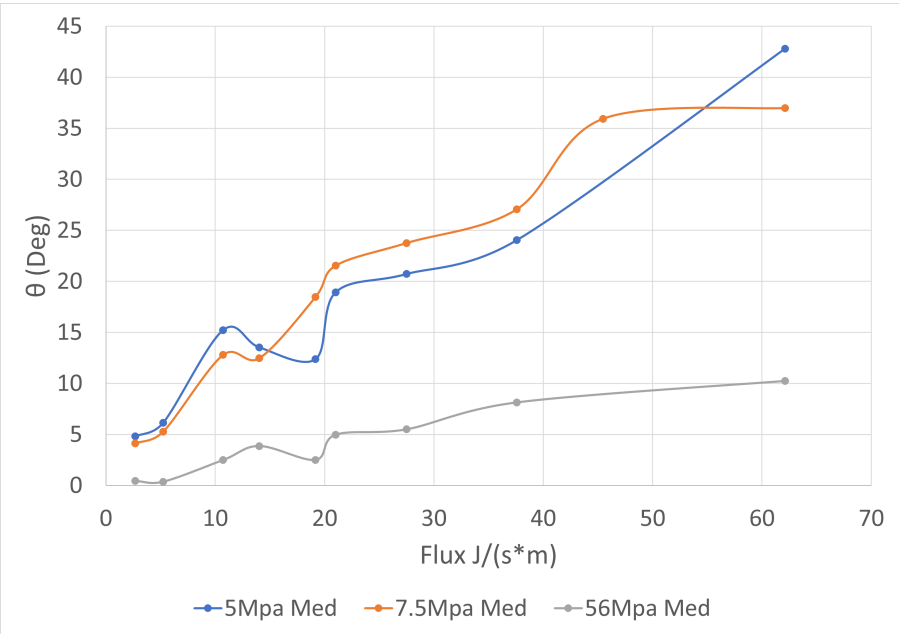

Figure 30: Deflection Vs Flux WL: 0.68 m

Generating a very sensible relationship where the larger a wave ie) the more incumbent energy, in general, the more the object will deflect. However, when looking at the peak forces applied to the object relative to those of a stiff object we see that there are multiple peaks generated where there is a large separation in the peak forces

of the object. Where it does not necessarily increase with increasing wave energy.

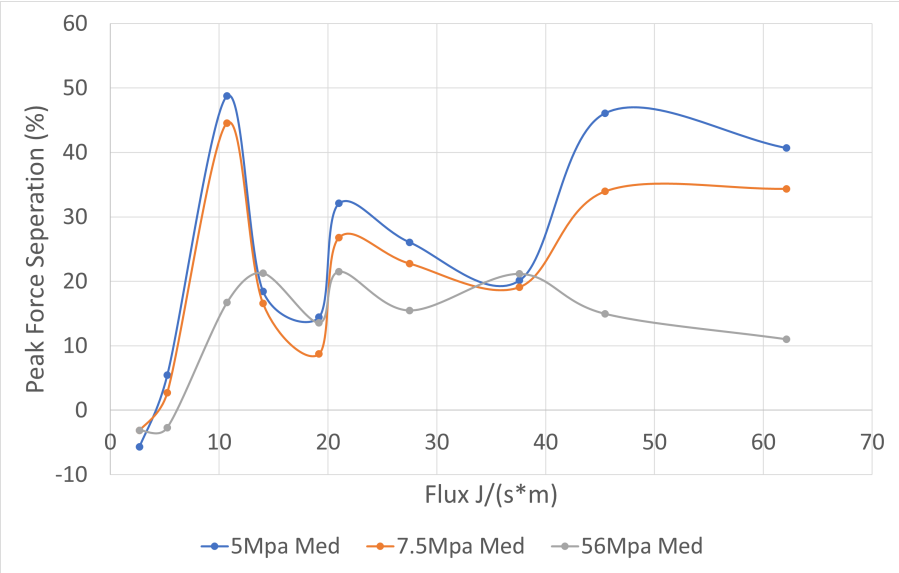

Figure 31: Percentage of Peak Force Difference Vs Flux WL:0.68 m

These two local maxima occurring at the 3rd and 6th positions on the graph might be explained when we consider the findings of [**keulegan et al. 1958**] as both these tests, deal with a 1-second period wave which induces a high rate of change in orbital velocity. This first peak of the wave for the medium cones has a KC value ranging from 20-100 depending on the diameter which places part of the object inside the peak seen in graphs peak and trough respectively.

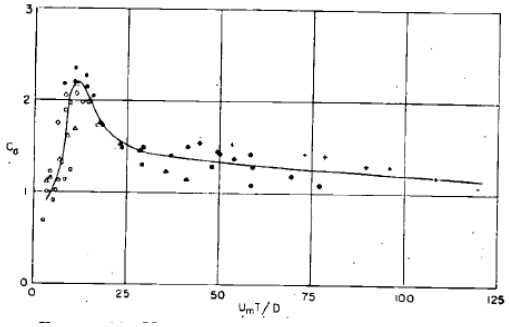

(a) KC Vs Drag Coefficient [**keulegan et.al. 1958**]

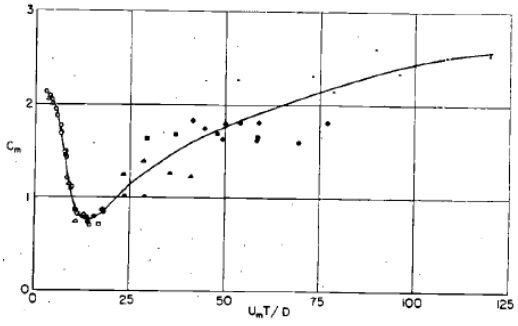

(b) KC Vs Inertia coefficient [**keulegan et al. 1958**]

The available system energy in the form of the C_d is quite high for this combination which in turn applies a larger force more rapidly to the flexible objects this then causes it to deflect and reduces the peak forces felt by them. What this implies is that the rate at which the orbital velocities of the wave pass through the object has a large impact on the applied force and thus the flexibility of the object.

5.6 Wave Height

The wave height Hm0, which across the same period has the straightforward trend of increasing the deflection, peak, and average forces on the object. As it increases in height, the orbital velocity also increases. Also as a partially submerged object the amount that is impacted by the wave increases. Looking at the stiff medium cone for the 1.00 second wave period across three wave heights 0.05, 0.1, and 0.14 then the trend is apparent.

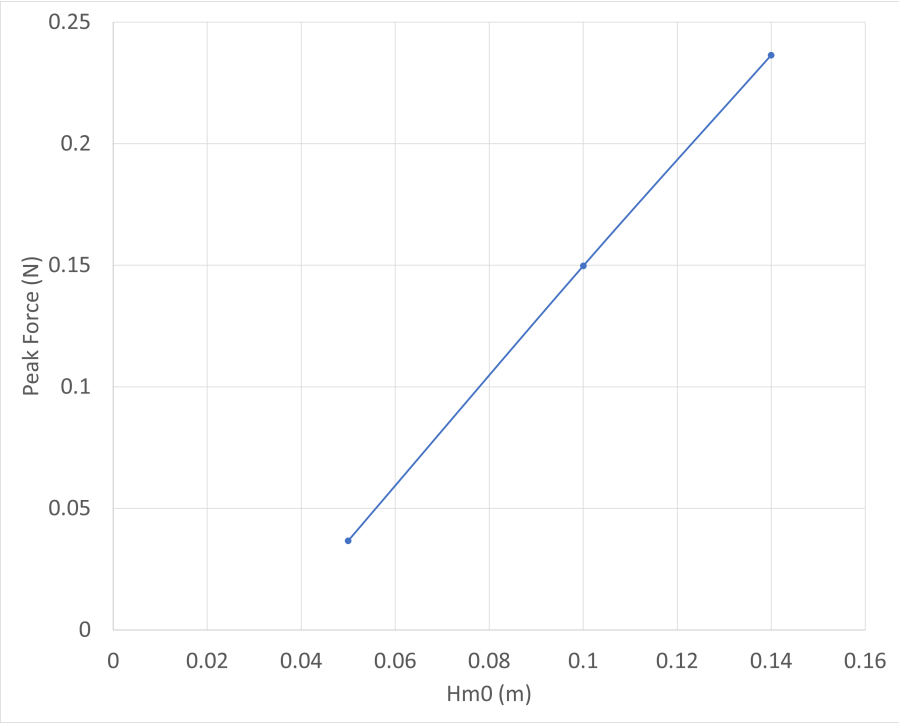

Figure 33: Force Vs Wave Height Stiff Medium Cone WL:0.68 m T_p:1.00 s

holding period constant at 1 second for the following wave heights we can see that the object has a direct correlation with the increase in force being applied. When then applying this to deflection again in fig.**??**

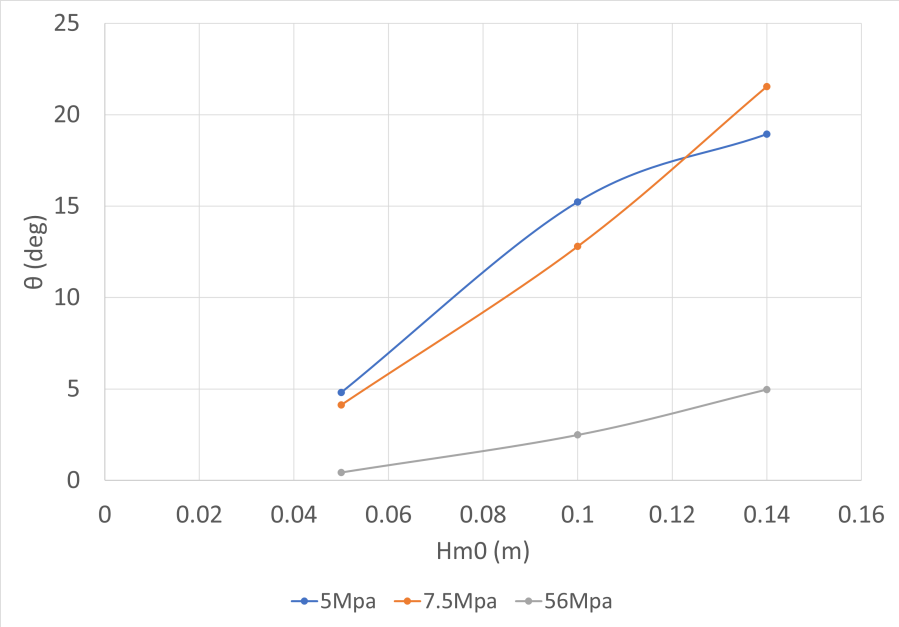

Figure 34: Deflection Vs Wave Height, Flexible Medium Cones WL:0.68 m T_p:1.00 s

As the relationship for each object is relatively linear, the Hm0 which is directly correlated to peak force increases then the deflection also increases in a similar manner.

5.7 Impact Height

Another factor is the peak WSE of the wave as the wave becomes more cnoidal the wave generates a skew around the x-axis with higher peaks and a shallower trough. In the testing series, there is a range of waves tested. With many fully Cnoidal waves, while Hm0 stays constant. The relative max surface elevation, and minimum surface elevation change. Which based on linear and Cnoidal theory allows the peak of the wave to travel faster through the relation $c = \sqrt{g(d+\eta)}$. For a partially submerged object, this also means that the wave will impact more of the object as more of it will be within range of the wave. When looking at the 0.1 Hm0 wave in the 0.53 water level where it feels the bottom and therefore goes through more skewing as it shoals we can see across three periods that the peak forces on the stiff object increase with increasing peak WSE, fig.35

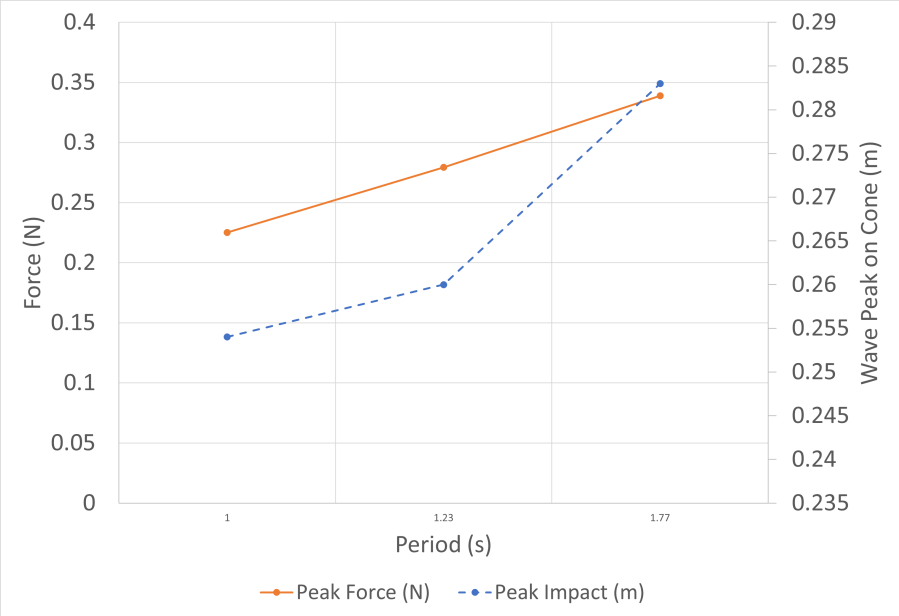

Figure 35: Medium Stiff Cone Deflection Vs Peak WSE WL: 0.53 m H_{m0}: 0.1 m

The larger the skew, the more area is available for forcing. This, in turn, generates an increase in peak force which, causes the object to deflect to a greater degree. There are some discrepancies in the deflection. However, this can be attributed to the wave sets and the possibility for the object to reach a resonance or other flow effects. This seems to have occurred for the 7.5Mpa cone on the 1.77-second 0.1-meter wave and would explain the increase in recorded deflection.

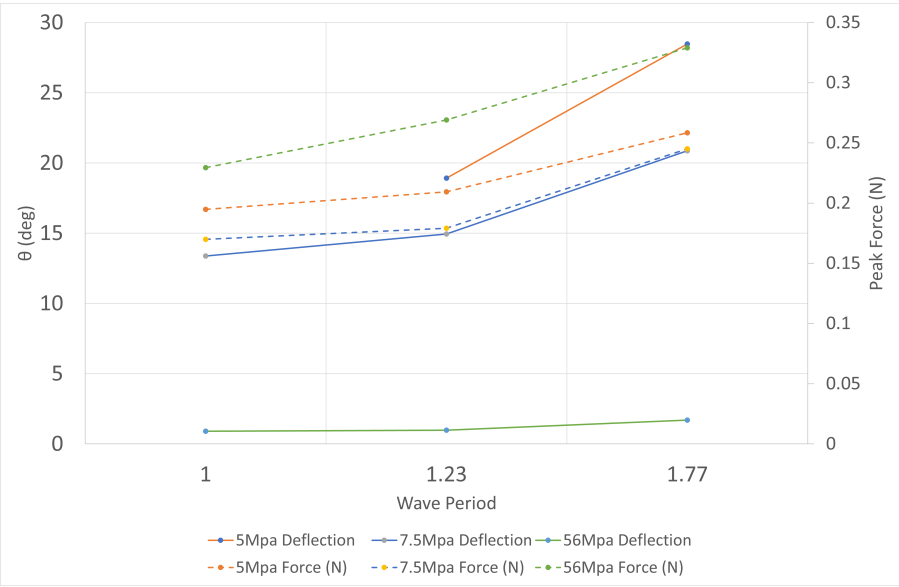

Figure 36: Deflection & Force Vs WSE, Flexible Medium Cones WL:0.53 m Hm0: 0.1 m

As seen in the above figure for the flexible medium cones the increase in WSE which increases impact area for a partially submerged object has a positive impact on the deflection. Also increasing the peak force F_p generated

on the object.

5.8 Expected Forces

Using the WG as the baseline for peak WSE we can adjust the expected max wetted area of the mimic instead of simply using the wave height. As the amount of the mimic impacted the wave will affect the final force. Using the equations 31 where the drag coefficient is calculated from eq.(8)

$$C_D = 1 + 10Re^{-2/3}$$

are then applied to the adjusted wave velocities using the approximate Cnoidal wave velocities discussed in the section on Wave types in the literature review. leading to expected peak forces across all tests on the stiff objects for the following:

Table 5: Expected Peak Drag Forces (Newtons)

WL (m)		
0.68		
Test#	Medium	Large
1	0.0122	0.0291
2	0.0562	0.1364
3	0.1113	0.2676
4	0.0627	0.1528
5	0.1400	0.3395
6	0.2537	0.6167
7	0.0950	0.2326
8	0.2291	0.5607
9	0.4923	1.2113
10	0.0242	0.0583
0.53		
Test#	Medium	Large
1	0.0206	0.0500
2	0.1177	0.2907
3	0.3385	0.8407
4	0.1453	0.3594
5	0.2948	0.7318
6	0.1475	0.3648
7	0.3024	0.7509
8	0.3084	0.7658
9	0.2961	0.7350
10	0.0493	0.1210

These are the forces expected to occur at the wave peak, at this exact moment the change in velocity of the wave is entirely in the vertical direction, $F_i = 0$ and $U_{ref}\frac{du}{dt} = 0$ These forces are off by a large factor when compared to the recorded peak forces which are believed to have something to do with the effects of wave impact especially since these objects are partially submerged which could result in the surface tension from an unbroken wave having a greater impact on the object, ie) the passage of the object from air to fluid, and possibly

the shear forces induced by the waves as well. This generates a large disparity between the peak recorded Vs. actual forces, thus a drag coefficient was generated using the following equation:

$$F_d = \frac{1}{2}\rho\overline{C_d U}_{ref}^2 A \tag{33}$$

Where $\overline{U}_{ref}$ denotes the average velocity felt over the object, and A the active frontal area of the object. The above forcing equation is used as a baseline based on previous literature. The active testing range was between a KC of 5 and 312. The following drag coefficient equations were then derived from the data. Resulting, in a drag coefficient equation for large cones of

$$\overline{C_d} = 27.11(KC_a)^{-1.079} \tag{34}$$

and medium cones of

$$\overline{C_d} = 21.314(KC_a)^{-0.764} \tag{35}$$

where KC_a is the average KC number over the cross-sectional area of the object. It is important to note that, this is only applicable to partially-fully submerged conical, stiff vegetation. The drag coefficient is applicable only for non-breaking, fully spun-up regular waves, without reflections. Generating the following numbers in table 6.

Table 6: Adjusted Peak Forces

WL (m)		
0.68		
Test#	Large	Medium
1	0.257	0.076
2	0.646	0.270
3	1.243	0.519
4	0.472	0.204
5	0.971	0.421
6	1.357	0.628
7	0.352	0.175
8	0.714	0.352
9	1.022	0.568
10	0.128	0.050
0.53		
Test#	Large	Medium
1	0.250	0.066
2	0.587	0.209
3	0.999	0.433
4	0.507	0.199
5	0.720	0.321
6	0.511	0.200
7	0.472	0.234
8	0.477	0.237
9	0.467	0.230
10	0.197	0.071

Which, generates the following figure of the fitted data:

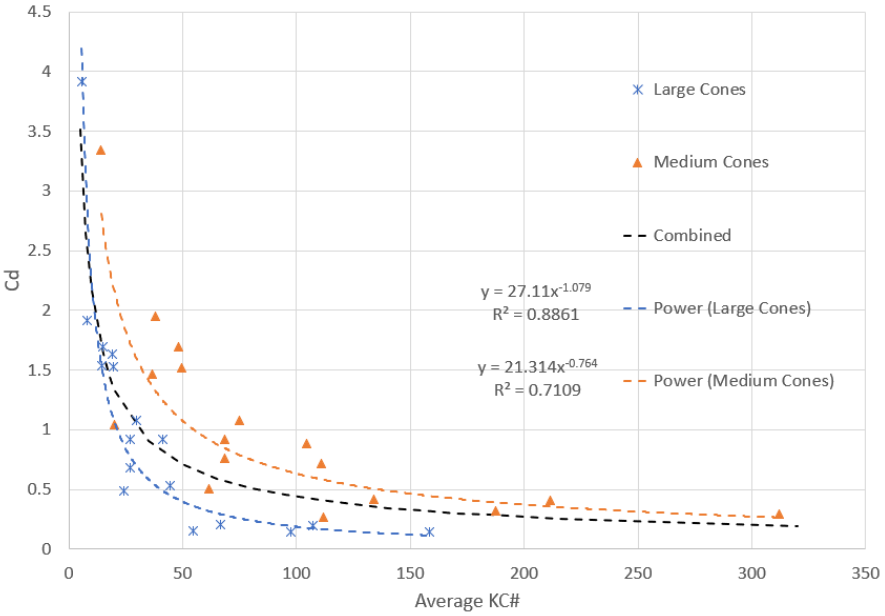

Figure 37: Drag Coefficient Calibration

While a decent indicator of the peak force felt by the cones. This is unfortunately only applicable to the stiff variants. It is difficult to predict the deflected forces (flexible objects) with the general forcing equations without using a CFD. The forces are generated roughly based on the speed of the object relative to that of the surrounding flow. As the object mobilizes two more factors are required to predict force, the speed relative to force as well as the degree of deflection of the object or angle to the flow.

6 Analysis

6.1 Adjusting Numbers

In this section, the aim is to try to consolidate the important variables defined in **Section 3.3** into a more applicable number for the prediction of θ. The number should bear similarities to the Cauchy and KC, as from testing they are good predictors of deflection when looking at a single object. However, fails to capture changes in shape and complexity. With this in mind a new number which starts similarly to Cauchy where the stiffness of the object to force is captured in this case using

$$\frac{F_p}{EI}, [L^{-2}] \tag{36}$$

this then captures the effects of flow, wave height, as well as its relative stiffness essentially a variation of Cauchy, F_p is essentially flow with a drag coefficient included. Next, the range of impact needs to be added as we found

above the peak wetted branch length or η_p has a significant impact on top of wave height resulting in the following equation.

$$\frac{F_p \eta_p}{EI}, [\frac{1}{L}] \tag{37}$$

Following this to non-dimensionalize the number the shape factor of the volume / frontal area is added which results in $\frac{\pi r}{3}$ since all of these objects are of the same shape we can remove the $\frac{\pi}{3}$ leaving r resulting in the following equation:

$$\frac{F_p \eta_p r}{EI}[-] \tag{38}$$

This still results in an imperfect view of the data, finally multiplying this by another dimensionless number which is the slope of the object ie the ratio of the object diameter to its length.

$$S = \frac{l}{\delta_{y,base} - \delta_{y,tip}} \tag{39}$$

It was found that cubing the slope (S) provided the best fit for the data which results in the following number.

$$\frac{F_p r \eta_p S^3}{EI}[-] \tag{40}$$

Breaking down the number into numerator and denominator we find the numerator containing

$$F_p r \eta_p l^3 \ ([MT^{-2}L^6]) \tag{41}$$

while the denominator has.

$$EI(\delta_{y,base} - \delta_{y,tip})^3 \ ([MT^{-2}L^6]) \tag{42}$$

Importantly we now have the force and a shape in both the numerator and denominator. This number while bearing a strong similarity to the Cauchy number from which it was derived bears one key difference. The numerator and denominators of Cauchy bear the units of $[MT^{-2}L^3]$, while the new number places a stronger emphasis on the length units $[L^6]$ regarding the object. This provides a better view of the motion of conical vegetation. Which unlike cylinders do not have a constant cross-sectional area.

Applying both the large and medium data sets across both water levels the following figure is generated.

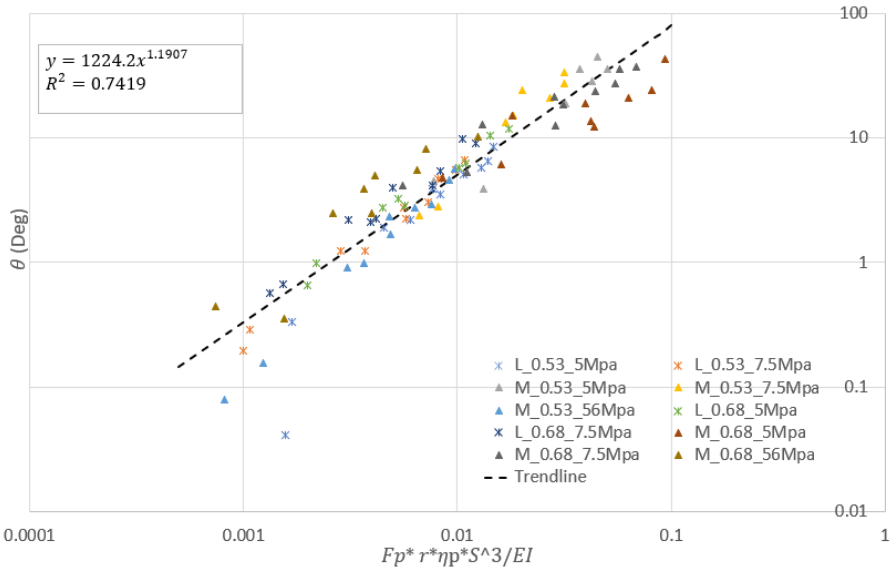

Figure 38: All Data Points Large and Medium Cones

Theoretically, using this curve if someone were to apply a wave to a conical object, (as this is only run on conical objects it is improper to assume it works for others) then one could roughly predict the maximum tip deflection. First by calculating the force applied by the fluid due to flow, and the total object EI, generating this equation which bears a fit of $R^2 = 0.742$.

$$\theta = 1224 * (\frac{F_p r \eta_p S^3}{EI})^{1.19} \tag{43}$$

Where deflection is in deg, F_p, is in Newtons, and E is Young's modulus in Mpa, I is in m^4, and η_p is the peak impact in meters and S is the object slope or rate of tapering.

It is also important when looking at this equation to understand what each part represents to any random shape that would change the equation. Most importantly the values of r, η_p, S. r represents the ratio of the objects $\frac{Volume}{Area}$, η_p represents the moment arm from the base of the object, and S represents the rate at which the object changes in size. A Step-by-Step derivation of the equation can be found in **Appendix F**

6.2 Deflection Relevance

Keeping in mind the above equations and concepts. The following analysis will discuss at what point deflection becomes significant when reducing energy from waves for partially submerged objects. To find the deflective relevance the following definition is used. The threshold for relevant deflection of an object can be defined as the point at which past deflection, there is a significant change in the amount of force felt by the object, relative to its stiff counterpart under the same conditions. This can then be broken into two categories, peak and average forces. Where peak force F_p is the highest force in Newtons felt by the object during a wave used in the above analyses. The average force $F_a$is the force felt by the object in N/S during a wave.

6.2.1 Threshold for Deflection in Peak Forces

When looking at the peak forces felt by an object both tests #1, and 10 across both water levels 0.68 and 0.53 show an insignificant change in peak force across all objects except for the test #1 for the 5Mpa med cone at 0.53. This, however, is attributed to resonance as the 7.5Mpa object has around the same force as the stiff. 0.76 Newtons for the 7.5Mpa, and 0.78N for the stiff. Across these tests, the maximum recorded deflection is 6.1 Degrees occurring on test#10 for the 7.5Mpa Med Cone at the 0.68 WL. If the net is cast further across larger waves some 6-degree deflection waves can see a large change in the peak forces. Adjusting for this, we arrive at roughly 5.3-4 degrees of deflection the object can be considered stiff with the caveat that the wave must be non-breaking. The high impact of breaking waves causes large deflection force adjustments. If the objects are flexible enough they can accelerate rapidly from the induced forces. If the deflection of all objects under 5.5 degrees is plotted in relation to the peak force of the stiff and flexible variants ie) $\frac{F_{p,Flex}}{F_{p,Stiff}}$ the following graph is generated.

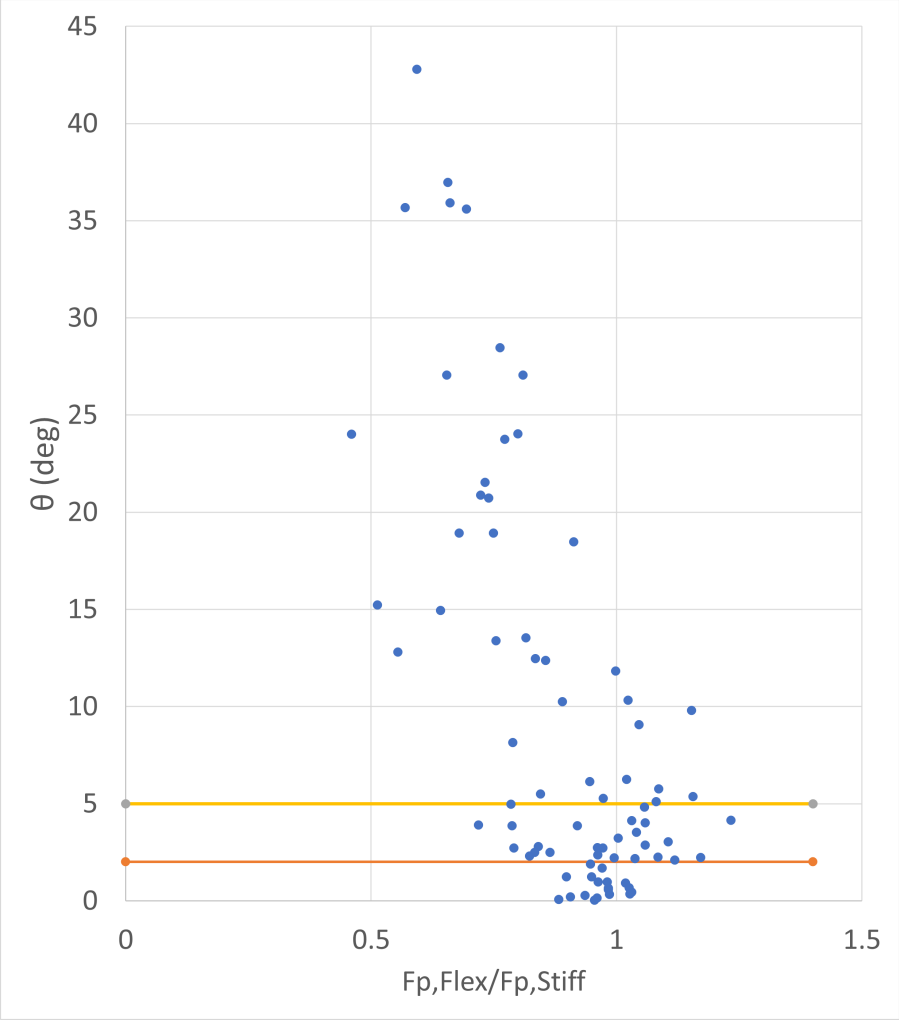

Figure 39: Threshold For Deflection of Relative Peak Forces

In general, as the deflection increases we see that the relative force of the flexible cones decreases when com-

pared to that of the stiff object. This becomes especially prevalent once passing a degree of deflection greater than 10 degrees, with the tightest ranges inside of 5 and 2 degrees. Looking specifically inside a range of 5.5 degrees we can better see the variation of the points.

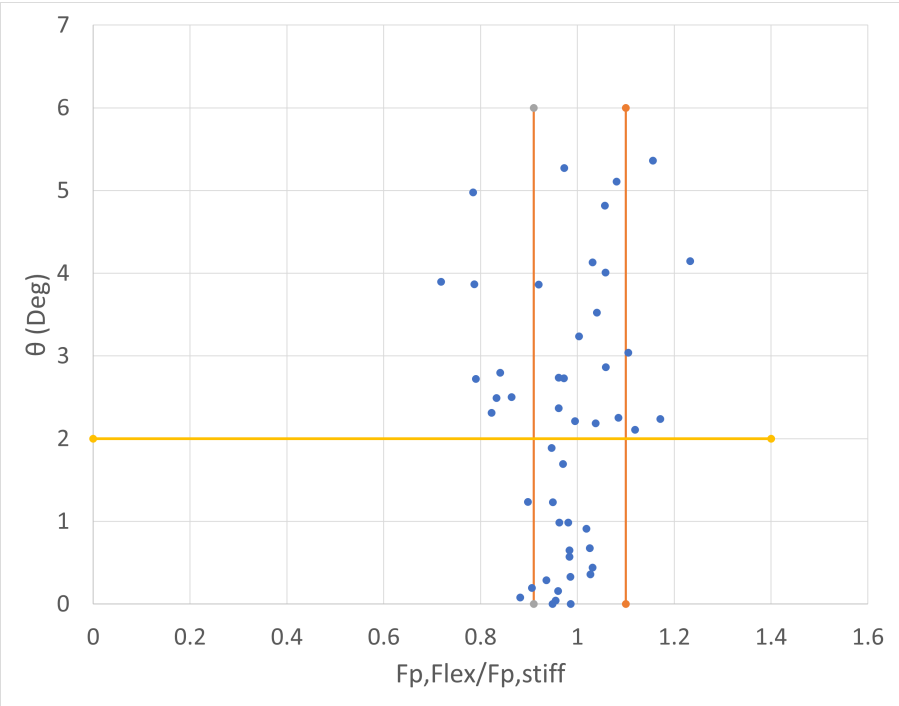

Figure 40: Threshold For Deflection of Relative Peak Forces Zoomed

Here we can see that most of the forces felt by the flexible objects are slightly less than, or even slightly greater than the forces felt by the stiff version. All within 0.2 of 1:1 which in most cases falls well within the 1st Std of the peaks. The average Std across these tests is 0.02947 Newtons and an average force of 0.394 Newtons placing the first Std of the $\frac{F,flex}{F,stiff}$ at a ratio of roughly 0.91 to 1.09 within this range roughly 69% of all points are accounted for. Points that fall outside of this could be due to a multitude of reasons. Most likely because the waves are done in sets, which, if the object has resonance, can easily affect the amount of deflection. As well as the forces felt at the peaks. Looking at the graph we see that after 2 degrees of deflection, the spread of the forces increases significantly. With this in mind, the tentative assertion is put forward that up until 5 degrees deflection is relatively inconsequential. However, past 2 degrees more complex effects can start to occur causing the peak forces of a stiff or flexible object to change. Still, in general, at 5 degrees or less the averages are focused around the 1:1 stiff-to-flexible ratio but there is a greater possibility for variation.

6.2.2 Threshold For Deflection in Average Forces

When looking at a threshold for average force (N/S) the values are far more blurry, plotting all the points within 1 Std. Against all the points under 5.5 degrees of deflection generating the following plot.

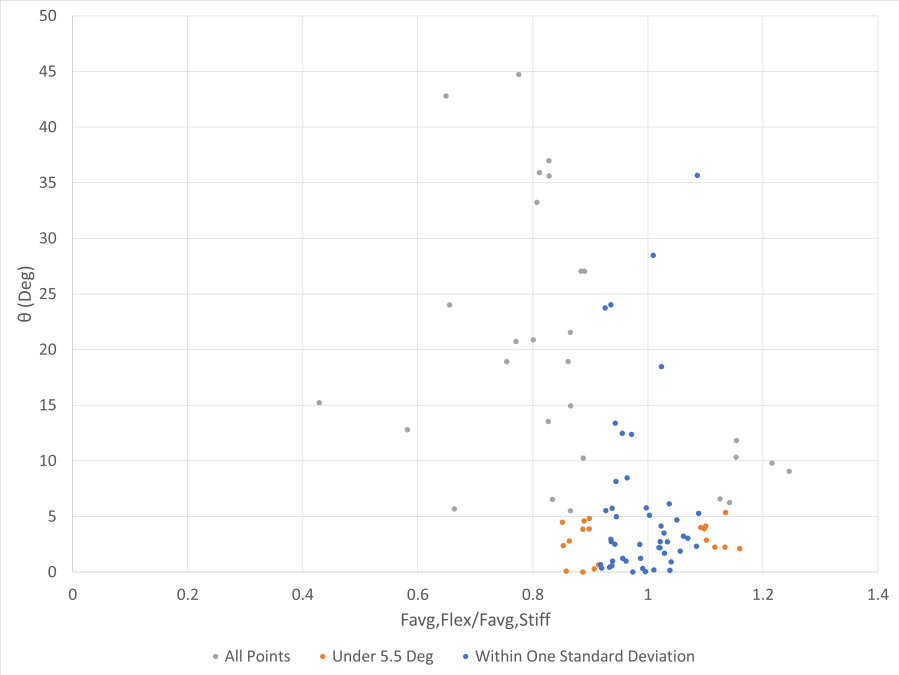

Figure 41: Threshold For Deflection of Average Forces (N/S)

The density of this plot is a bit more sporadic, indeed even looking at the bottom line ie) deflection>1 degree there is still a large spread, up to almost 1.2 F,Flex/F,Stiff. Implying, that even though the cone did not deflect a perceptible amount. there was still a decrease in the forces with no specific reasoning outside the test variability within the external testing conditions themselves. Small variations in initial water level, and wave generation. When looking at the data from WGs there is little to no variation in the time surface elevation from one test to another. Which, simply leaves the only explanation that there is variability occurring that cannot be accounted for. Moving forward, however, with this understanding when looking at the points we see the highest density within 0.8-1.2 F,Flex/F,Stiff is inside the 5.5-degree range. Especially, past 5.5 degrees the density of the points severely decreases within one std of the forces. In general, all the points are oscillating around 1:1, under the 5-degree line. With enough regularity that within 5 degrees the object can be considered stiff. However, this should be taken with a grain of salt as there is considerable chance based on this data for variability in the recorded forces. This variability does also occur around the stiff cones so it may simply have something to do with the material. Perhaps the small difference in the starting position of the objects on the mount, the exact flow in the tank, small variations in WL, and possibly small currents remaining between tests even though these were accounted for. However, as the waves are not steady flow in general this leaves more opportunity for variability to occur during testing through high frequency dynamical noise.

7 Discussion

7.1 Common Ratios

7.1.1 Difficulties in Force-to-Stiffness Ratio

The Cauchy number is generally the most used way to scale object flexibility for grasses between a model and prototype [**Jacobsen et al. 2019**]. Specifically cylindrical objects that have a constant cross-section. However, in this instance, the object is being used to mimic branches, and branches taper. Branches, as discussed by [**Kalloe et al. 2023**] have differing grades and sizes on a single tree. Most for the purpose of this work can be viewed as cones for a pollard willow, when going from a base to a tip they have varying sizes and thicknesses. If the Cauchy number is viewed through slices of the object's incremental force-to-stiffness or the incremental moment arm. The ratio over the object profile of the average Cauchy for the object is the same. It can be seen that across different shapes with a constant E modulus, an error is generated.

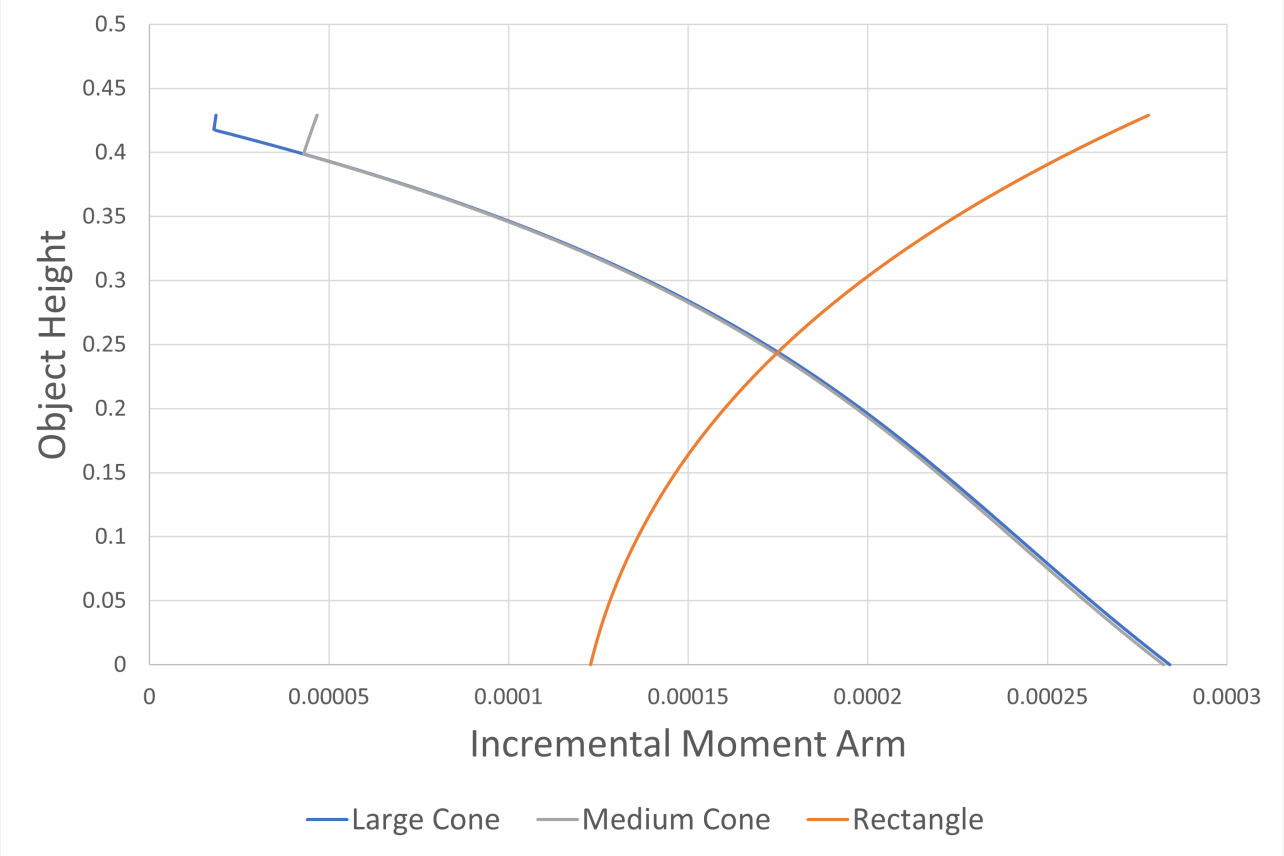

Figure 42: Incremental Moment Over Different Objects

In this image, we can see three incremental profiles generated all based on the same expected wave. With the following object properties:

-	Diameter (m)	H (m)	Surface Area (m$\hat{2}$)	E (Mpa)	I (m)	Avg Cauchy
Medium Cone	0.0137	0.43	0.0029455	5	9.07705E-05	13.99
Large Cone	0.0346	0.43	0.007439	5	2.29E-04	13.99
Rectangular Prism	0.0173	0.43	0.007439	14.59	9.07705E-05	13.99

The first and more noticeable area comes in the object which has a completely different shape from that of the other two objects (rectangle). In this case, the E-moduli must be increased to generate the same EI. When comparing it to the Large cone profile the lines are inverted with the local moment of bending increasing with object height for the rectangle and decreasing for the cone. For the profiles of object deflection to match the profile of the moment arm must also match that of the original object. In this, we find a disparity when changing the object shape requiring a variable E modulus over the height to generate the same profile. The Medium and Large cones however show that their profiles (using the moment arm) have the same force/resistance ratio. Theoretically, this would generate the same amount of deflection. As seen previously in figure27 this is not the case. The top of the equation $\rho\delta_y U_{ref}^2 l^3$ predicts the force of fluid on the front face of the object well. When looking at the denominator. The second area moment I which views the object as a triangle does not take into account the mass moment of inertia of an object. These are three-dimensional objects, while I only takes into account the projected 2D area of the object. Both objects are made of the same theoretical material and therefore have the same density which will be used to compare the mass moments of inertia I_m. For a cone

$$I = \frac{bh^3}{12} \tag{44}$$

while

$$I_m = m(\frac{3r^2}{20} + \frac{h^2}{10}) \tag{45}$$

since the density of both objects is made of the same material, m can be simplified in this case to the volume of a cone $V_c = \frac{\pi r^2 h}{3}$ if we replace the mass portion of the equation m with volume we get the following equation which we can denote as I_v of the volume moment

$$I_v = \frac{\pi r^2 h}{3}(\frac{3r^2}{20} + \frac{h^2}{10}) \tag{46}$$

generally I_m has the units of $[ML^2]$ in this case when comparing similar densities can be changed to $[L^3 * L^2] or [L^5]$ and I units of $[L^4]$. Since we are comparing objects of the same density the mass component of I_m can be ignored and replaced with volume. If I_v is plugged into Cauchy in replacement of I which again only works, in this case. The following curves are now generated when viewing the object incrementally.

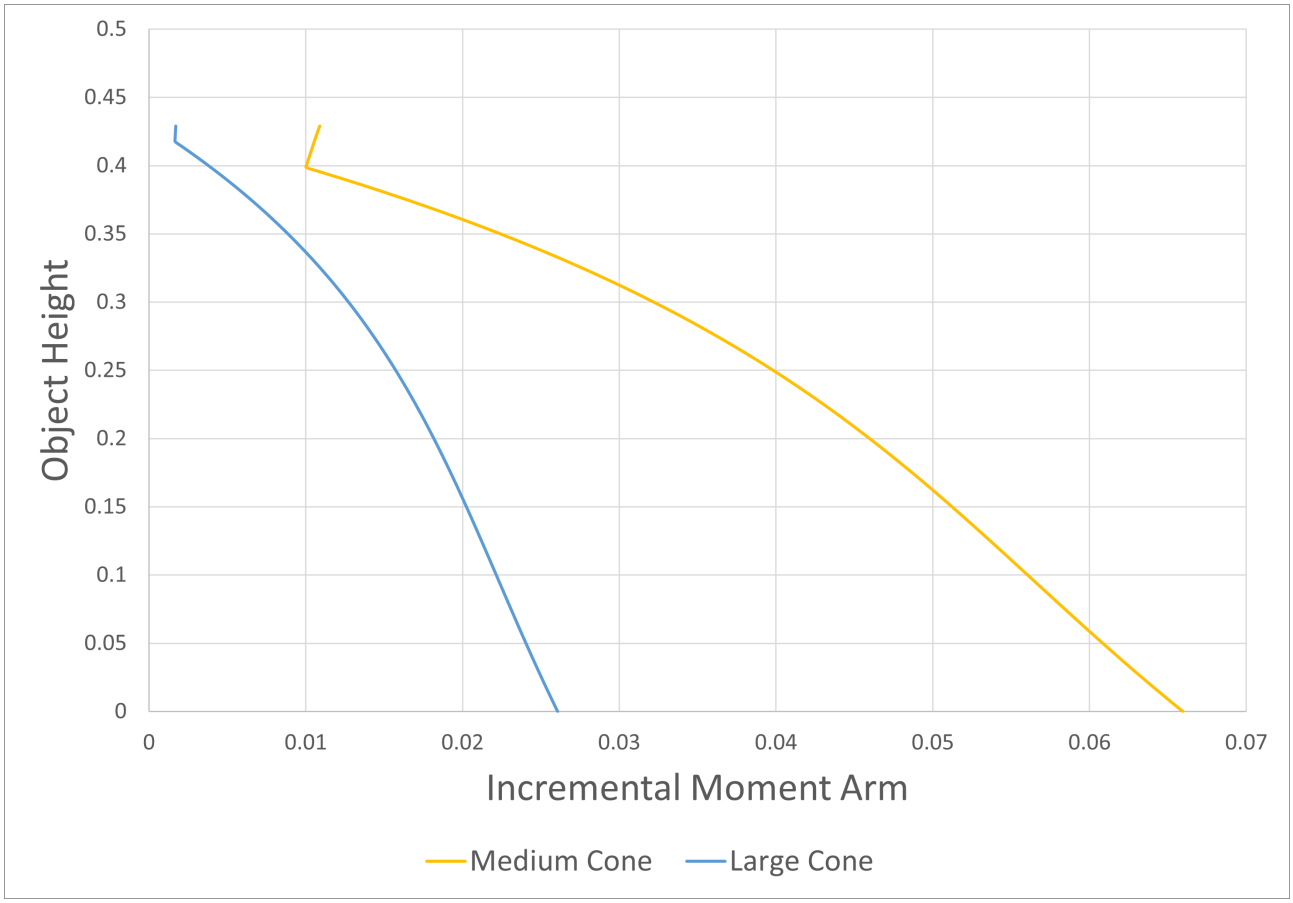

Figure 43: Incremental Moment Over Similar Cones Using Mass Moment

The reason for this separation is the ratios of $I[L^4]$ Vs $I_v[L^2 * L^3]$ in the original Cauchy equation, the large cone has an EI of 1324.9 and the medium cone of 453.8 which gives a ratio of roughly 2.9 between the large and medium cone. However, when looking at object inertia in the form of the volume moment the values for the large and medium are now 12.49 and 1.95 respectively which provides a ratio of 6.39 between the two. This is shown in the ratio between the actual deflection of the objects where the medium bends between 3-7 times more than the Large cone for the 0.68 WL.

Test	Large 5Mpa θ	Med 5Mpa θ	Ratio M/L
1	0.648828	4.817604	7.425084
2	2.738196	15.22681	5.560889
3	-	18.93105	-
4	3.236776	13.5301	4.180117
5	5.765098	20.72033	3.594098
6	10.32008	-	-
7	2.862235	12.3765	4.324068
8	6.247896	24.03867	3.847482
9	11.82618	42.79343	3.618535
10	0.983501	6.133971	6.236874

This change in ratio is what causes a disparity when viewing cones with the Cauchy equation across different

object scales, as it is only noticeable when looking at the object in 3 dimensions that do not have constant cross-sections. When looking then at the deflection of the object relative to the Cauchy number across different object types we see the expected result, where the larger object due to its mass moment deflects significantly less.

7.1.2 CAL/KC

In comparison to the current numbers of KC, Ca, the combined CaL/KC as created by [**Jacobsen et al. 2019**] works the best out of the numbers, Ca, KC, CaL, and CaL/KC for describing the motion of a mimic stem across different flow conditions. These stems, however, are cylindrical and maintain a constant cross-section, as well as being fully submerged underflow. In theory, this number serves to cancel out the issues created with the singular ratios of KC or Ca. While this value holds up well for stems it fails to capture the complexity of the situation undergoing the mimics in this testing series. In fig.44 we can see the power and linear relationships for deflection Vs CaL/KC plotted on a log-log scale and the correlation across different tests and objects we get the following figure which has essentially a correlation of 0 across multiple points.

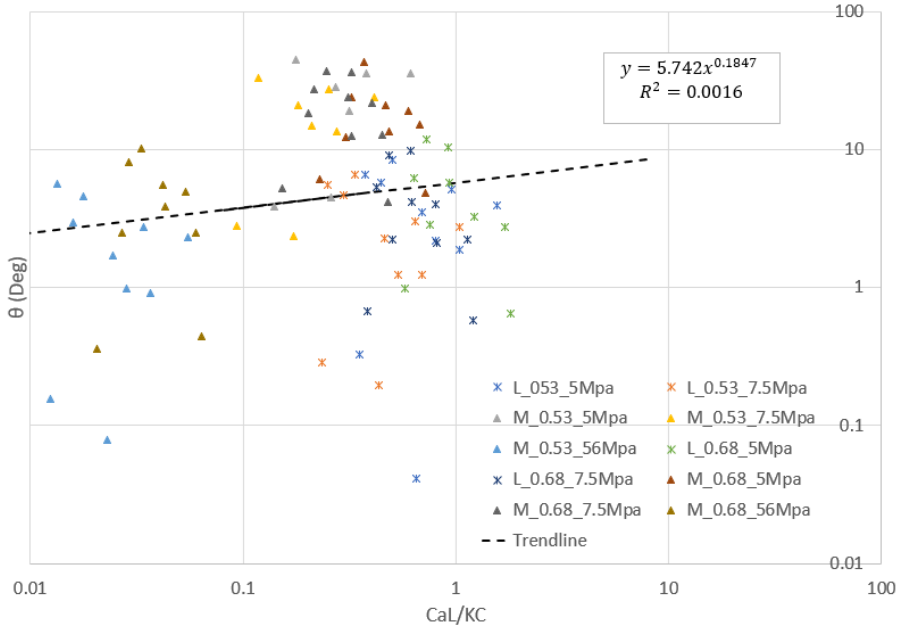

Figure 44: Deflection Vs CaL/KC

This is in theory due to as previously mentioned in the section on Cauchy, the 3-dimensional flow effects that occur as objects change in size. As size changes the relative scale of the flow ie) wave attenuated force takes on a different ratio which in turn causes these number to lose their validity. The KC and Ca are both dimensionless numbers that relate to specific circumstances, thus when the scale of an object no longer matches the scale of the wave flow, three-dimensional effects begin to occur which is outside the scope of a 2-D equation.

8 Conclusion(s)

The goals of this research and thesis were to attempt to gain a better understanding of the effects governing the deflection of schematized willow branches under wave flow, and how this deflection can, in turn, affect the ability of an object to reduce wave energy. The canopy (mimic) models were developed based on the projected frontal area of a pollard willow as defined by [**Kalloe et al. 2023**]. These mimics were then tested across a range of waves and water levels to determine the impacts of object motion or deflection on forcing, and in turn the ability to dampen wave energy. Deflection θ which was defined as the position of the tip from rest to the maximum forward motion of the object. Which can also be defined as the deflection at the moment the bulk of the object reaches a net-0 velocity. This was done to remove the secondary mode of bending from the data set. This θ was then compared across multiple different variables (H, η,T_p,F_p) and ratios (KC, Ca).

As a result of the research done here, it was determined that there is a direct link between the amount of force an object can exert on the wave flow and the amount of deflection in regard to the peak forward motion of an object. While already well-known phenomena, when the data was compared to the current methods. It was found that the current ratios used to predict object motion can sometimes fail to capture the complexities of flow due to the limitations from which they were derived. The Cauchy and KC numbers work as excellent predictors of a singular object across a range of wave conditions. However, fails to relate to changes in object dimensions. Similarly, the $\frac{CaL}{KC}$ while an excellent predictor of cylindrical stems under submerged wave flow, again fails to capture the θ of the object under partially submerged flow, for cones across different scales. This was determined to be due to the 3-Dimensional effects of flow.

Based on the data recorded across the tests conducted in this research a reasonable relationship for object deflection in turbulent flows was determined, where the Reynolds# is above 1000 for the bulk of the object. Generating the following equation.

$$\theta = 1224 * (\frac{F_P \eta S^3}{EI})^{1.19}$$

Which has an R^2 of 0.742 fit to the data. Where θ is the maximum forward tip deflection in degrees, F_p is the peak force, and η is the peak impact height of the wave on the object. S is the object slope from base to tip. E is the Young's Modulus, and I is the moment of inertia. It is also important when looking at this equation to understand what each part represents, for different shapes the final number may very well be different as mentioned in the analysis section.

This coupled with a hard threshold for deflection of 2 degrees, can be used to determine if the incident wave on a partially submerged object will result in an amount of deflection that is significant enough to quantify the object as flexible under the current flow conditions. With a soft threshold of object stiffness located at 5 degrees of deflection. The limitation of this equation lies in the prediction of larger amounts of deflection. Predicting

the peak forces of a highly mobile object requires a complex analysis or a physical model. However, currently, it can still be used as a method to determine if an object can be considered stiff or flexible in relation to the influence of flexibility on the force compared to a stiff branch. Once an adequate equation for calculating the drag coefficient can be found. Most importantly this work shows that for complex shapes, to properly generate a method of determining motion. The changing cross-sectional areas must be taken into account in the equation in this case the tapering of the mimic was included through the slope term.

8.1 Recommendations

The conclusions in the paper are promising on the impact of tapered shapes on the deflection of vegetation. However, this data is only for cones, more testing needs to be conducted. More complex non-constant cross-sectional shapes need to be tested like forked or branching mimics. These then need to be compared to the motion of objects that are within the influence of other objects. Different water levels (fully submerged, fully emerged, etc..) need to be tested. More complex wave patterns specifically with irregular waves which are not included in this test data need to be observed. All of this should eventually be combined to help develop a CFD to simulate the mechanical properties of these types of shapes in any range of conditions.

The peak forces are another area of concern not in the variation but in the actual values. The predicted forces can be approximated for a stiff object without much difficulty, once a drag coefficient is determined. However, once the object goes through high amounts of deformation it becomes significantly more complex to predict the forces. As well the equation derived in this paper may prove to be accurate, it is also a first derivation and can most certainly be improved upon by further research to study the bending of objects with a non-constant cross-sectional area.

9 References

Kalloe, S. A., Hofland, B., Antolínez, J. A. A., & van Wesenbeeck, B. (2022). Quantifying Frontal-Surface Area of Woody Vegetation: A Crucial Parameter for Wave Attenuation. *Frontiers in Marine Science, 9,*[820846]. https://doi.org/10.3389/fmars.2022.820846

Jadhav, R. S., Chen, Q., & Smith, J. M. (2013). Spectral distribution of wave energy dissipation by salt marsh vegetation. *Coastal Engineering, 77*, 99-107.

Soloff, S. M., Adrian, R. J., & Liu, Z. C. (1997). Distortion compensation for generalized stereoscopic particle image velocimetry. *Measurement science and technology*, 8(12), 1441.

Stancic, I., Grujic Supuk, T., & Panjkota, A. (2013). Design, development and evaluation of optical motion-tracking system based on active white light markers. *IET Science, Measurement & Technology*, 7(4), 206-214.

Mendez, F. J., & Losada, I. J. (2004). An empirical model to estimate the propagation of random breaking and nonbreaking waves over vegetation fields. *Coastal Engineering*, 51(2), 103-118.

Wiegel, R. L. (1960). A presentation of cnoidal wave theory for practical application. *Journal of Fluid Mechanics*, 7(2), 273-286.

Dalrymple, R. A., Kirby, J. T., & Hwang, P. A. (1984). Wave diffraction due to areas of energy dissipation. *Journal of waterway, port, coastal, and ocean engineering*, 110(1), 67-79.

Dijkstra, J. T., & Uittenbogaard, R. E. (2010). Modeling the interaction between flow and highly flexible aquatic vegetation. *Water Resources Research*, 46(12).

Jacobsen, N. G., Bakker, W., Uijttewaal, W. S., & Uittenbogaard, R. (2019). Experimental investigation of the wave-induced motion of and force distribution along a flexible stem. *Journal of Fluid Mechanics*, 880, 1036-1069.

Kelty, K., Tomiczek, T., Cox, D. T., Lomonaco, P., & Mitchell, W. (2022). Prototype-scale physical model of wave attenuation through a mangrove forest of moderate cross-shore thickness: LiDAR-based characterization and Reynolds scaling for engineering with nature. *Frontiers in Marine Science*, 8, 780946.

Marjoribanks, T. I., Hardy, R. J., Lane, S. N., & Parsons, D. R. (2014). High-resolution numerical modelling of flow—vegetation interactions. *Journal of Hydraulic Research*, 52(6), 775-793.

Nam, P. T., Staneva, J., Thao, N. T., & Larson, M. (2020). Improved calculation of nonlinear near-bed wave orbital velocity in shallow water: Validation against laboratory and field data. *Journal of Marine Science and Engineering*, 8(2), 81.

Takagi, H., Mikami, T., Fujii, D., Esteban, M., & Kurobe, S. (2016). Mangrove forest against dyke-break-induced tsunami on rapidly subsiding coasts. *Natural Hazards and Earth System Sciences*, 16(7), 1629-1638.

Van Rooijen, A., Lowe, R., Ghisalberti, M., Conde-Frias, M., & Tan, L. (2018). Predicting current-induced drag in emergent and submerged aquatic vegetation canopies. *Frontiers in Marine Science*, 5, 449.

Fredsoe, J., & Sumer, B. M. (2006). Hydrodynamics around cylindrical structures (revised edition) (Vol. 26). *World Scientific*.

Laitone, E. V. (1960). The second approximation to cnoidal and solitary waves. *Journal of fluid mechanics*, 9(3), 430-444.

Dekkers, J. (2018). Undular bore development over coral reefs: An experimental study.

Strusińska-Correia, A., Husrin, S., & Oumeraci, H. (2013). Tsunami damping by mangrove forest: a laboratory study using parameterized trees. *Natural Hazards and Earth System Sciences*, 13(2), 483-503.

van Wesenbeeck, B. K., Wolters, G., Antolínez, J. A., Kalloe, S. A., Hofland, B., de Boer, W. P., ... & Bouma, T. J. (2022). Wave attenuation through forests under extreme conditions. *Scientific reports*, 12(1), 1884.

Korteweg, D. J., & De Vries, G. (1895). XLI. On the change of form of long waves advancing in a rectangular canal, and on a new type of long stationary waves. *The London, Edinburgh, and Dublin Philosophical Magazine and Journal of Science*, 39(240), 422-443.

Schiereck, G. J. (2017). Introduction to bed, bank and shore protection. *CRC Press*.

Buck, J. R., Daniel, M. M., & Singer, A. C. (1997). Computer explorations in signals and systems using MATLAB. *Prentice-Hall, Inc.*.

Stoica, P., & Moses, R. L. (2005). *Spectral analysis of signals* (Vol. 452, pp. 25-26). Upper Saddle River, NJ: Pearson Prentice Hall.

Goring, D. G. (1978). Tsunamis–the propagation of long waves onto a shelf. *California Institute of Technology*.

Morison, J. R., Johnson, J. W., & Schaaf, S. A. (1950). The force exerted by surface waves on piles. *Journal of Petroleum Technology*, 2(05), 149-154.

El-Reedy, M. A. (2019). Offshore structures: design, construction and maintenance: Chapter 7 - Assessment of Existing Structures and Repairs. *Gulf Professional Publishing*.

Keulegan, G. H., & Carpenter, L. H. (1956). Forces on cylinders and plates in an oscillating fluid. *National Bureau of Standards*.

Reynolds, O. (1883). III. An experimental investigation of the circumstances which determine whether the motion of water shall be direct or sinuous, and of the law of resistance in parallel channels. *Proceedings of the royal society of London*, 35(224-226), 84-99.

Jadhav, R. S., Chen, Q., & Smith, J. M. (2013). Spectral distribution of wave energy dissipation by salt marsh vegetation. *Coastal Engineering*, 77, 99-107.

Chen, H., Ni, Y., Li, Y., Liu, F., Ou, S., Su, M., ... & Suzuki, T. (2018). Deriving vegetation drag coefficients in combined wave-current flows by calibration and direct measurement methods. *Advances in water resources*, 122, 217-227.

Bradley, K., & Houser, C. (2009). Relative velocity of seagrass blades: Implications for wave attenuation in low-energy environments. *Journal of Geophysical Research: Earth Surface*, 114(F1).

Suzuki, T., Zijlema, M., Burger, B., Meijer, M. C., & Narayan, S. (2012). Wave dissipation by vegetation with layer schematization in SWAN. *Coastal Engineering*, 59(1), 64-71.

Ursell, F. (1952). Edge waves on a sloping beach. *Proceedings of the royal society of London. Series A. Mathematical and Physical Sciences*, 214(1116), 79-97.

Airy, G. B. (1845). *Tides and waves*. B. Fellowes.

Stokes, G. G. (1847). On the theory of oscillatory waves. *Trans. Cam. Philos. Soc.*, 8, 441-455.

Hughes, S. A. (1993). *Physical models and laboratory techniques in coastal engineering* (Vol. 7). World Scientific.

10 Appendix A

10.1 Lens Distortion & Magnification Factors

To find any lens distortion images with a reference (checkerboard) were put through the Matlab processing and the distances of high contrast (Square Edges) were used to generate the relative distortion. There was no change in the amount of pixels to cover the 20mm squares regardless of location in the frame. While the object is submerged at all points in the x-y direction the size of a 20 mm square is 36 pixels, corresponding to a pixel size of 0.555 mm per pixel. From top to bottom and then from left to right. This implies that the error due to rounding must be <0.5 pixels hence the error is <0.5 across a distance of roughly 50 pixels which implies a maximum error of <1% at the maximum distortion, generating a maximum error per pixel of <0.00555 mm for the dry case.

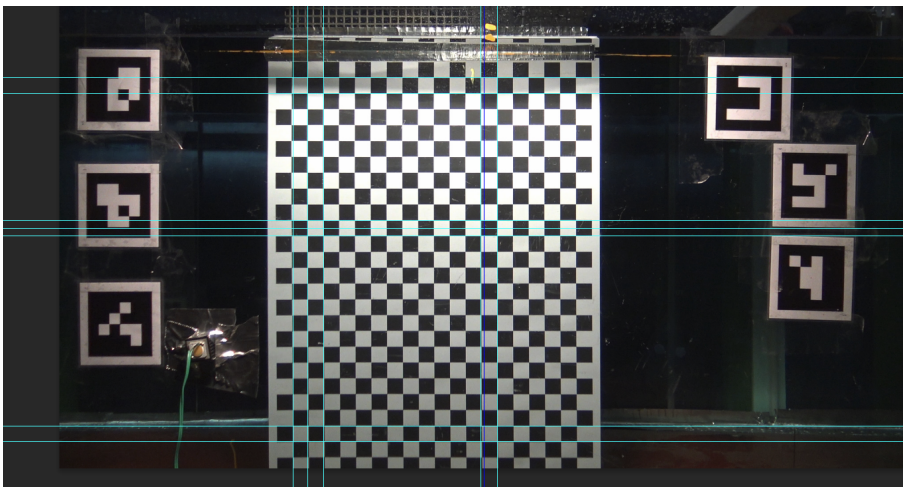

Figure 45: Image Distortion Check

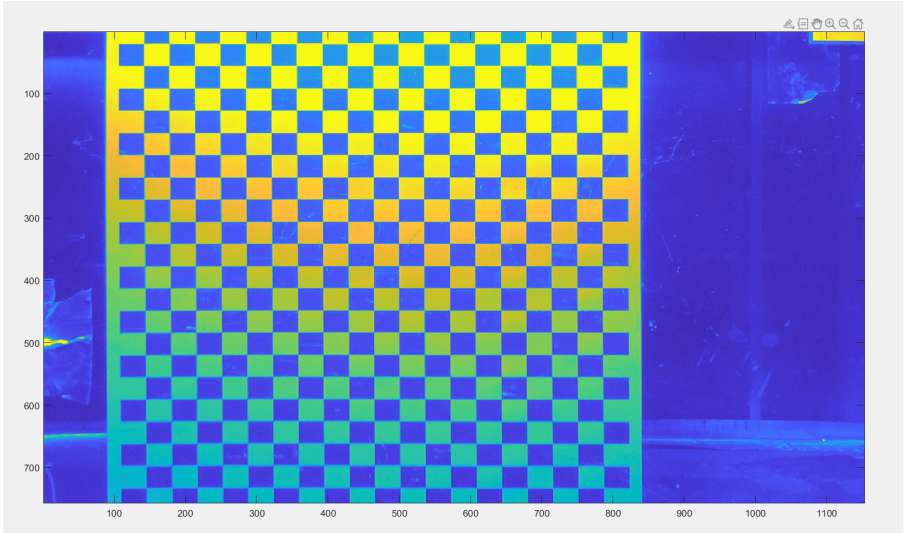

Figure 46: Viewing range

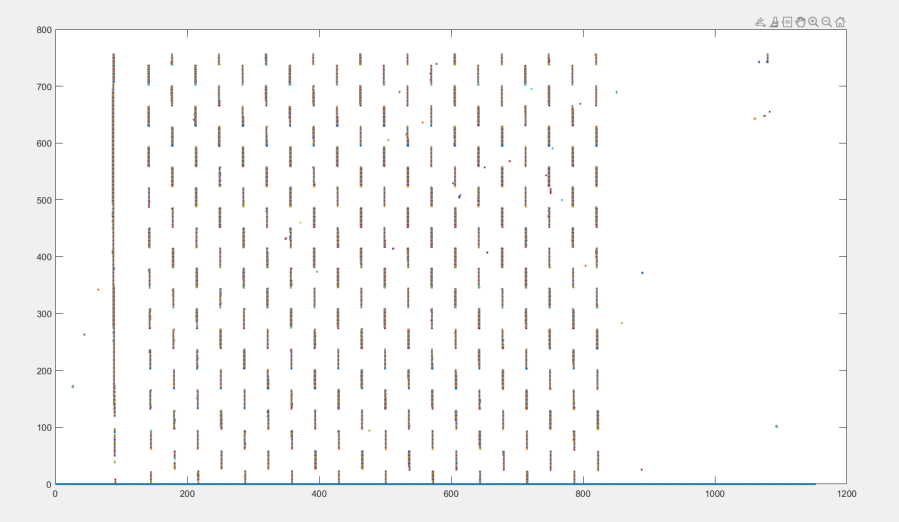

Figure 47: Image Distortion Check Matlab

The same procedure was repeated to determine the magnification factor of the fluid. The dry checkerboard shows that 20mm, or one square is covered by a distance of 32 pixels i.e. 1 pixel is equivalent to 0.625 mm. This means converting the captured pixels to dry from submerged is a factor of 9/8. In the dry case again, at maximum distortion, there is a difference of <0.5 pixels leading to a maximum error of <1% or <0.00625 mm for the submerged case. [**Stancic 2013**] a study on human movements for sports medicine details an acceptable amount of distortion for active motion as 1.1mm for velocities of 2.5m/s being well within the acceptable value. Across the entire length of the active objects used in this testing which is 0.43 meters, there is no change in the perceivable error between sections thus the distortion must be below 0.5 pixels. Accounting for a factor of safety the distortion maximum is 0.625mm from base to tip. Tip arc deflection can be viewed with the formula a

$$\frac{2\pi r * Deg}{360} = Displacement \tag{47}$$

in this case would be

$$\frac{2 * 430 * \pi * Deg}{360} = 0.625mm \tag{48}$$

meaning the maximum effect from the maximum possible distortion would be extremely small, the exact ratio is confidently within a range of $+-0.008$deg from the observed values.

The above discusses the distortion error for 1080p, some videos are also recorded in 4k resolution, the same measurements were taken for those camera settings and unsurprisingly in the dry conditions, 20mm is equivalent to 64 pixels in the x and y directions or 0.3125 mm/pixel. Double that of the 1080p, for the submerged conditions the same is again found with a 9/8ths multiplier leaving the pixel count for 20mm at 72 pixels in x and y directions or 0.278 mm/pixel. In this dimension based on the ruler size of 64 pixels with no measurable distortion inside the active range of the video, the detectable distortion must fall at again <0.5 pixels of

distortion across 64 pixels. This leads to roughly the same radial distortion of +- 0.008 deg of an arc.

10.2 High and Low Contrast Images

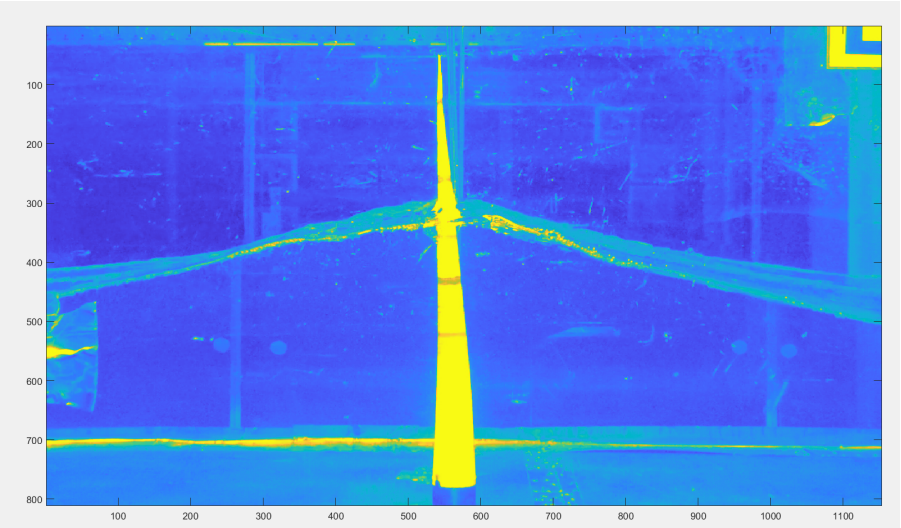

Figure 48: High surrounding Contrast

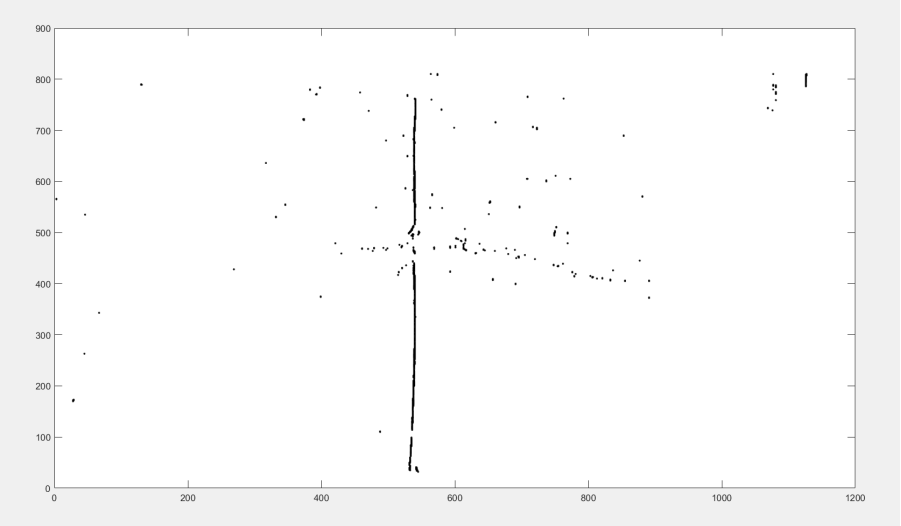

Figure 49: High surrounding Contrast Scatter

In the images with good lighting, there is a high contrast between the cone and its surroundings. In the above situation, the tip of the object is easy to find and then extract using code, as seen by fig.49

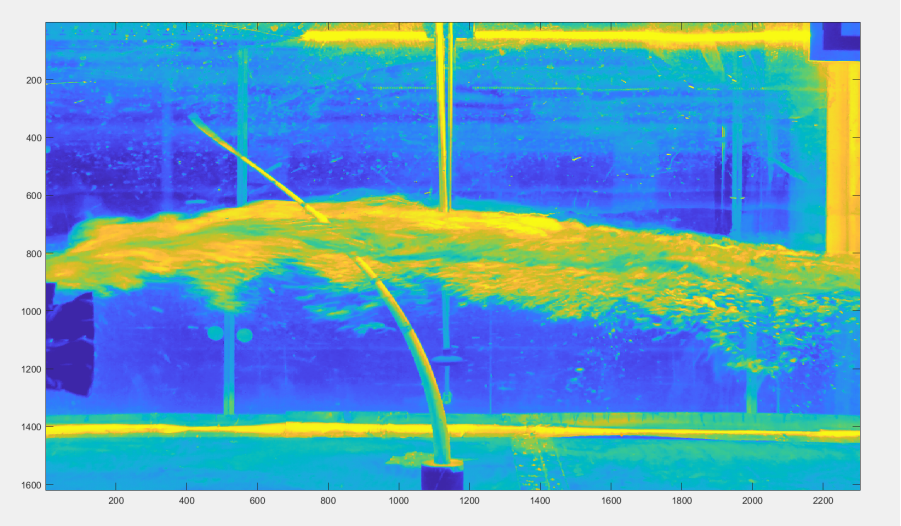

Figure 50: Low surrounding Contrast

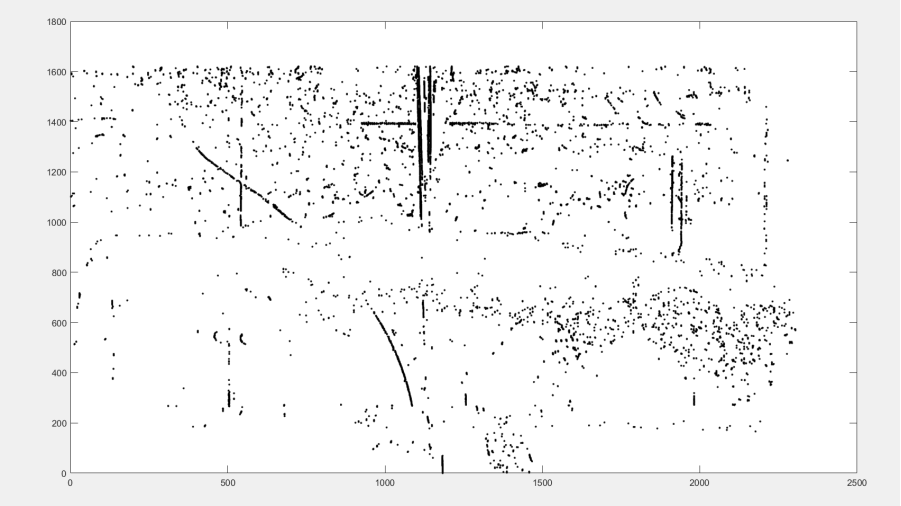

Figure 51: Low Surrounding Contrast Scatter

In the low lighting/contrast setting the cone is harder to distinguish from its surroundings. While adjusting the filter can end up with a reasonable resolution of the object, too many other points are pulled into the frame along with it. This results in the point needing to be taken by hand from the original image. Creating the +-1 pixel error for any points taken this way.

10.3 Object Tracking

First, the image is loaded up into Matlab, then it is converted into grayscale, and the top 30 percent of the image is removed due to high contrast at the top. As well as the left and right 20 percent to remove the contrast from the Arucos. Each row of the picture is then run through the difference function and a filter to remove low contrast points. All passing points are then converted to 1s and multiplied by the inverse of their row number. Then plotted as points on a loop to generate a new version of the image graphically which can then be matched

to the original as a way of tracking the object's motion and validating it.

10.3.1 Code

```
I = imread("C:\Users\eliwe\OneDrive\Documents\Thesis_stuff_2022\Frame_Analysis\0.68\7.5Mpa Med\6\2.jpg");
I2 = im2gray(I);
s2 = size(I2);
II = I2((s2(1)*0.25):s2(1), s2(2)*.2:s2(2)*0.8);
III = I((s2(1)*0.25):s2(1), s2(2)*.2:s2(2)*0.8);
%II = I2;
s = size(II);
n = 1;
g = 1;
k = [1:1:s(1)];
figure
image(II)
%figure(2)
%imshow(III)
if n <= s(1)
    while n<=s(1)
    m(n,:) = diff(II(n,:));
    n = n+1;
    end
end
x = zeros(s(1),s(2)-1);
c = size(x);
f = c(1)*c(2);
for k=[1:1:f]
    if m(k)< 60
        x(k) = nan;
    else
        x(k) = 1;
    end
end
for k = [1:1:s(1)]
    x(k,:) = x(k,:)*((s(1)-k));
end
figure(3)
for l = [1:1:s(1)]
    plot(x(l,:),'.','color','red')
    hold on
end
```

Figure 52: Image Processing Code

10.4 Camera Specifications

Camera: Sony 4K FDR-AX33 20.6 MegaPixels Handycam;

25fps, image size 16:9 (2.1M);

File Format XAVC S HD ;

note: This was adjusted in the later tests with the smaller objects to a frame rate of 50 fps, a shutter speed of 600 Hz, and an image of 1980 x 1080 pixels to account for the increased frame rate.

10.4.1 Camera Setup / Calibration

1) Clean the flume walls so as to provide a clear picture

2) Calibrate the lens to remove distortion

4) Calibrate the Camera in space using arucos

3) Set up the checkerboard in the plane with the tree in both dry and submerged conditions.

11 Appendix B: CSV Analysis

11.1 Data Correlation

Cross-correlation measures the similarity between a vector x and shifted (lagged) copies of a vector y as a function of the lag. If x and y have different lengths, the function appends zeros to the end of the shorter vector so it has the same length as the other. Using this data the maximum value is found in the r-vector output. Then using the "find" function, which finds the location of the max within the r-vector we get the number of places the matrix was shifted to line them up. This placement then is subtracted from half the size of the r vector which gives the required shift of the secondary matrix relative to the original. Depending on the sign will determine if the matrix needs to be shifted forward or backward. If the shift value is positive then the secondary matrix simply has that amount of points removed from the beginning excluding the first column which includes time. If the value is negative a matrix of 0s is appended to the front of the secondary matrix with a length equal to that of the shift. This then pushes the data in line with the mount data. All of this is done using the first deep water wave gauge (WG1) which deals with the lowest amount of noise and therefore provides the most accurate matching.

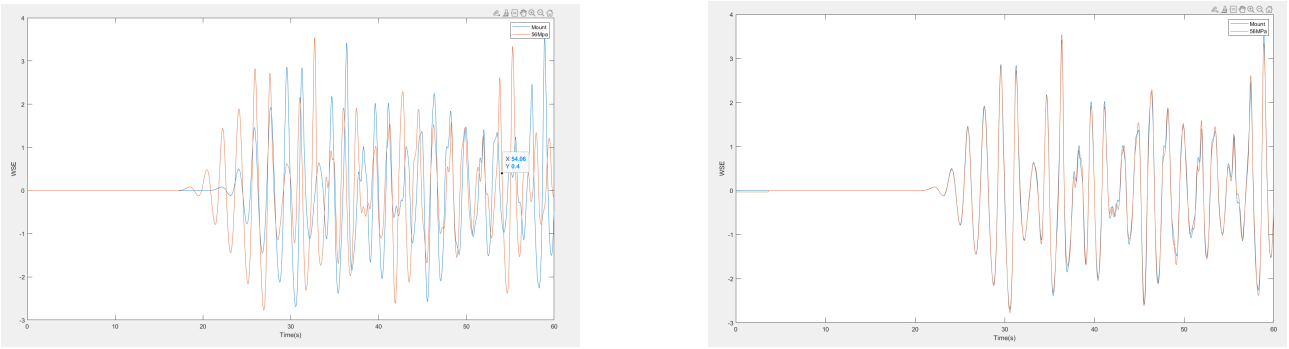

(a) Uncorrelated Data

(b) Correlated Data

Figure 53: Ex Data Correlation

After this process is completed, the force values may also be added or subtracted from the canopy. The secondary matrix is trimmed so that it is the same size as that of the mounting matrix. This is to ensure that when applying either data set to one another only the data that belongs to the same waves is used. To give an example, if data taken after a test on the mount was completed in a 1 min test whereas the canopy+mount test was 1.5 min due to not shutting the recording down. The function will trim the time back to a 1 min test synced with the mount.

11.1.1 code

```
%correlates the data to the mount and removes the force recieved
%by the mount leaving just the canopy forcing
test1 = importdata('D:\Sorted Data\0.68\6-Cone Mount\5.csv');
test2 = importdata('D:\Sorted Data\0.68\6cone 7.5Mpa\5.csv');
Mount = test1;
b = length(test2);
A3 = test2(12000:b,2:16);
A4 = test2(1:(b-12000+1),1);
A2 = [A4 A3];
x = Mount(1:12000,2);
y = A2(1:12000,2);
r = xcorr(x,y);
z = max(r);
shift =12000 - find(z == r);
if shift>=0
    A2_move = A2(shift:length(A2),2:16);
    A2_new = [test2(1:(length(A2)-shift+1),1) A2_move];
else
    n = zeros(abs(shift),15);
    A2_move = [n;A2(:,2:16)];
    A2new = [test2(
end
Mlength = length(Mount(:,1));
Nlength = length(A2new(:,1));
if Mlength > Nlength
    Fnew = A2new(:,16)-Mount(1:Nlength,16);
    App = zeros((Mlength-Nlength),16);
    Fmove = [Fnew;App(:,1)];
    Adjusted = [A2new;App];
    FAdjusted = [Adjusted Fmove];
else
    Fnew = A2new(1:Mlength,16)-Mount(:,16);
    Adjusted = A2new(1:Mlength,:);
    Fmove = Fnew(1:Mlength,:);
    FAdjusted = [Adjusted Fmove];
end
%csvwrite('D:\Sorted Data\0.68\6cone 7.5Mpa\A5.csv',FAdjusted)
```

Figure 54: Data Correlation Code

11.2 Force Peak Separation

The peaks are separated with the 'FindPeaks' function in Matlab. With the constraints that peaks must be at least 1/2 of the maximum recorded value as well as 150 ticks apart (0.75 seconds), this generates the as seen below the plot. All highlighted points are recorded and placed into a matrix along with the average of the 3rd through 13th points. Data is taken at the third point to guarantee the wave is fully spun up and stopped at the 13th to ensure no reflections are taken into account.

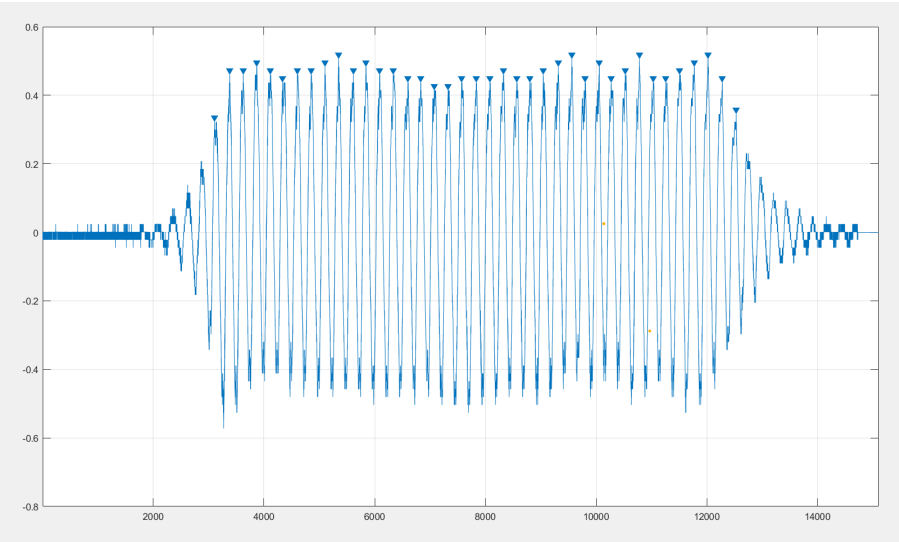

Figure 55: Peaks

In 2 tests [Stiff Medium 3-0.53, 5Mpa Medium 9-0.53], however, there was a massive spike generated by the force gauge that left reality before the waves even started generating. In this case, the data is segmented to the point where the spike peak is outside of the window being looked at. Then the same method as previously mentioned is applied to the data.

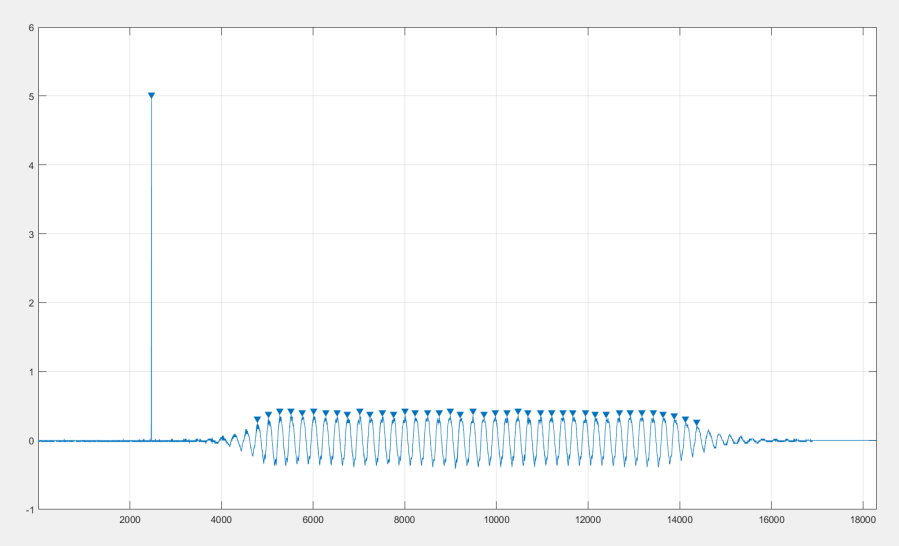

Figure 56: Peaks Outliers

11.2.1 code

```
function final = localmaxima(test1)
Mount = test1;
force = max(Mount);
[peaks,locs] = findpeaks(Mount,'MinPeakHeight',force/2,'MinPeakDistance', 150);
avg_peaks = mean(peaks(3:13));
appendVector = [avg_peaks;zeros(length(peaks)-1,1)];
final = [locs peaks appendVector];
end
```

Figure 57: Peaks Calculation

11.3 Line-up Error

The above process of force correlation is done by lining up the data at a frequency perfect match 1/200 Hz. However, in rare cases, the data may require a shift of 1/400 Hz. In this case, it is rounded to the nearest whole 1/200 Hz and then shifted. The error that this generates is negligible on the total and peak forces. Using the 5Mpa A9 at the 0.53WL tests as an example. This data set has particularly complex peaks due to the fully turbulent nature of the wave as it is broken on impact and incident on a highly flexible object. Will be heavily affected by offsets. As an example the data was shifted down 1/200th Hz creating a small offset then the peaks were taken from the data and averaged resulting in an average peak force of 0.3787 N relative to the properly shifted data which generated a peak force average of 0.37373 this is an error of the average of roughly 1.33 percent. This shift is also twice the actual effect that could occur in a viable data set itself. This while important

to keep in mind will have a minimal impact on the trends being looked at as the scale of difference is in the 10s of percent between data sets.

11.4 Cnoidal Wave Orbital Approx

Since depth-averaged velocity can be defined as

$$U = \frac{Q}{d + \eta_w} \tag{49}$$

, where Q is the discharge per unit width of the flume and

$$Q = c * \eta_w \tag{50}$$

and U is the depth-averaged velocity. Then

$$U = \frac{c\eta_w}{h + \eta_w} \tag{51}$$

as the net flux in the system can be assumed to be 0 since the experiments take place in a flume. The following derivation can then be used.

$$U_l = \frac{Q_l}{h + \eta_w l} \tag{52}$$

Where U_l is the average linear velocity, Q_l is the theoretical linear wave theory flow and $\eta_w l$ the linear WSE. When applied to the wave peaks the equation then takes on the form:

$$U_{lp} = \frac{Q_{lp}}{h + H/2} \tag{53}$$

The symbol $_lp$ denotes the linear theory values at the wave peak. where

$$Q = c * H/2 \tag{54}$$

thus

$$U_{lp} = \frac{c * H/2}{h + H/2} \tag{55}$$

however c can be replaced with

$$c = \sqrt{g(h + H/2)} \tag{56}$$

leaving

$$U_{lp} = \frac{\sqrt{g * (h + H/2)} * H/2}{h + H/2} \tag{57}$$

to then find the Cnoidal velocity the WSE recorded at the wave peak is then used. Which can then be presented as

$$U_{cn} = \frac{\sqrt{(g * (h + \eta_{w-cn})} * \eta_{w-cn}}{h + \eta_{w-cn}} \tag{58}$$

meaning that.

$$\frac{U_{cn}}{U_{lp}} \propto \frac{\eta_{w-cn}}{H/2} \tag{59}$$

Using this ratio for the depth-averaged flow velocity, it can then simply be applied to the orbital velocities generated across the profile by linear wave theory ie)

$$U_{max} = \omega a * \frac{cosh(k(h+z))}{sinh(kh)} \tag{60}$$

which then generates a rough estimate for the peak orbital velocities of a Cnoidal wave by

$$U_{ref} = U_{max} * \frac{\eta_{w-cn}}{H/2 + h} \tag{61}$$

in theory this can be applied throughout the entire wave as well. However, in points where the WSE is out of phase ie) not the wave peak or trough, it becomes far more complicated.

11.5 Positive Force

While peak forces are useful for identifying the effects the flexibility exerts on the object it is important to also see how much energy is taken out of a single wave peak. To do this the average positive force for a singular wave was taken from the data set using a simple code to find the total positive area during the wave per peak. Found simply by using the locations of the peaks found in the Peaks function, then removing all negative points from the data and summing the total positive points. Followed by multiplying by the sampling frequency and dividing by the number of peaks viewed. This acts as a left Riemann sum for the data.

11.5.1 Code

```
function [F] = AreaUnderCurve(Forces,Peaks)
p1 = Peaks(5,1);
p2 = Peaks(8,1);
A = Forces(p1:p2);
z = length(A);
for k = 1:z;
    if A(k)<=0
        C(k) = 0;
    else
        C(k) = A(k);
    end
end
F = sum(C)*1/(z/2);
end
```

Figure 58: Average Force (N/S) Code

12 Appendix C: Processed Data

12.1 Force Data

Table 7: % Difference In Peak Force From the Stiff Object

0.68							
Test#	5Mpa Large	7.5Mpa Large	56Mpa Large	5Mpa Med	7.5Mpa Med	56Mpa Med	7.5Mpa 6cone
1	-1.650	-1.650	-1.404	5.681	3.125	3.125	2.835
2	-3.872	-0.456	-6.292	-48.743	-44.563	-16.711	-25.213
3	-5.628	5.824	-0.494	-32.091	-26.796	-21.506	-37.433
4	0.375	11.891	-5.660	-18.444	-16.557	-21.276	-17.418
5	8.577	23.297	0.226	-26.058	-22.756	-15.482	-36.106
6	2.369	15.287	2.694	-46.090	-33.960	-14.959	-46.610
7	5.878	17.155	-6.801	-14.430	-8.717	-13.561	-22.045
8	2.037	15.585	-5.269	-20.124	-19.092	-21.156	-32.625
9	-0.203	4.604	-0.749	-40.693	-34.356	-11.006	-45.099
10	-1.901	2.565	-5.141	-5.430	-2.716	2.714	-10.909
	0.53						
1	-4.516	-9.393	-8.497	-25.033	-3.847	-11.790	-67.367
2	-5.295	-10.205	-6.558	-13.471	-24.580	1.852	-1427.578
3	-28.138	-20.951	-4.244	-43.058	-54.016	-17.687	205.408
4	3.762	-5.056	7.201	-25.075	-35.897	-3.732	861.745
5	8.103	10.538	3.836	-30.567	-34.597	-2.795	1137.642
6	-29.589	-33.502	-26.216	-65.168	-63.557	-34.870	82.271
7	4.023	8.476	-6.884	-23.748	-27.683	-2.953	837.463
8	-36.097	-29.891	-23.821	-65.801	-69.202	-42.119	64.300
9	-41.955	-37.988	-25.753	-61.903	-63.724	-32.784	94.375
10	-1.447	-6.388	-4.576	-7.955	-15.905	-3.975	300.096

12.2 Frame Locations

Initial frame	0.68					
Test#	5Mpa Large	7.5Mpa Large	56Mpa Large	Stiff Large	5Mpa Med	7.5Mpa Med
1	550	401	511	Stiff	701	267
2	233	538	217	Stiff	267	679
3	182	433	162	Stiff	882	586
4	150	365	278	Stiff	362	528
5	197	391	179	Stiff	436	429
6	310	497	242	Stiff		540
7	230	350	171	Stiff	350	523
8	210	224	164	Stiff	779	539
9	270	536	269	Stiff		376
10	702	345	371	Stiff	770	307
Max forward Deflection				Stiff		
Test#	5Mpa Large	7.5Mpa Large	56Mpa Large	Stiff Large	5Mpa Med	7.5Mpa Med
1	1837	1747	2202	Stiff	1749	1950
	1885	1795	2303	Stiff	1799	1999
	1935	1844		Stiff	1849	2049
2	958	1724	704	Stiff	962	4445
	983	1774	729	Stiff	987	4496
	1008	1826	755	Stiff	1012	4546
3	1049	1779	855	Stiff	1697	1647
	1075	1830	881	Stiff	1748	1697
	1100	1880	905	Stiff	1797	1748
4	799	1645	778	Stiff	1526	1434
	832	1708	809	Stiff	1587	1495
	862	1767	840	Stiff	1648	1555
5	822	1777	705	Stiff	1521	1737
	853	1837	735	Stiff	1584	1799
	884	1900	766	Stiff	1645	1861
6	850	1914	732	Stiff		1516
	881	1976	763	Stiff		1578
	912	2036	794	Stiff		1640
7	695	1516	703	Stiff	1447	1677
	739	1607	746	Stiff	1537	1765
	783	1693	791	Stiff	1627	1853
8	805	1515	669	Stiff	1313	1775
	849	1603	713	Stiff	1402	1864
	894	1693	757	Stiff	1491	1953
9	781	1500	846	Stiff		1651
	825	1588	890	Stiff		1740
	870	1677	935	Stiff		1828
10	1332	1561	1342	Stiff	1471	1334
	1945	1664	1450		1576	1439
	1543	1770			1680	1544

Initial frame	0.68				
Test#	56mpa Med	Stiff Med	Flex Fork	Stiff Fork	6Cone 7.5Mpa
1	886	Stiff Med	269	542	222
2	283	Stiff Med	595	508	563
3	264	Stiff Med	465	559	689
4	339	Stiff Med	570	531	641
5	322	Stiff Med	406	504	976
6		Stiff Med	525	515	512
7	285	Stiff Med	318	503	804
8	253	Stiff Med	410	546	748
9		Stiff Med	400	515	560
10	719	Stiff Med	304	548	347
Max forward Deflection					
Test#	56mpa Med	Stiff Med	Flex Fork	Stiff Fork	6Cone 7.5Mpa
1	1655	Stiff Med	1928	1713	1851
	1708	Stiff Med	1976	1762	1901
	1757	Stiff Med	2027	1813	1951
2	971	Stiff Med	1897	1712	1775
	997	Stiff Med	1839	1762	1825
	1022	Stiff Med	1889	1812	1875
3	815	Stiff Med	1745	1730	1930
	840	Stiff Med	1795	1702	1979
	865	Stiff Med	1844	1832	2032
4	796	Stiff Med	1844	1726	1544
	827	Stiff Med	1907	1787	1604
	858	Stiff Med	1966	1848	1666
5	814	Stiff Med	1548	1706	2217
	844	Stiff Med	1609	1767	2275
	875	Stiff Med	1732	1828	2334
6		Stiff Med	1524	1644	1464
		Stiff Med	1585	1708	1527
		Stiff Med	1646	1769	1587
7	856	Stiff Med	1726	1588	1650
	900	Stiff Med	1814	1676	1740
	945	Stiff Med	1902	1764	1831
8	702	Stiff Med	1491	1488	1531
	747	Stiff Med	1578	1577	1620
	791	Stiff Med	1668	1666	1708
9		Stiff Med	1440	1528	1441
		Stiff Med	1528	1616	1531
		Stiff Med	1616	1706	1708
10	1527	Stiff Med	1416	1512	1506
	1635	Stiff Med	1520	1617	1611
		Stiff Med	1626	1723	1718

Initial frame	0.53					
Test#	5Mpa Large	7.5Mpa Large	56Mpa Large	Stiff Large	5Mpa Med	7.5Mpa Med
1	505	580	334	Stiff	737	497
2	263	829		Stiff		776
3	251	279		Stiff	263	464
4	282	576	767	Stiff	228	276
5	187	648	555	Stiff	250	469
6	256	700	302	Stiff	426	182
7	181	502		Stiff	231	251
8	197	374	316	Stiff	263	214
9	280	391		Stiff	196	
10	539	342	354	Stiff	640	375
Max forward Deflection						
Test#	5Mpa Large	7.5Mpa Large	56Mpa Large	Stiff Large	5Mpa Med	7.5Mpa Med
1	1727	1729	1720	Stiff	1714	1768
	1774	1778	1768	Stiff	1763	1818
				Stiff	1812	1868
2	958	1675		Stiff		2026
	983	1726		Stiff		2051
	1008	1775		Stiff		2076
3	855	1695		Stiff	829	1042
	880	1746		Stiff	854	1067
	905	1796		Stiff	879	1092
4	891	1472	1671	Stiff	936	1317
	922	1535	1732	Stiff	967	1347
	952	1595		Stiff	998	1378
5	822	1653	1667	Stiff	897	1078
	852	1716	1728	Stiff	853	1108
	883	1778		Stiff	884	1139
6	780	1620	1717	Stiff	743	657
	811	1681	1782	Stiff	774	689
	842	1744		Stiff	804	720
7	738	1594		Stiff	680	897
	782	1682		Stiff	724	941
	826	1771		Stiff	768	985
8	737	1600	1770	Stiff	680	859
	781	1689	1859	Stiff	722	904
	826	1777		Stiff	769	949
9	735	1468		Stiff	617	869
	781	1553		Stiff	663	914
	824	1646		Stiff	706	958
10	1698	1692	1466	Stiff	1580	1497
	1785	1780	1552		1671	1563
		1872			1759	1673

Initial frame	0.53					
Test#	56mpa Med	Stiff Med	Flex Fork	Stiff Fork	6Cone 7.5Mpa	6cone Stiff
1	333	Stiff	632	457	272	
2	227	Stiff	884	334	506	
3	428	Stiff	497	689	521	
4	267	Stiff	468	500	400	
5	281	Stiff	505	541	280	
6	251	Stiff	448	533	490	
7	333	Stiff	484	522	418	
8	262	Stiff	371	550	396	
9	232	Stiff	316	490	219	
10	364	Stiff	323	523	292	
Max forward Deflection						
Test#	56mpa Med	Stiff Med	Flex Fork	Stiff Fork	6Cone 7.5Mpa	6cone Stiff
1	1654	Stiff	2071	1627	1843	
	1704	Stiff	2173	1676	1898	
		Stiff	2222	1726	1946	
2	847	Stiff	3286	1684	1700	
	872	Stiff	3335	1734	1750	
	897	Stiff	3385	1784	1799	
3	965	Stiff	1922	1681	1705	
	990	Stiff	1971	1731	1756	
	1015	Stiff	2022	1781	1806	
4	771	Stiff	1774	1448	1567	
	803	Stiff	1835	1510	1629	
	833	Stiff	1897	1571	1692	
5	714	Stiff	1644	1545	1772	
	745	Stiff	1706	1606	1835	
	776	Stiff	1767	1668	2020	
6	700	Stiff	1518	1562	2177	
	732	Stiff	1581	1622	2242	
	760	Stiff	1645	1686	2305	
7	683	Stiff	1654	1456	1523	
	728	Stiff	1743	1545	1611	
	772	Stiff	1831	1633	1698	
8	776	Stiff	1505	1705	1758	
	818	Stiff	1595	1796	1850	
	863	Stiff	1609	1885	1936	
9	722	Stiff	1448	1413	2265	
	766	Stiff	1545	1503	2357	
	811	Stiff	1634	1590	2440	
10	1536	Stiff	1462	1414	1564	
	1628	Stiff	1550	1503	1652	
		Stiff	1640	1591	1741	

13 Appendix D: Calculation of Dimensionless #s

13.1 Reynolds Calculation

To find and apply the Reynolds # across the object profile. The Reynolds number was calculated using the maximum velocity that occurs under the wave peak, applied to the whole water column. This is then applied to the equation.

$$R_e = \frac{UD}{v}$$

A check is run through the water column and wave so that only in the areas where the canopy exists is the equation applied. This generates a Reynolds profile for the object.

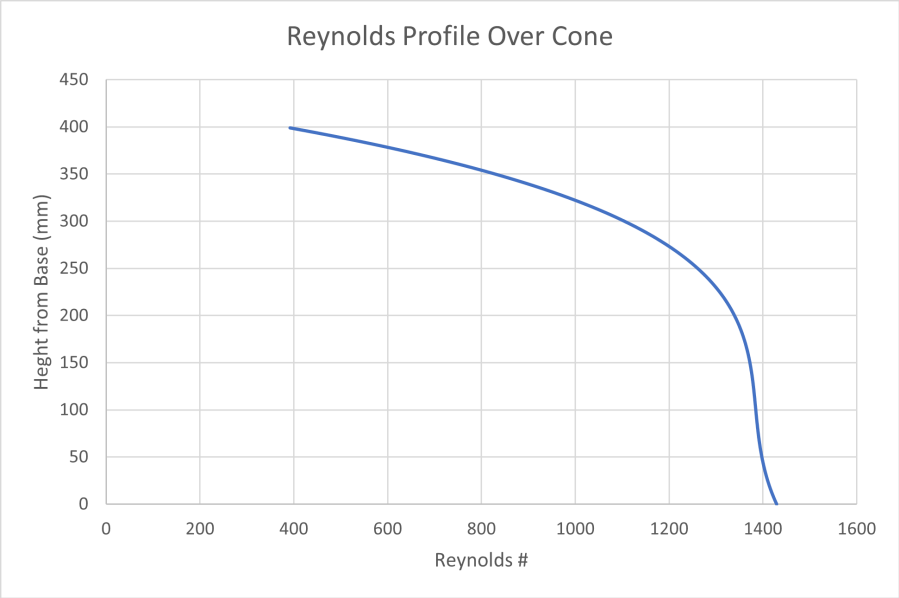

Figure 59: Reynolds Profile

13.2 KC, Ca, L , Cal/KC Calculation

This is done with the same methods as used in the Reynolds calculations however the governing equation is the Keulegan Carpenter equation

$$KC = \frac{UXT}{L}$$

the Cauchy

$$\frac{\rho \delta_y l^3 U_{ref}^2}{EI}$$

The same applied for the area-averaged calculations where Re is substituted with KC.

$$\frac{\int_0^z D * KC(z) dz}{A_c}$$

For the Ca number the $(\rho U_{ref}^2 \delta_y)$ part of the equation is averaged over the active area then multiplied by the constants $(\frac{l^3}{EI})$.

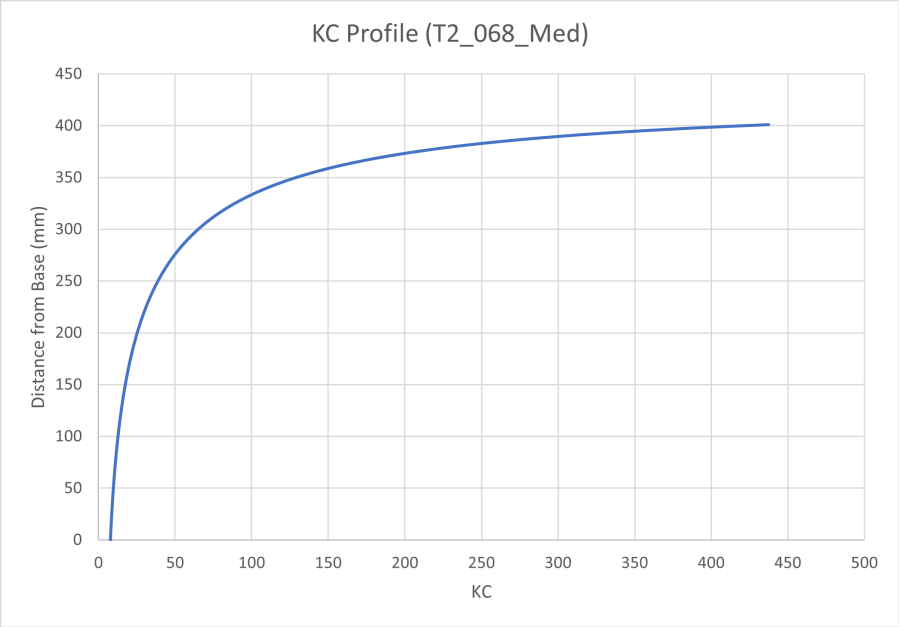

Figure 60: KC Profile

14 Appendix E: Instrument Calibration

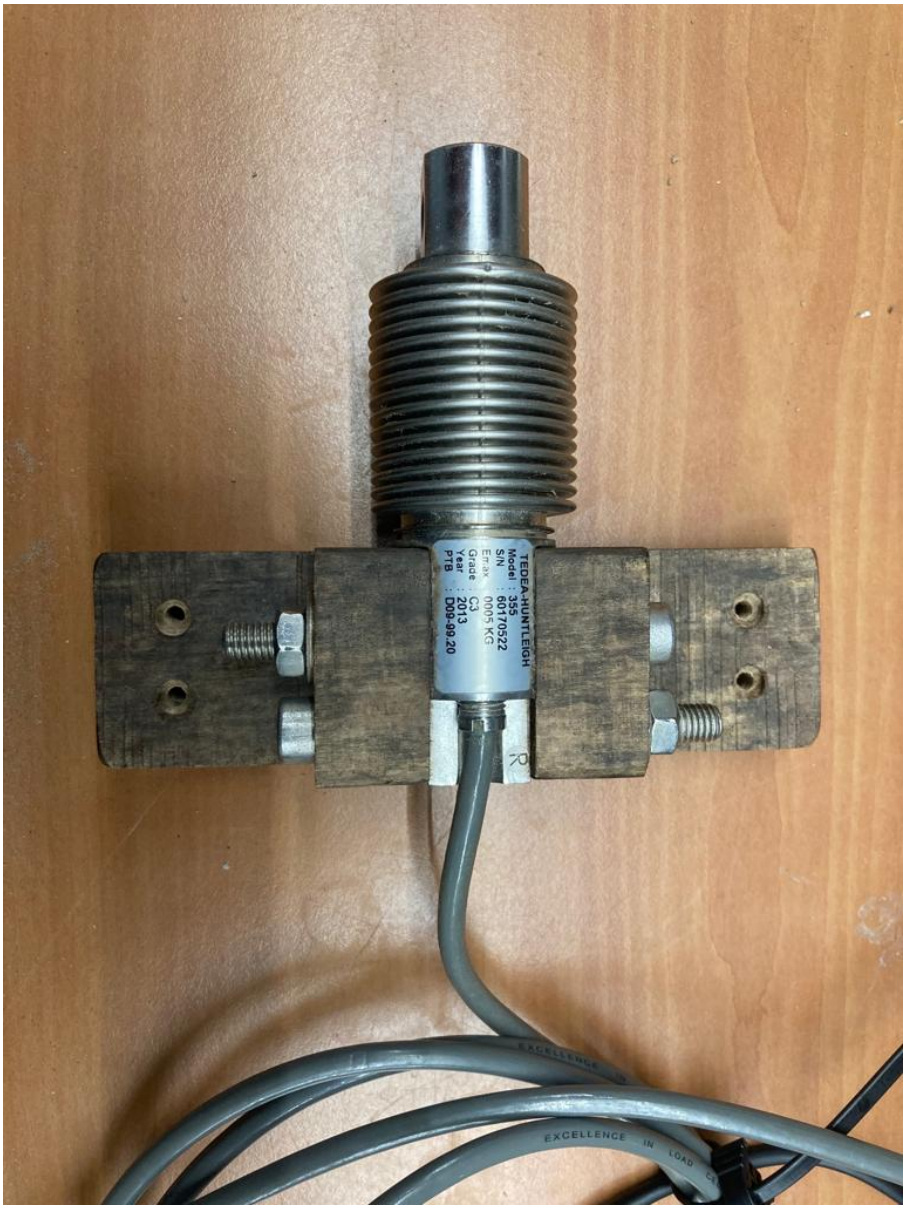

Figure 61: Force gauge

14.0.1 Force Gauge Calibration & Resolution

The force gauge was hooked up to an amplifier. From there the gauge was mounted horizontally to a wall and a bucket hooked up to the transducer. Water was added in increments using a syringe to ensure accurate measurements. Changes in the output voltages were recorded and used to provide a ratio for change in voltage to force. See gauge calibration in **??**. After calibration, the gauge was shown to have a sensitivity of roughly 2.5ml of water for 0.01 volt. This corresponds to a force of 0.024525 Newtons. For the Large and Medium cones, the resolution is more than enough to pick up forces generated by waves on all tests. For the thin cones, a single object may not generate the forces required. To combat this issue the thin cones will then be tested on a fork,

which will have 10 cones as 10 cones generates roughly the same frontal area as the large cone (0.007439 m^2), 10-Thin Cones (0.007568 m^2). This is more than sufficient to generate the required forces. the expected Forces generated by a singular small cone from the expected waves is around 0.0054 Newtons, having a fork of 10 cones puts that value up to 0.059 Newtons which is sufficient to pick up from the force gauge.

Table 8: FG Specs

Range (V)	Sensitivity (V)	Calibration Factor (N/V)	Sampling Freq (Hz)
10	0.01	0.024525	200

14.1 Damping Structure Image

Figure 62: Parabolic Wave Damper

14.1.1 Force Gauge Specs

Type:

TEDEA-HUNTLEIGH , Model: 355, S/N: 60170522, Emax= 5kg, Grade: C3, Year:2013, PTB: d09-99.20

www.vishaypg.com/load-cells

Stainless steel bending beam load cell

Versterker: 200x / 1000x ; Excitatie 10.5 V/ 2.5mA (name: DE-15-05)

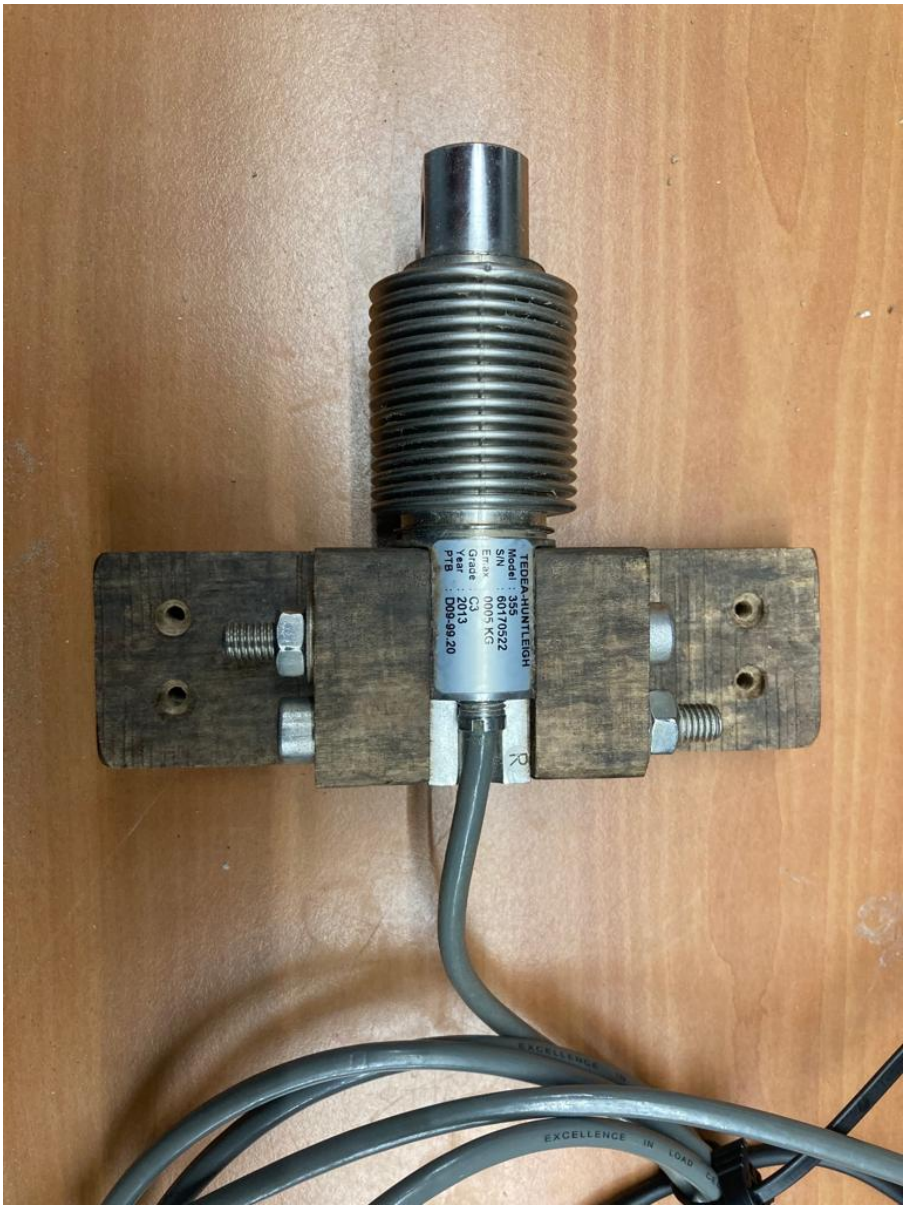

Figure 63: Force gauge

Table 9: FG Calibration

Block #	Weight (grams)	Measurement (V)	Force (N)
Offset		-2.74	
Bucket without water (+draad)	116.4	-2.24	1.141884
Bucket with 20 ml water	136.4	-2.16	1.338084
Bucket with 30 ml water	146.4	-2.11	1.436184
Bucket with 130 ml water	246.4	-1.69	2.417184
Bucket with 230 ml water	346.4	-1.26	3.398184
Bucket with 290 ml water	406.4	-1	3.986784
Bucket with 295 ml water	411.4	-0.98	4.035834

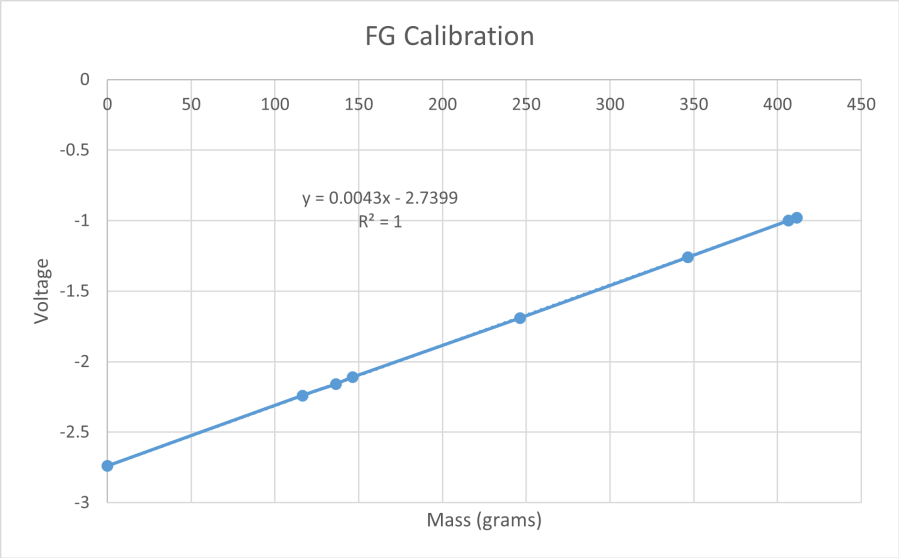

Figure 64: FG calibration

14.2 Wave Gauge Calibration factors and Locations

To calibrate the wave they were turned on at the start of testing each day, displaced 5 cm up or down and the difference between the two points was marked and recorded. Then a calibration factor for that day and the gauge were generated. Once the calibration is known similarly to the force gauge an average is taken over the first 100 points of data recorded while the water is still before the tests begin. Then the average is removed from the data zeroing it and the multiplication factor is applied to generate a viable plot of the water surface elevation. note: WG 7 had a faulty winch and sometimes needed to be displaced 10 cm to become stable, due to this some of the calibration factors in the table may seem very off for that gauge if that is the case check if needs to be adjusted by a factor 2 more than the others of the same day. For locations see table 10

Table 10: WG Placement

WG	X (m)
1	4.05
2	4.35
3	4.95
4	9.65
5	9.95
6	10.55
7	11.3
8	14.57
9	14.87
10	15.47

14.2.1 code

A1 = test1.data

WGFactors = [0.021008403 0.020242915 0.021008403 0.024154589 0.024509804 0.024390244 0.02016129 0.019685039

```
0.021645022 0.023584906 ];
for k = 2:11
WG1avg(k-1) = mean(A1(1:100,k));
end
for k = 2:11
WG1k-1 = A1(:,k)-WG1avg(k-1);
end
WG = cell2mat(WG1).*WGFactors;
```

day	time	WG1	WG2	WG3	WG4	WG5	WG6	WG7	WG8	WG9	WG10
8.12.2022	intial pos	-10	3.48	5.78	0.96	1.76	1.54	-10	3.3	1.27	-5.26
displacement	0.05	-10	1.04	3.37	-1.11	-0.25	-0.49	-10	0.78	-1.04	-7.35
9.12.2022	intial pos	2.99	0.34	0.24	0.19	0.65	0.09	0.84	5.87	-0.38	1.02
displacement	0.05	0.58	-2.16	-2.13	-1.92	-1.38	-1.96	-1.63	3.33	-2.69	-1.09
12.12.2022	intial pos	6.55	8.01	6.65	6.61	6.44	5.5	4.05	6.32	5.78	8.27
displacement	0.05	4.06	5.53	3.26	4.49	4.34	3.52		3.77	3.4	6.26
	0.1							-0.98			
13.12.2022	initial pos	-2.15	0	-0.55	-1.52	-1.54	-1.16	-4.81	-3.46	-2.18	2.72
	0.05	-4.51	-2.45	-2.92	-3.6	-3.56	-3.22	-7.34	-5.97	-4.47	0.57
14.12.2022	initial pos	-0.98	0.44	-0.07	1.58	2.88	0.94	-2.94	-0.62	0.48	3.54
	0.05	-3.36	-2.05	-2.45	-0.49	0.63	-1.11	-5.42	-3.14	-1.83	1.38
14.12.2022	initial pos	1.2	2.49	0.66	3.86	4.2	3.03	2.48	1.84	3.33	5.51
	0.05	-1.18	0.03	-1.74	1.76	2.08	0.96	-0.16	-0.68	0.98	3.35
15.12.2022	intial pos	-0.9	0.33	-1.46	2.01	2.34	1.2	0.12	-0.38	1.27	3.61
	0.05	-3.26	-2.14	-3.86	-0.06	0.28	-0.85	-2.37	-2.9	-1.32	1.45
15.12.2022	initla pos	0.35	-0.01	0.03	2.71	3.2	0.45	-2.47	-0.09	0.48	3.32
	0.05	-2.04	-0.248	-2.38	0.83	1.33	-1.59	-4.97	-2.61	-1.85	1.17
15.12.2022	initial pos	3.39	4.11	2.69	4.31	4.24	3.92	0.16	3.07	2.78	5.51
	0.05	1.02	1.61	0.26	2.21	2.17	1.89	-2.29	0.62	0.42	3.36
16.12.2022	intial pos	1.62	2.98	2.11	3.48	4.35	2.73	-0.18	2.26	2.4	4.95
	0.05	-0.76	0.5	-0.31	1.38	2.28	0.69	-2.5	-0.27	0.07	2.82
16.12.2022	intial pos	2.39	3.32	1.77	3.43	4.05	2.83	3.54	2.6	2.32	4.63
	0.05	0.12	0.85	-0.61	1.32	1.96	0.81	-1.48	0.09	0.42	0.05
4.1.2023	intial pos	0.35	0.62	-0.87	1.15	1.77	0.62	-1.78	-0.12	-0.26	0.88
	0.05	-2.06	-1.86	-6	-0.9	-0.25	-1.23	3.24	-2.65	-2.59	-1.23
								(-10)			
5.1.2023	intial pos	-2.08	-0.28	-1.4	-0.35	0.09	-0.89	0.43	-1.75	-1.74	0.59
	0.05	-4.45	-2.76	-3.82	-2.43	-1.96	-2.95	-4.6	-4.29	-4.06	-1.52
								10			
6.1.2023	intial pos	6.88	7.12	7.67	7.39	8.27	7.25	6.81	7.95	7.06	8.14
	0.05	4.48	4.7	5.25	5.26	6.14	5.21	4.25	5.37	5	6.17
6.1.2023	intial pos	0.52	0.24	-0.06	-0.42	-0.05	0.46	0.88	1.61	1.09	0.09
	0.05	-1.9	-2.23	-2.47	-2.54	-2.14	-1.58	3.37	-1.19	-1.26	-2.07
7.1.2023	intial pos	6.03	5.92	5.73	4.43	4.28	4.67	3.11	6.64	5.52	4.04
	0.05	8.43	8.38	8.14	6.53	6.4	6.67	8.01	9.15	7.83	6.22
9.1.2023	intial pos	0.65	0.58	1.05	0.95	0.73	1.47	1.24	1.53	0.29	0.55
	0.05	3.03	3.01	3.47	3.07	2.84	3.48	3.75	4.06	2.59	2.73
10.1.2023	intial pos	-1.25	-0.48	-0.1	-0.53	-0.42	-0.86	-0.05	0.55	-1.19	-0.66
morning	0.05	1.12	1.97	2.25	1.58	1.7	1.21	-5.05	3.09	1.13	1.29
10.1.2023	initial pos	0.41	0.75	0.44	0.23	0.57	0.16	0.69	0.98	0.01	0.2
evening	0.05	2.78	3.2	2.76	2.34	2.69	2.19	3.16	3.54	2.32	2.37
11.1.2023	initial pos	-4.3	-4.12	-4.41	-3.88	-3.52	-3.88	-4.31	-4.01	-4.62	-4.08
	0.05	-6.44	-6.62	-6.87	-5.97	-5.56	-5.74	-9.31	-6.54	-6.92	-6.19
11.1.2023	intial pos	-0.08	0.04	-0.12	-0.22	0.11	0.17	0.57	0.8	-0.02	0.01
	0.05	2.32	2.49	2.3	1.87	2.19	2.16	3.06	3.31	2.33	2.2

Table 11: WG Displacement Data

day	time	WG1	WG2	WG3	WG4	WG5	WG6	WG7	WG8	WG9	WG10
12.1.2023	intial pos	-4.91	-4.96	-4.94	-4.44	-4.12	-3.99	-4.54	-4.35	-4.73	-4.35
	0.05	-7.29	-7.38	-7.11	-6.48	-6.13	-6.02	-9.55	-6.84	-7.07	-6.48
12.1.2023	initial pos	-0.72	-0.54	-0.14	-0.43	-0.13	-0.56	4.06	0.45	-0.34	-0.38
	0.05	-3.09	-3.01	-2.52	-2.51	-2.2	-2.62	-0.96	-2.15	-2.66	-2.51
13.1.2023	initial pos	0.74	0.72	0.45	-0.13	0.69	0.27	0.74	0.82	0	0.31
	0.05	3.14	3.16	2.87	1.97	2.82	2.31	3.26	3.37	2.34	2.46
16.1.2023	intial pos	0.38	0.23	0.32	-0.33	0.07	0.26	0.83	0.85	0.68	0.29
	0.05	3.14	3.16	2.87	1.97	2.82	2.31	3.26	3.37	2.34	2.46
17.1.2023	initial pos	7.21	7.39	7.49	6.12	5.82	5.72	7.79	8.13	7.01	6.56
	0.05	5.03	4.94	5.1	4.02	3.73	3.69	5.34	5.56	4.67	4.35
18.1.2023	initial pos	0.08	0.02	0.77	0.11	0.12	0.03	-0.12	1.34	0.51	-0.9
	0.05	-2.32	-2.45	-1.62	-1.95	-1.94	-2	-2.61	-1.17	-1.81	-3
19.1.2023	intial pos	0.09	-0.29	0.3	0.04	-0.08	0.2	0.39	0.78	0.79	-0.17
	0.05	-2.12	-2.77	-2.08	-2.04	-2.13	-1.73	-2.2	-1.74	-1.51	-2.31
20.1.2023	initial pos	-2.45	-3.12	-2.29	-2.25	-2.19	-1.81	-2.42	-2.1	-2.09	-2.64
	0.05	-0.07	-0.64	0.07	-0.18	-0.15	0.22	0.06	0.42	0.2	-0.53
22.1.2023	initial pos	2.1	1.87	0.71	0.09	0.64	0.9	1.49	1.73	1.01	0.32
	0.05	4.47	4.3	3.04	2.17	2.76	2.91	3.98	4.22	3.3	2.51
24.1.2023	initial pos	-0.14	-0.39	-0.29	-0.39	0.04	0.53	0.66	0.7	0.22	0.13
	0.05	-2.16	-2.85	-2.72	-2.46	-2.04	-1.5	3.19	-1.85	-2.1	-2.05
25.1.2023	intial pos	0.07	0.13	-0.04	-0.08	-0.33	-0.17	0.15	0.7	0.15	-0.47
	0.05	-2.31	-2.36	-2.44	-2.16	-2.4	-2.26	-2.37	-1.84	-2.17	-2.59
27.1.2023	initial pos	-0.11	-0.31	-0.16	-0.29	-0.34	0.05	-0.04	0.57	-0.11	-0.26
	0.05	-2.49	-2.78	-2.54	-2.36	-2.38	-2	-2.52	-1.97	-2.42	-2.38

Table 12: WG Displacement Data.cont

day	WG1	WG2	WG3	WG4	WG5	WG6	WG7	WG8	WG9	WG10
9.12.2022	0.0207	0.0200	0.0211	0.0237	0.0246	0.0244	0.0202	0.0197	0.0216	0.0237
12.12.2022	0.0201	0.0202	0.0147	0.0236	0.0238	0.0253	0.0199	0.0196	0.0210	0.0249
13.12.2022	0.0212	0.0204	0.0211	0.0240	0.0248	0.0243	0.0198	0.0199	0.0218	0.0233
14.12.2022	0.0210	0.0202	0.0209	0.0240	0.0229	0.0243	0.0196	0.0198	0.0215	0.0231
15.12.2022	0.0211	0.0834	0.0207	0.0249	0.0251	0.0245	0.0202	0.0200	0.0207	0.0232
16.12.2022	0.0215	0.0202	0.0208	0.0238	0.0240	0.0246	0.0207	0.0198	0.0239	0.0172
4.1.2023	0.0207	0.0202	0.0210	0.0244	0.0248	0.0270	0.0199	0.0198	0.0215	0.0237
5.1.2023	0.0211	0.0202	0.0207	0.0240	0.0244	0.0243	0.0199	0.0197	0.0216	0.0237
6.1.2023	0.0207	0.0205	0.0207	0.0235	0.0237	0.0245	0.0198	0.0186	0.0228	0.0243
7.1.2023	0.0208	0.0203	0.0207	0.0238	0.0236	0.0250	0.0204	0.0199	0.0216	0.0229
9.1.2023	0.0210	0.0206	0.0207	0.0236	0.0237	0.0249	0.0199	0.0198	0.0217	0.0229
10.1.2023	0.0211	0.0204	0.0214	0.0237	0.0236	0.0244	0.0201	0.0196	0.0216	0.0243
11.1.2023	0.0221	0.0202	0.0205	0.0239	0.0243	0.0260	0.0200	0.0198	0.0215	0.0233
12.1.2023	0.0211	0.0205	0.0220	0.0243	0.0245	0.0245	0.0199	0.0197	0.0215	0.0235
13.1.2023	0.0208	0.0205	0.0207	0.0238	0.0235	0.0245	0.0198	0.0196	0.0214	0.0233
16.1.2023	0.0181	0.0171	0.0196	0.0217	0.0182	0.0244	0.0206	0.0198	0.0301	0.0230
17.1.2023	0.0229	0.0204	0.0209	0.0238	0.0239	0.0246	0.0204	0.0195	0.0214	0.0226
18.1.2023	0.0208	0.0202	0.0209	0.0243	0.0243	0.0246	0.0201	0.0199	0.0216	0.0238
19.1.2023	0.0226	0.0202	0.0210	0.0240	0.0244	0.0259	0.0193	0.0198	0.0217	0.0234
20.1.2023	0.0210	0.0202	0.0212	0.0242	0.0245	0.0246	0.0202	0.0198	0.0218	0.0237
22.1.2023	0.0211	0.0206	0.0215	0.0240	0.0236	0.0249	0.0201	0.0201	0.0218	0.0228
24.1.2023	0.0248	0.0203	0.0206	0.0242	0.0240	0.0246	0.0198	0.0196	0.0216	0.0229
25.1.2023	0.0210	0.0201	0.0208	0.0240	0.0242	0.0239	0.0198	0.0197	0.0216	0.0236
27.1.2023	0.0210	0.0202	0.0210	0.0242	0.0245	0.0244	0.0202	0.0197	0.0216	0.0236

Table 13: WG Calibration Factors

15 Appendix F: Full Equation Derivation

15.1 Applying Deflection

Starting out with a simple application from the analysis we understand that as forces increase deflection increases. For an object with the same dimensions, only a different Young's Modulus we understand that there should be a ratio where the peak force divided by the resistance to bending (EI) should be consistent across an object of the same dimensions.

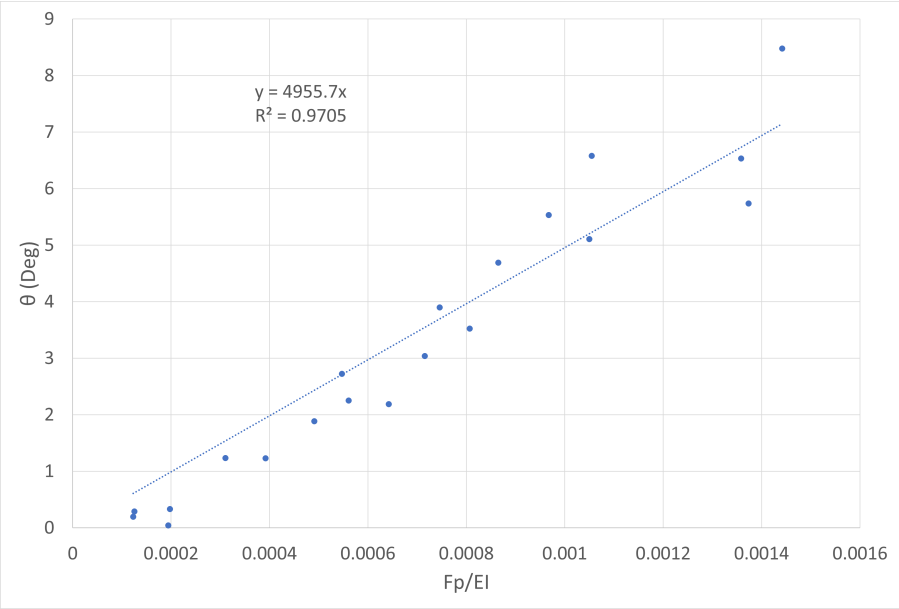

Figure 65: Deflection of Large Cones WL: 0.53 m

From this plot, we can see the general trend of the large objects for the 7.5Mpa and 5Mpa cases, as more force is applied relative to the object's resistance to bending we see a relatively linear increase than in the amount of bending of the object. In this case, a slope of roughly 4955.7 is generated. When this is then applied to the medium cones again we can see that there is a rather linear trend in the deflection.

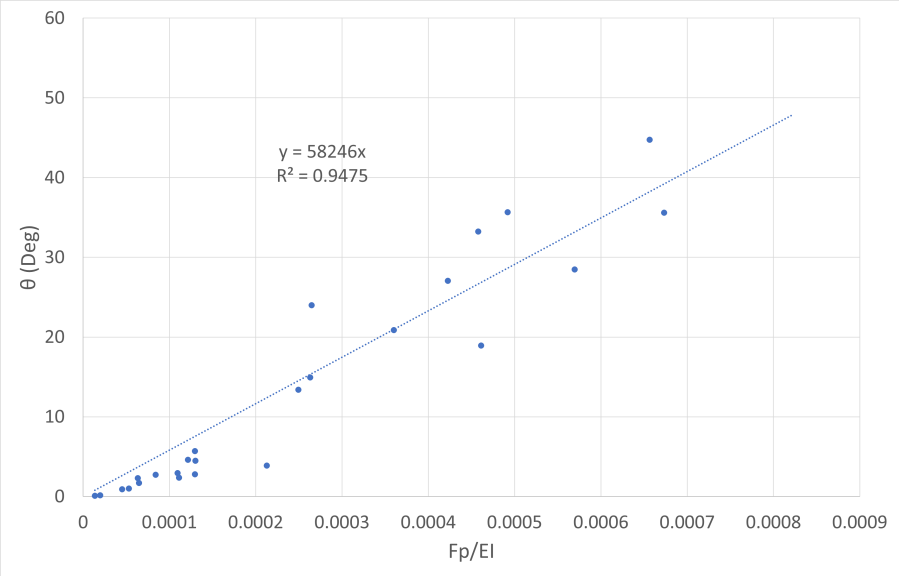

Figure 66: Deflection of Medium Cones WL: 0.53 m

From this plot we can again see the general trend of the medium objects or the 7.5Mpa and 5Mpa Medium cones, as expected the tips are much thinner and the objects go through significantly more bending than their larger counterparts during each wave. In this case a slope of 528246 is generated relative to the object's bending resistance.

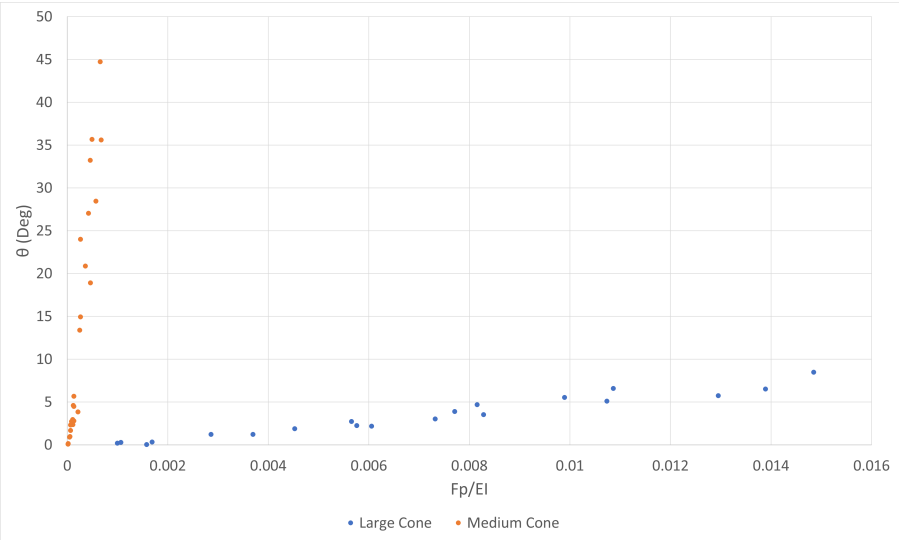

Figure 67: Medium and Large Cone Deflection WL: 0.53 m

While both plots on their own have very nice fits and linear regression once they are combined it becomes obvious that they have different governing equations. When the same amount of relative force to stiffness is applied to the object. Essentially this equation currently encapsulates the Cauchy eq as the force applied is in many ways equal to the flow of the fluid multiplied by the area submerged. To fully satisfy all requirements three more effects must be added, the shape factor of the object which in this case is proposed through the

object volume over Area which is.

$$V = \pi r^2 h/3 \tag{62}$$

$$A = r * h \tag{63}$$

This results in,

$$\pi/3 * r \tag{64}$$

since all objects are of the same shape in this testing the $\pi/3$ can be removed leaving a multiplier of r. The second effect is the moment arm of the force which in theory is roughly the still water level of the wave, however for a partially submerged object wave skew has a large effect therefore the peak impact height of the wave relative to the base of the object is used (η). Third is the tapering of the object. This is added to the equation by multiplying the object by the cube of the slope S, Eq.(39). In essence, what this achieves is the addition of an extra shape factor. The larger the slope of an object the faster it narrows which implies increased support against bending. This also relates the object's length to its thickness, the thinner the object the less resistance to bending. Leaving the fully dimensionless#.

$$\frac{F_p r \eta_p S^3}{EI}$$

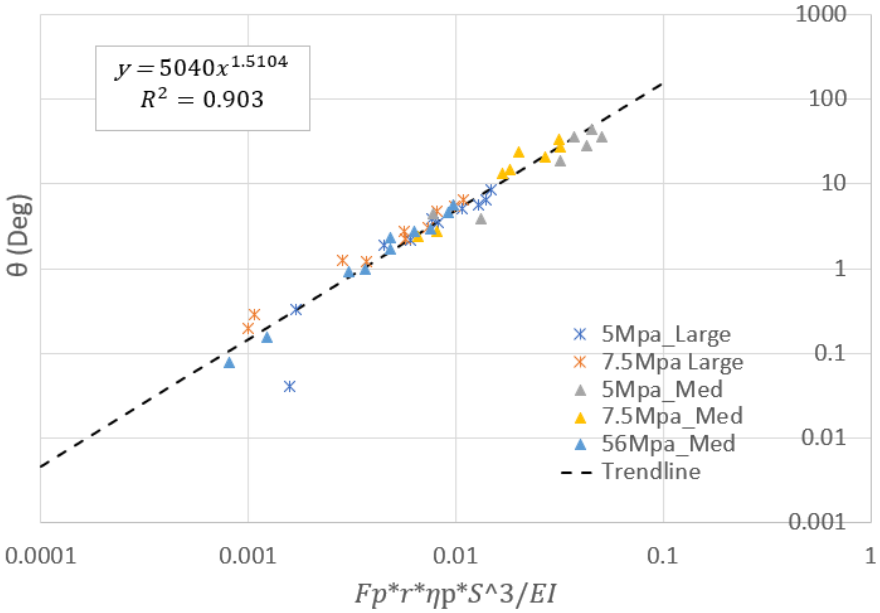

Figure 68: Fully Scaled Deflection WL: 0.53 m

What this now shows is that the degree of tip deflection, when related to the peak force applied, is multiplied roughly by the maximum moment arm and adjusted for the shape of the object. Then divided by the resistance of the object to bending The applied curve is a Power fit curve and this generates a quite nice R^2 value of 0.903 meaning this data has a 90% fit. Even more interestingly if we then apply this same style to either the Medium

or Large cones in singularity the same fit is again generated with very similar powers.

When applying this same equation to the 0.68 WL for the large and Medium cones we get the following graph

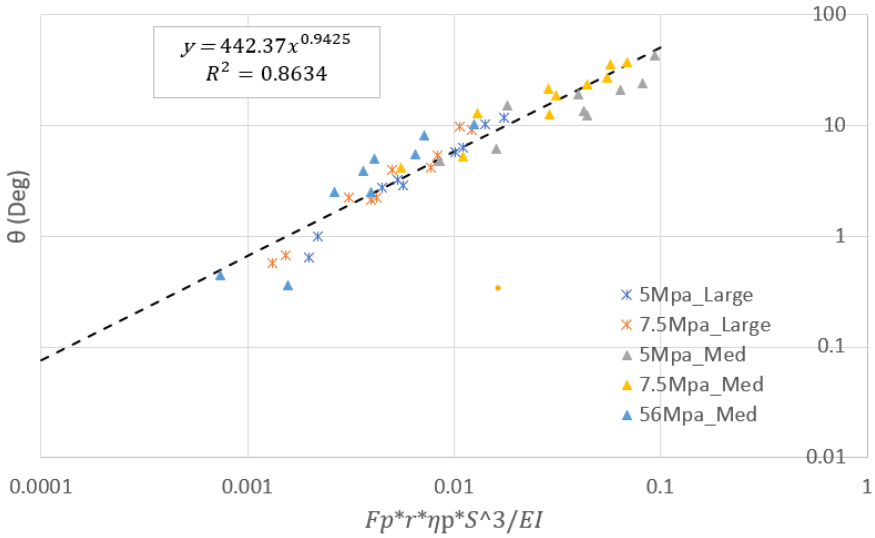

Figure 69: Fully Scaled Deflection 0.68

In this case, the slope and power are decreased as well as the fit, around 0.86, but still within the same range. Between the two different water levels, there are two confounding factors across all tests. In the 0.53 WL three of the waves are waves that have broken and are rollers before impact, this occurs in tests 6,8,9. And again in the high WL at 0.68 the object may become fully submerged due to deflection and the incumbent wave height. When looking at the broken waves inside the tests which correspond more to the peak leftmost points in the graph we see they still seem to follow the trend of the data quite well. This is because the variable of peak force encompasses the effects of the wave impact on the object. Especially for the large cones the high-impact rollers are present in the bulk of the data, with deflections of around 8 degrees. Due to the stiffness of the larger objects still receive the force in line with the rest of the data. However, for the objects that become fully submerged at 0.68 this may also have a large effect on the equation, as suddenly the wave peak ie) η_p is no longer occurring on the object but above which means the forces cap out at an applied distance of 0.43 however, in theory, this should still work properly as the forces are known. Of course, other factors can also confound the results, namely resonant oscillation with the waveform which will result in lower peak forces, and higher deflection relative. The resonance is most likely to have the largest impact and occurs more often at the 0.68m WL.

Applying both the large and medium data sets across both water levels the following figure is generated.

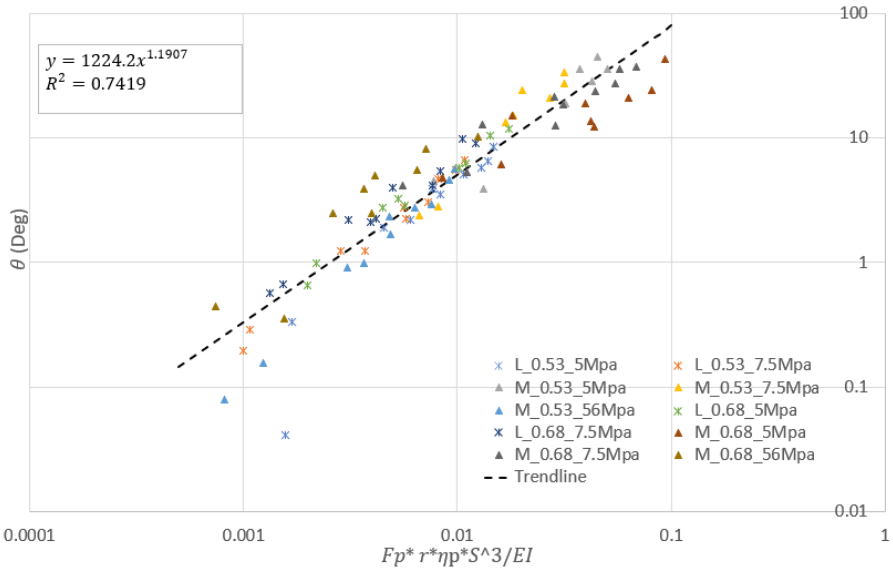

Figure 70: All Data Points WL 0.53,0.68

Theoretically, using this curve if someone were to apply a wave to a conical object, (as this is only run on conical objects it is improper to assume it works for others) then one could roughly predict the maximum tip deflection. First by calculating the force applied by the fluid due to flow, and the total object EI, generating this equation.

$$\theta = 1224 * (\frac{F_p r \eta_p S^3}{EI})^{1.19} \tag{65}$$

Where deflection is in deg, F_p, is in Newtons, and E is Young's modulus in Mpa, I is in m^4, and η is the peak impact in meters and S is the object slope.

However calculating F_p is the most complicated part of this equation, for a relatively stiff object this value should correspond with the peak forces generated by the orbital velocities since the object will not deflect. For highly deflecting objects the peak force will change as more of the object will then be interacting with the wave, possibly as seen many times in this experiment resulting in the object becoming fully submerged due to the wave and deflection. Also, highly deflective objects will move more quickly with the wave reducing the effects of the wave impact discussed earlier. Most likely an iterative or CFD style approach would work best to determine the object peak deflection and from it the peak forces one equation already exists being the above eq, however, the second part would also need to incorporate bending and deflection, the commonly used equation

$$f_x = 1/2 \rho U_{ref}^2 \delta_y C_D + \frac{\pi}{4} \int_{z=0}^{h_v} C_M \delta_y^2 U_{ref} \frac{dt}{du} dz \tag{66}$$

which is the combination of Eqs (4, 5)would be the best method provided the drag coefficient is well known for the object.